1-12-2015

Design, Fabrication and Characterization of MIM Diodes and Frequency Selective Thermal Emitters for Solar Energy Harvesting and Detection Devices

Saumya Sharma
University of South Florida, saumya1@mail.usf.edu

Follow this and additional works at: https://scholarcommons.usf.edu/etd

Part of the Electrical and Computer Engineering Commons, and the Materials Science and Engineering Commons

Design, Fabrication and Characterization of MIM Diodes

and Frequency Selective Thermal Emitters for Solar Energy Harvesting and Detection Devices

by

Saumya Sharma

A dissertation submitted in partial fulfillment
of the requirements for the degree of
Doctor of Philosophy in Electrical Engineering
Department of Electrical Engineering
College of Engineering
University of South Florida

Co-Major Professor: Elias Stefanakos, Ph.D.
Co-Major Professor: D. Yogi Goswami, Ph.D.
Andrew Hoff, Ph.D.
Jiangfeng Zhou, Ph.D.
Manoj Ram, Ph.D.

Date of Approval:
January 12, 2015

Keywords: Langmuir Blodgett films, tunnel diode, plasmonics, selective emitter

DEDICATION

This work is dedicated to the innate virtues of human inquiry and causal reasoning that fuel all

scientific endeavors.

TABLE OF CONTENTS

LIST OF TABLES

LIST OF FIGURES

iv

vi

ABSTRACT

Energy harvesting using rectennas for infrared radiation continues to be a challenge due to the lack of fast switching diodes capable of rectification at THz frequencies. Metal insulator metal diodes which may be used at 30 THz must show adequate nonlinearity for small signal rectification such as 30 mV. In a rectenna assembly, the voltage signal received as an output from a single nanoantenna can be as small as ~30μV. Thus, only a hybrid array of nanoantennas can be sufficient to provide a signal in the ~30mV range for the diode to be able to rectify around 30THz. A metal-insulator-metal diode with highly nonlinear I-V characteristics is required in order for such small signal rectification to be possible. Such diode fabrication was found to be faced with two major fabrication challenges. The first one being the lack of a precisely controlled deposition process to allow a pinhole free insulator deposition less than 3nm in thickness. Another major challenge is the deposition of a top metal contact on the underlying insulating thin film. As a part of this research study, most of the MIM diodes were fabricated using Langmuir Blodgett monolayers deposited on a thin Ni film that was sputter coated on a silicon wafer. UV induced polymerization of the Langmuir Blodgett thin film was used to allow intermolecular crosslinking. A metal top contact was sputtered onto the underlying Langmuir Blodgett film assembly. In addition to material characterization of all the individual films using IR, UV-VIS spectroscopy, electron microscopy and atomic force microscopy, the I-V characteristics, resistance, current density, rectification ratio and responsivity with respect to the bias voltage were also measured for the electrical characterization of these MIM diodes.

Further improvement in the diode rectification ratio and responsivity was obtained with Langmuir Blodgett films grown by the use of horizontally oriented organic molecules, due to a smaller tunneling

distance that could be achieved in this case. These long chain polymeric molecules exhibit a two-dimensional molecular assembly thereby reducing the tunneling distance between the metal electrodes on either side of the insulating layer. Rectification ratios as high as 450:1 at ±200mV were obtained for an MIM diode configuration of Ni-LB films of Arachidic Acid films-(Au/Pd).

The bandwidth of the incident radiation that can be used by this rectenna assembly is limited to 9.5% of 30THz or ±1.5THz from the center frequency based on the antenna designs which were proposed for this research. This bandwidth constraint has led to research in the field of frequency selective emitters capable of providing a narrowband emission around 30THz.

Several grating structures were fabricated in the form of Ni-Si periodic arrays, in a cleanroom environment using photolithography, sputtering and deep reactive ion etching. These frequency selective samples were characterized with the help of focusing optics, monochromators and HgCdTe detectors. The results obtained from the emission spectra were utilized to calibrate a simulation model with Computer Simulation Technology (CST) which uses numerous robust solving techniques, such as the finite element method, in order to obtain the optical parameters for the model. Thereafter, a thorough analysis of the different dimensional and material parameters was performed, to understand their dependence on the emissivity of the selective emitter.

Further research on the frequency selectivity of the periodic nano-disk or nano-hole array led to the temperature dependence of the simulated spectra, because the material parameters, such as refractive index or drude model collision frequency, vary with temperature. Thus, the design of frequency selective absorbers/emitters was found to be significantly affected with temperature range of operation of these structures.

CHAPTER 1:

INTRODUCTION

Energy harvesting technologies have received significant research emphasis over the recent years. Several microelectronic devices are being engineered with this application in mind. Devices based on working principles of photoelectric effect and quantum tunneling have shown improved energy conversion potential to produce electricity. While photovoltaic cells suffer from the Shockley-Queisser limit, in terms of their maximum attainable conversion efficiency, rectenna solar cells have shown promising efficiencies higher than 85% for conversion of electromagnetic radiation to DC at GHz frequencies [1-2].

In order to utilize a significant amount of electromagnetic radiation from the sun, a rectenna must operate at high frequencies, at least in the order of THz. A basic rectenna assembly consists of an antenna and a rectifying diode. The antenna captures the incident electromagnetic radiation while the diode rectifies the AC field across the antenna to produce direct current. High frequency antennas with adequately broad bandwidths suitable for this application are available for use [3]. The main objective of this research is to fabricate a metal-insulator-metal (MIM) diode that can be used for rectification at such high frequencies. PN junction and Schottky diodes cannot be used for this purpose because of their operating frequency limitations. Tunnel diodes, on the other hand, are capable of rectification in the THz range [4].

The peak irradiance for the solar spectrum occurs around 600THz, but rectification at such high frequencies remains a challenge. Thus, there is a need for an intermediate emitter that can absorb the

1

incident solar radiation while selectively emitting it around the operating frequency of the MIM diode. This leads to the second objective of this project, which involves the design of a frequency selective infrared emitter. Such an emitter may be designed with the help of periodic nanostructure arrays patterned onto a metal-dielectric photonic crystal [5–7].

The proposed assembly would work such that the radiation incident onto the plasmonic thermal emitter would raise its temperature and cause it to selectively emit around the center frequency of the antenna. The diode would then rectify the AC output of the antenna to deliver direct current.

1.1 Rectenna

The word rectenna symbolizes a combination of the words "*rectifying antenna.*" A rectenna may be understood as an antenna matched to couple IR energy into the terminals of a diode, where this IR energy is rectified from AC to DC power. These devices operate as long as the turn-on voltage of the rectifying element is below the amplitude of the coupled RF signal. Figure 1 shows a block diagram representation of a rectenna assembly.

The rectenna was invented in 1964 by William C. Brown [1]. His design incorporated a dipole antenna which provided input to a Schottky diode to convert microwaves into DC power. The Schottky diode was selected for this application because of its high switching speed and low forward voltage drop. This meant more of the power coupled into the antenna would be converted form AC to DC and thus more would be available to power the intended application. There have been successful industrial implementations of wireless power transfer in the microwave region using this technology. It was proposed that this technology could be extended to high frequencies approaching those of visible light. If the antenna, impedance matching circuitry, and rectifier could all be built to an appropriate size and operational speed, the system could, in theory, be used to rectify light—which is an electromagnetic wave. This was a very attractive proposition because it opened up the possibility of

2

direct harvesting of solar radiation and remote harvesting of waste heat from industrial applications. For a rectenna to operate in the infrared frequency range it will not be appropriate to use a Schottky diode due to its frequency limitation. A tunnel diode would be suitable for rectification at frequencies around 30THz due to its faster switching speed. For the purpose of this research, metal-insulator-metal and metal-double insulator-metal diode based tunnel junctions will be fabricated.
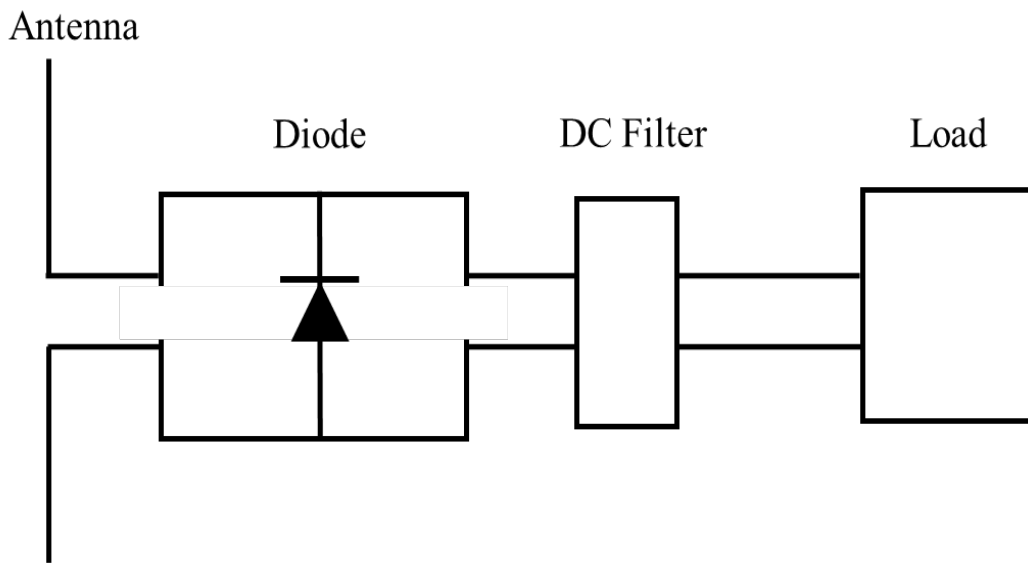
Figure 1 Block diagram representation of a rectenna assembly.
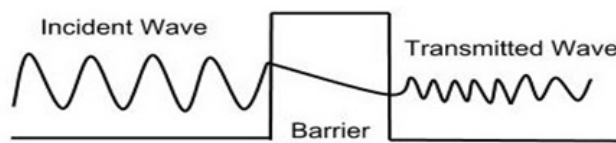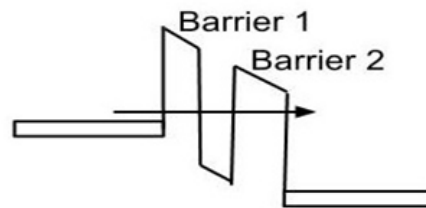
Figure 2 Schematic representations of (a) MIM and (b) MIIM diodes.

3

1.2 Metal Insulator Metal Diode

A Metal-Insulator-Metal (MIM) tunnel junction consists of a stacked assembly of an ultrathin insulator sandwiched between two metal layers. It is a quantum tunneling device in which rectification takes place with the flow of electrons from one metal plate to another by overcoming the potential barrier. The tunneling mechanism allows rectification of an applied AC signal resulting in a DC output component.

The top contact area in an MIM tunnel junction depends on the relationship between operating frequency and the capacitance of the tunnel junction. The working of such a diode can be easily interpreted with the help of an energy band diagram like that for an asymmetric MIM junction at equilibrium. Figure 3 shows thin insulator layer(s) sandwiched between two dissimilar electrodes with different work function.

The resonant tunnel MIIM diode has a quantum well structure and it uses electron tunneling by possessing the unique property of negative differential resistance in the current-voltage behavior. It consists of two insulator barriers, one with a low barrier height and the other with a higher barrier height. By introducing the second insulator later of the MIIM tunnel diode, its limitations of conductivity and nonlinearity can be simultaneously overcome. Alimardani et al. have experimentally demonstrated how a second insulator layer could introduce additional asymmetry than conventional MIM diodes [8–10]. They also present the enhanced low voltage asymmetry and nonlinearity enhancement and low resistance with the choice of dissimilar metals along with insulator hetero-junctions as in a $M_1I_1I_2M_2$. Grover et al. have extensively analyzed the limitations of single insulator MIM diodes and compared those to MIIM configurations [4,11].

They have also demonstrated the quantum well formation for MIIM diodes under forward bias conditions and made a comparison between thin and thick two barrier insulator containing diodes. At

4

equilibrium conditions the Fermi levels of the metal electrodes line up. The Fermi level moves down by qV_a by an applied potential with q being the charge. The potential barrier between the electrodes reveals a trapezoidal shape and a triangular quantum well forms between the insulators under forward bias. When the lowest quantum well energy is lower than the Fermi level of the adjacent metal, the electrons can freely tunnel through the layers, whereas, under reverse bias conditions, there is no such quantum well. Thus, current (I) - voltage (V) behavior of a resonant tunneling diode is highly nonlinear and asymmetric suited for rectification purposes at higher frequencies.
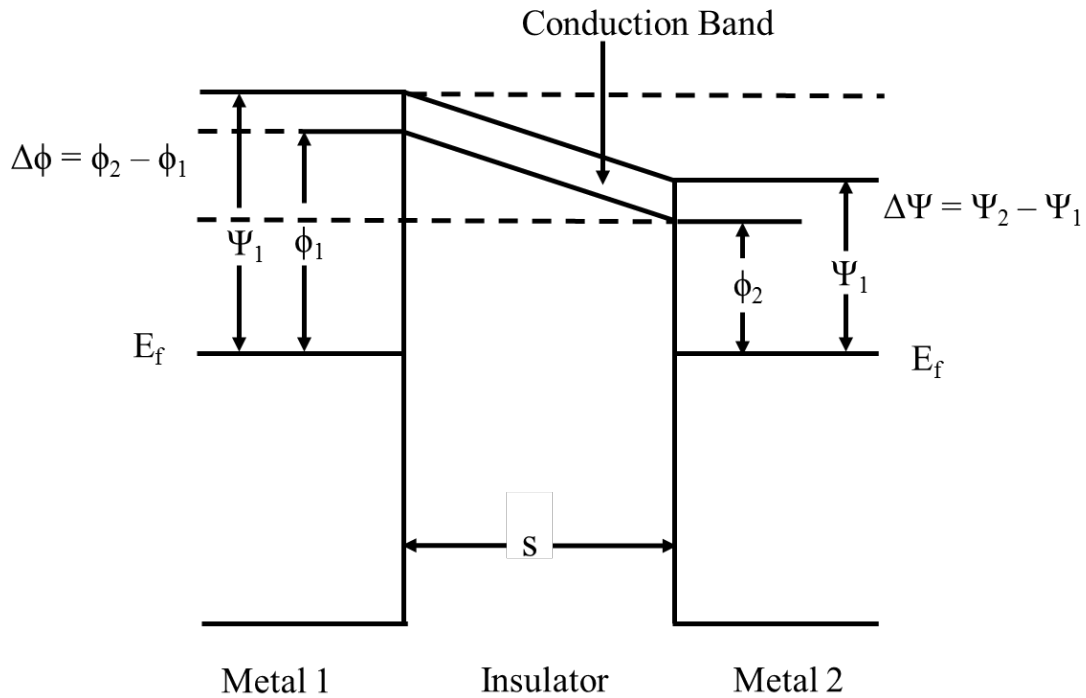
Figure 3 Energy band configuration at zero bias in a metal-insulator-metal tunnel junction.

1.3 Frequency Selective Emitter

Spontaneous emission from bulk thermal sources is known to suffer from limitations of incoherence, lack of directionality and broadband nature of emission. Different bulk materials possess varying optical properties. Often multi-material complexes, such as layer by layer photonic crystals, are utilized to modify optical properties such as transmission or emission. Surface modification also leads to

5

excitation and coupling of surface plasmon modes, thereby influencing the optical properties of the crystal [12–16]. Thus, it is possible to tune the emission spectrum according to the desired application, with the help of surface patterning of a periodic grating on a layered metal-dielectric structure. Microstructures of sub wavelength dimensions when etched onto a photonic crystal allow such application specific tailoring of the emission spectrum. Several periodic array structures with rectangular, square or circular holes, disks or gratings have also exhibited extraordinary emission peaks [7,17].

A fundamental relationship between the optical and electronic properties of materials with hole and electron conduction was given by Paul Drude in 1900. This led to the frequency dependent, complex optical dielectric function:

$$\varepsilon(\omega) = 1 - \left(\frac{\omega_p^2}{\omega(\omega - i\omega_c)}\right)$$

where ω is the frequency at which the dielectric function is being calculated, ω_c is the electron collision frequency and ω_p is the plasma frequency. It is critical to note that ω_c and ω_p are temperature dependent variables in the above equation. There is a relatively small change in the plasma frequency, ω_p, with increase in temperature due to volume expansion. For this reason the value of ω_p for gold has been assumed to be constant throughout the research as $\omega_p = 1.29 \times 10^{16}$ cm^{-1}.

During experimentation, the emittance of the thermal emitter was calculated using the ratio of the radiation emitted from the sample at a temperature T, to the radiation emitted from a blackbody at the same temperature T. For theoretical calculations, the concept was formulated on the basis of fundamental conservation of energy at the macroscopic level and Kirchhoff's law of thermal radiation. According to the conservation of energy, the incident energy ($\Phi_{incident}$) must be conserved as the sum of the reflected($\Phi_{reflected}$), transmitted($\Phi_{transmitted}$) and absorbed($\Phi_{absorbed}$) portions of

6

energy. This was also used as a theoretical basis for the simulation model set up to obtain the emissivity spectrum and to analyze the effect of dimensional/material variations on the frequency selectivity of emission.

$$\Phi_{incident} = \Phi_{reflected} + \Phi_{absorbed} + \Phi_{transmitted}$$

Or 1= ρ+ α+ τ where ρ, α and τ are the reflectance, absorptance and transmittance, respectively. For opaque surfaces, the transmittance maybe ignored, and this was ensured by considering a metal ground plane at the back of the photonic crystal structure. Using Kirchhoff's law, in thermal equilibrium, the emittance of the designed emitter must equal the absorptance, thus giving,

$$\varepsilon_\lambda = 1 - \rho_\lambda$$

Thus, it is possible to compute the emissivity spectrum using reflectance measurements for a particular photonic crystal. This technique can be useful to determine the impact of dimensional variations and choice of material which influence the frequency selectivity of emission.

CHAPTER 2:

LITERATURE REVIEW

2.1 MIM and MIIM Tunnel Diodes

A significant amount of research has been carried out in the design and fabrication of MIM and MIIM diodes. While most of the research focused on insulating metal oxide layers, atomic layer deposition and sputtering techniques were mostly used in the fabrication of these rectifying devices.

Alimardani et al. have presented research on nanolaminate bilayer insulator tunnel barriers of combinations of aluminum, hafnium and zirconium oxides deposited via atomic layer deposition (ALD) with asymmetric work function metal electrodes to produce MIIM diodes with enhanced I-V asymmetry and non-linearity. They claim improvements in MIIM devices using step tunneling rather than resonant tunneling [8].

Bhansali et al worked on a quantum approach to increase the efficiency of solar/thermal energy conversion by converting waste heat to electrical energy using rectennas with high frequency antennas and state of the art metal insulator metal tunnel diodes both with organic and inorganic insulating layers [18]. They reported diode characteristics for a Nickel-Nickel Oxide-Chromium layered assembly as well as a Gold-self assembled monolayer of 1-dodecanethiol-Chromium based organic metal insulator metal diode.

Celestin et al have reported experimental proof of substrate roughness dependence on the current voltage response of an MIM diode. The diodes fabricated for this research used self-assembled alkanethiol films deposited on Gold substrates[19].

8

Chin et al have also presented research on the use of MIM diodes for energy harvesting applications using Pt/TiO$_2$/Ti layered diodes. They have shown the dependence of dielectric thickness on linearity and symmetry of the electrical characteristics of the diode [20].

Dagenais has worked on the development of rectifying antenna assemblies to harvest solar energy. His research has proposed the use of a geometric field enhancement scheme in rectennas based on surface plasmon resonance. This approach was experimented in a polysilicon/SiO$_2$/polysilicon based tunnel diode. The surface plasmons showed electric field enhancement across the tunnel junction, while reducing the required voltage to turn on the diode, thus indirectly improving the efficiency of energy conversion [21].

Grover et al. have evaluated the performance of rectennas designed to operate at infrared frequencies. They have shown the suitable use of femtosecond-fast MIM diodes in a traveling-wave configuration for improvement of the bandwidth of operation and better detection efficiency. They have also devised a method to calculate the responsivity of such a traveling wave detector coupled antenna setup. They have reported their best responsivity in the case of a Nb-Nb$_2$O$_5$-Nb based traveling wave diode at a 3μm wavelength. They have also demonstrated how lowering the diode resistance and increasing the antenna area and noise reduction can lead to improvement of the detecting ability of the rectenna [22]. In another one of their publications they have shown the use of photon-assisted transport theory to calculate the current-voltage characteristics of metal insulator metal tunnel junctions under illumination [23]. Among other results they have also developed a model to calculate current voltage characteristics using a semiclassical approach which accounts for the photon energy associated with the incident radiation. The results indicate a difference in the diode resistance and responsivity values from those expected with the classical model for tunneling [11].Hashem et al. have developed an analytical model that employs a Transfer Matrix Method to determine the probability of

tunneling transmission through a number of insulating layers. Their work also provides a study of factors such as work function difference and insulator thickness and their effect on the performance of a tunnel diode. Their results show improvement in diode responsivity, resistance and nonlinearity by using double insulating layers in the MIM assembly [24]. In another one of their publications, Nb/Nb$_2$O$_5$ based MIM diodes were studied. They have shown the impact and calculation for total rectenna efficiency as a factor of thickness of metal layers, work function difference and insulator thickness [25].

Imafidon et al. have also analyzed the possibility of energy harvesting using rectennas in the military and commercial sectors. They have worked on nanowire antennas and high speed rectifiers for conversion of THz radiation into DC power. They have analyzed the current and induced voltage in nanowire antennas by varying geometric parameters for different frequencies of input radiation. Their research includes the optimization of nanoantennas so that they can be used in the energy conversion of a broader band of frequencies [26].

Joshi and Moddel have presented an analysis of advantages of rectenna solar cells over conventional photovoltaics. They also mention that rectenna solar cells can convert energy at efficiencies exceeding the Shockley Queisser limit. Their publications also provide a quantitative analysis of broad band energy conversion in the rectifying element using the theory of photon-assisted tunneling. They have concluded that the quantum based approach and low frequency classical rectification show different results [28-29].

Kinzel et al. have described their rectenna based energy conversion experiment with a graphene diode coupled with a metal bowtie antenna. A low capacitance could be maintained in this graphene diode by keeping it structurally planar They have found such a diode to be more suitable for high frequency rectification, compared to an MIM diode[29]. In another one of their publications, Kinzel et al. have

10

reported the application of metal-oxide-metal diodes for rectification of high frequency radiation in sensing or energy harvesting. They have proposed the integration of a slot antenna frequency selective surface with the metal-oxide-metal diode rectifier. In this way, increasing the radiation capture area while decreasing the length of the transmission line has helped in the reduction of losses. Their work has claimed to be promising for infrared sensing, imaging and direct conversion of heat to electricity [30].

Krishnan et al. have used a Ni-NiO-Cr tunneling assembly for detection at far-infrared frequencies. They have also fabricated a 2.5 GHz microstrip slot antenna usable in a rectenna setup. Their MIM tunnel diode has shown a high sensitivity and asymmetric current voltage characteristics. An experiment with the slot antenna coupled with a Schottky diode detector has been reported to show a rectified output voltage of 56 mV [31]. In another one of their publications, Krishnan et al. have reported the fabrication of a planar, asymmetric MIM diode with Ni-NiO-Cr layers. This diode had a contact area of $1\mu m^2$. They have presented the electrical characteristics of the detector and verified the same with a theoretical model [32].

Periasamy et al. have also studied the possibility to convert visible light to electricity using rectennas. For their energy conversion setup, they fabricated $Nb\text{-}Nb_2O_5$ and $Nb\text{-}TiO_2$ based tunnel diodes and successfully tested them at low frequencies. They deposited a thin insulating layer using anodic oxidation of the underlying metal. Their top metal contact was in the form of a bent wire thereby forming a point-contact diode. They optimized the technique of deposition to lay down the insulating layer and to attain the desired chemical composition. They have also presented a systematic study which reveals a strong relation between the work function and electron affinity of the metal and insulator and the electrical characteristics of the diode [33]. In another one of their publications, they have reported very good diode performance in $Nb/Nb_2O_5/Pt$, $Nb/Nb_2O_5/Au$, $Nb/Nb_2O_5/Ag$ and

11

Nb/Nb$_2$O$_5$/Cu based tunnel junctions. Their results show that these MIM diodes can be employed in ultra-fast rectification applications [34]. Perisamy et al. have also reported the electrical characteristics of MIM systems with Nb$_2$O$_5$, TiO$_2$, Al$_2$O$_3$, MgO insulating layers sandwiched between Nb/Pt metal electrodes [35].

Ratnadurai et al. have fabricated Ni/NiO/Cr MIM diodes with different structural variations. They have made stacked, stepped self-aligned, stepped manual aligned and stepped spacer type metal-insulator-metal assemblies. Their electrical properties were studied to find the effects of the diode assembly on asymmetry and emission current. The stepped structure with an oxide spacer has been found useful to prevent short circuit at the step [36]. In another one of their publications, they have also reported the effect of variation of reactive gas ratio during the deposition of the oxide layer on the electrical characteristics of the diode. The tunneling response in the MIM diode showed improvement with reduced O$_2$ gas ratio. They have concluded that an excess of O$_2$ ions improves the tunneling response, as well as a deficiency of O$_2$ ions due to charge transport by ions or vacancies [37].

Araghi et al have studied the photopolymerizable surfactant 10;12-pentacosadiynoic acid (PCDA) at the air–water interface through a combination of surface pressure–area compression measurements and Brewster angle microscopy imaging during the time course of UV photopolymerization [38]. Bardosova et al have presented the photopolymerization of an amphiphilic compound containing a biphenyl group which has, at one end, a fumarate propyl ester and, at the other, a vinyl group. They polymerized the compound while it was spread as a monolayer at the air/water interface and then assembled it into multilayer structures by the Langmuir-Blodgett technique. They have also polymerized the monolayers among themselves after transfer of films onto the substrate [39].

Choi et al have fabricated devices with Au/Arachidic acid/Al (MIM) structures, with 9-21 monolayers of Arachidic acid. Also, they have presented the I-V characteristics for this device between -3 to +3V.

12

The insulation property of a thin film is better as the distance between electrodes is larger [40]. Hino et al have discussed the performance of an MIM structure consisting of a nonpolar LB film sandwiched in between Al and Au metal layers. They have also analyzed and reported the electrical properties of metal-insulator-metal devices composed of polyimide based Langmuir Blodgett films [41].

Iwamoto et al have reported the use of the Langmuir Blodgett technique for organic molecular assembly to fabricate precisely ordered functional molecular systems. They have used Cadmium arachidate Langmuir Blodgett multilayers in metal-insulator-metal diodes to perform I-V measurements among other electrical characterizations [42]. In another paper Iwamoto et al have investigated the electrical properties of polyimide films in between Al or Au or Pb-Bi metal electrodes [43].

Nijhuis et al have described a procedure to fabricate tunnel junction arrays using self-assembly methods over which they use a liquid top contact in microchannels. The other metal electrode in their structures is obtained using template stripping. They have reported a yield of 70-90% among these tunnel junctions. The structures fabricated using these techniques also included self-assembly of alkanethiolates with ferrocene. Large values of rectification ratio were observed for these tunnel junctions (90-180). [44]

Metal/insulator/metal tunnel junctions incorporating Langmuir Blodgett monolayers of polyimide in between aluminum and gold electrodes have been reported by Hing. He states that the MIM gives electrical energy to the applied voltage source, and that MIM Itself is a power source, in particular, a current source. However, the power source is considered to release electrical energy as a result of absorption of thermal energy from the surroundings.[45]Kaneko et al have studied the electrical characteristics of metal-insulator-metal as well as metal-insulator-semiconductor diodes incorporating

13

polydiacteylene in the form of insulating monolayers. As a part of these experiments, polydiacetylene films were deposited using the Langmuir Blodgett technique. They observed Schottky type current characteristics in the MIM structures, and measured the thermally stimulated currents (TSC) of MIM diodes with single and multiple layers of Polydiacetylene. Capacitance vs. voltage measurements were also performed for A1/LBPDA/Si (MIS) structures. Their C-V curves for the MIS structures have shown hysteresis.[46]

2.1.1 Langmuir Blodgett Thin Film Deposition

Gareth Roberts has published a significant amount of scientific literature discussing the deposition and formation of monomolecular films on substrates, the technique that is commonly known as Langmuir Blodgett films. His work has additionally summarized the preceding contributions of Benjamin Franklin, Lord Rayleigh, Agnes Luise Wilhelmine Pockels, Irving Langmuir, Katharine Blodgett and Hans Kuhn. Hans Kuhn's groundbreaking work on energy transfer also marked a strong base for further development of artificial systems of cooperating molecules transferred onto solid substrates. He has presented a detailed description of a variety of polymeric, monomeric, organic and inorganic molecular films that can be deposited using the Langmuir Blodgett technique [47].

Galletti et al have discussed the orientation and organization of molecular assemblies in the case of Langmuir Blodgett thin films. They have presented it in the context of both monolayer and multilayer assemblies, while describing the ideal deposition conditions of surface tension and phase of the molecules on the subphase. This report also includes the stability analysis of vinyl stearate monolayers and multilayers while describing the influence of subphase temperature, barrier displacement rate before and after reaching the deposition conditions, and the casting solvent selected for the particular experiment. While maintaining the displacement rate of the barriers between 1-7 cm per min, Galletti et al have reported the temperature of the subphase to be the most critical parameter affecting the

14

isotherm profile and stability of the monolayers, such that the effect of temperature on the isotherms obtained for the material was analyzed as a part of their study [48].

In order to reduce the pinhole defects or vacancies in the monolayer, several researchers have implemented intermolecular crosslinking or polymerization techniques using exposure to gamma or X-ray or ultraviolet radiation. Ogawa has reported different methods of film characterization for polydiacetylene films deposited using the Langmuir Blodgett technique and later polymerized by X-ray exposure [49].

Kumaki et al have reported their results for 2D film deposition with long chain polymers using AFM characterization. They have also documented their analysis of film integrity and orientation at the molecular level [50].

Aoki et al report the use of the Langmuir Blodgett technique to obtain monomolecular films of polymethyl methacrylate. Their study includes characterization and analysis of these films at a molecular level, in terms of the effect of horizontal or vertical dipping on the orientation of the films, that is a study of the azimuthal angle of the molecular orientation. Their observation reveals how the PMMA chain in an LB monolayer deposited by vertical dipping is weakly oriented in the direction of dipping. In the case of horizontal dipping, the molecular arrangement lacked any form of consistent trend in orientation. [51].

2.2 Design Of A Frequency Selective Thermal Emitter

Modification and tunability of transmission, absorption or thermal emission has gained significant research interest over the past decades. A major portion of related research has been in finding suitable material properties or introducing modifications of material properties for the desired optical characteristics. The other aspect of this research objective looks at surface modifications or structural variations of a photonic crystal to tune the absorption or emission characteristics. Both of these

15

directions have been considered in combination for the purpose of the proposed research, to design a frequency selective thermal emitter. The research also includes an analysis of the impact of dimensional variations on the frequency selectivity of emission/absorption.

Liu et al have demonstrated how selective thermal emitters based on metamaterials can be implemented in the form of perfect absorbers. They experimentally realized a narrow band mid-infrared (MIR) thermal emitter. They have elaborated on a multiple metamaterial sublattice type structure to allow a two band MIR emission. By performing both emissivity and absorptivity measurements, they have also confirmed good agreement between the emissivity and absorptivity as predicted by Kirchhoff's law of thermal radiation [5].

Marquier et al have presented the possibility of coherent emission of light at a temperature T by exciting suface polaritons. They have intensively reviewed the origin of this phenomenon. They have also studied the influence of the microstructure and temperature on the coherence properties. Their article presents the design of a quasi-isotropic source and a very directional source of thermal light [52].

Hasman et al have proposed several micro and nanostructure designs to enhance a material's emissivity and its radiative coherence. They have reviewed the present microscale and nanoscale structures supporting surface waves for obtaining polarization manipulation of thermal emission, extraordinary coherent thermal radiation, bandgap in the spectral emission, spin symmetry breaking of a coupled thermal antenna array, and a broadband infrared absorption. They have also presented experimental results for a quasi-monochromatic and directional thermal source with a spatial coherence length in the far-field that is much larger than the predicted limit related to the surface phonon-polariton coherence of a flat surface [7, 43]. Hesketh et al have shown the use of highly doped, micromachined, periodic structures on silicon for spectral control of emission. These structures have dimensions that

16

are comparable to the wavelengths of the measured radiation. Their measurements show periodic maxima in both the s and p polarized directional spectral emittances in the plane perpendicular to the grating vector due to standing-wave modes in the slots of the grating. They have concluded that these maxima provide detailed information on the characteristics of the electromagnetic modes associated with surface microstructures [54].

Sai et al have discussed thermal emissive properties of microstructured surfaces measured in the near-infrared region. Two-dimensional periodic microstructured surfaces with metal coatings were fabricated with Si anisotropic etching and laser ablation techniques. Clear selective-emission bands were observed experimentally. They have attributed such selectivity of emission to the resonance effect between the emissive field and the surface microstructures. In addition, numerical calculation computed with rigorous coupled-wave analysis (RCWA) has confirmed the emissive performance of the microstructured samples [45, 46].

CHAPTER 3:

METHODOLOGY: MIM DIODE FABRICATION USING LB FILMS

As mentioned in the previous sections, the design and fabrication of a rectifying device usable at THz frequencies still continues to be a challenge [4,47]. Metal-insulator-metal diodes that work on the principle of quantum tunneling, may be used for high frequency detection or energy harvesting applications. However, for electron tunneling to take place, it is very critical to maintain an ultrathin insulating layer in between the metal electrodes [47–50]. In addition to maintaining a precise thickness control, it is also critical to ensure that the deposited insulator is pin hole free and conformal to the underlying metal layer. Often times, in spite of successfully avoiding most pinhole defects in the insulator, physical damage caused during top contact deposition causes the device to fail. Thus, characterization of the insulating layer to minimize defects, and improvisation of the metal deposition process to reduce damage during the top contact deposition are two extremely important process steps in the fabrication of an MIM device.

3.1 Langmuir Blodgett Thin Film Deposition

The Langmuir Blodgett (LB) thin film deposition technique is based on the orientation or behavior of dispersed organic molecules at the air-water interface. The idea for an LB film originated in 1773 when Benjamin Franklin dropped about a teaspoon of oil into a pond. He observed that this led to a sudden calming of the waves and the effect could be seen up to about half an acre. Later, Agnes Pockles, Katharine Blodgett and Irving Langmuir contributed significantly to useful research on this phenomenon. Irving Langmuir also received a Nobel Prize in 1932 for his commendable work and contributions in the development of the Langmuir Blodgett deposition technique. It was well

established by then, that a surfactant dispersed onto water would spread on the surface of water until it formed a single monolayer of surfactant molecules. The integrity as well as spread of this surfactant could be controlled by monitoring the surface tension of the underlying water. The organic molecules align themselves to attain the minimum free energy between the gaseous and liquid phase [62]. In this way an insoluble monomolecular layer is formed at the air-water interface.

An appropriate selection of materials is important to ensure a compact Langmuir film deposition onto the substrate. The molecules of a LB suitable material, would be amphiphilic in nature. These molecules are hydrophobic in one part and hydrophilic in the other part. This characteristic allows the molecules to be partly immersed in the subphase (the liquid on which the molecules are dispersed in an LB trough) while the hydrophobic part of the molecule sticks out in air.

When the surfactant concentration is under a certain limit, the molecules spread out on the surface and arrange themselves as shown in Figure 4. This concentration limit is also called the critical micelle concentration. At a concentration above the critical micelle concentration level, the molecules would begin to lump together and form micelles or aggregate clusters. The self-orienting mechanism is due to the molecular tendency to attain a reduced surface energy state.

In the experimental apparatus, a KSV NIMA Langmuir Trough setup is being used. This setup consists of a trough that is filled with the subphase on which the molecules are dispersed using a microliter syringe. There are two barriers symmetrically placed on each side of the trough.

The orientation of surfactant molecules on the liquid surface can be analyzed using the surface tension measurements made by a wilhemy plate immersed in the subphase. Water is the most commonly used subphase in LB film deposition experiments.

The material to be deposited is dissolved in a polar organic solvent such as chloroform or hexane, before it is suspended onto the surface of water or any other subphase. After the solvent has been

allowed to evaporate for 20-30 minutes, the barriers are brought closer to compress the molecules dispersed at the air-water interface. The barrier speed may be varied, but for better accuracy, this speed is kept to a very low 1mm/min.

Film integrity can be clearly monitored based on a surface tension vs. film area isotherm that is generated real time during the compression process. Several such isotherms are obtained for different volumes of material dispersed onto the water surface. The ideal sample volume is identified based on the isotherm characteristics, such as a clear break point in the isotherm showing the collapse of the

a) Deposition material introduced on subphase (water)

b) Molecular arrangement made compact by barrier compression upto ideal surface tension to obtain a perfectly packed monolayer assembly

c) Substrate dipping for transfer of a compact monolayer
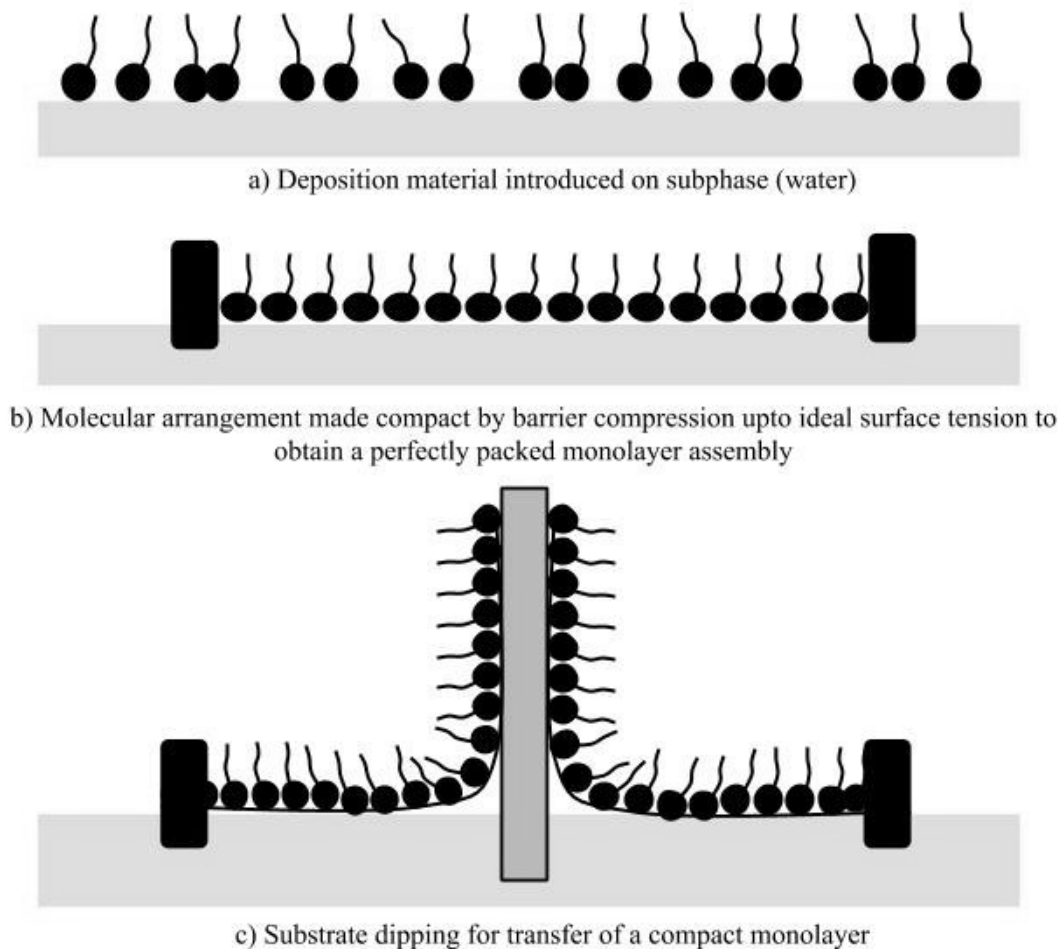
Figure 4 Schematic representation of the molecular arrangement, barrier compression and substrate dipping in Langmuir Blodgett thin film deposition.

20

film on any further compression. This shows that the molecules can be compressed to an ideal compact film state, and the surface tension must be maintained at a point right below the break point observed in the isotherm. Once this surface is maintained, in other words, a compressed film is obtained at the air-water interface, the substrate is then lowered into the water at a speed of 1mm/min. As the substrate dips below the water, the film transfers from the air-water interface to the surface of the substrate. Of course, the hydrophobicity and the hydrophilicity of the substrate have a significant impact of the film adhesion in such a process.
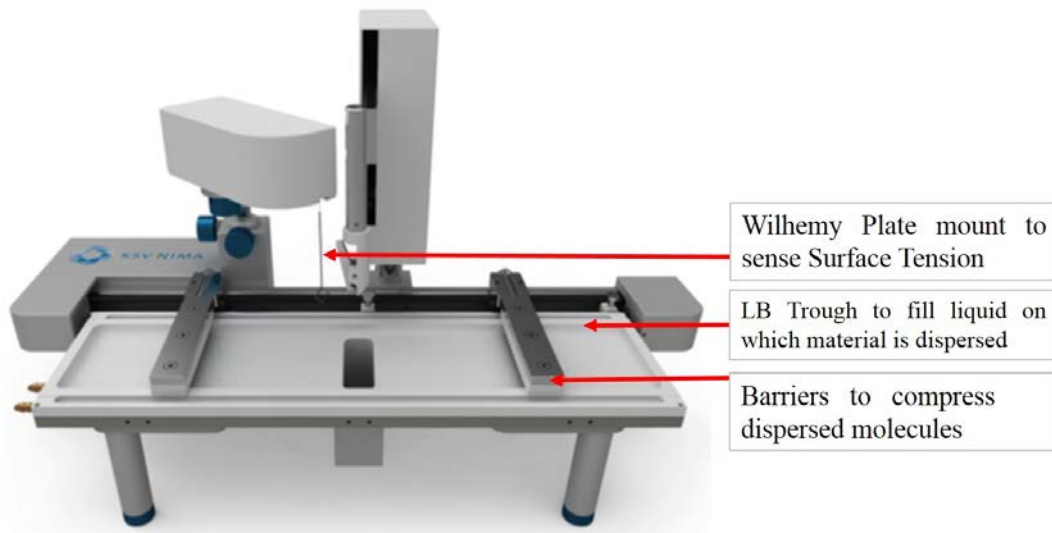
Figure 5 An image showing the KSV NIMA Langmuir trough setup.

3.2 Organic Insulator Based MIM And MIIM Diode

During the course of this research, organic insulator based MIM diodes are being fabricated using the Langmuir Blodgett (LB) technique. This technique allows the deposition of a monomolecular layer of a desired insulating material on any solid substrate. Subsequent repetitions of dipping the substrate into the LB trough, allow multilayer insulator deposition. Thus, an optimized molecular assembly of the desired insulating material can be laid down with minimal pinhole defects and precise thickness control using this process. Photopolymerizable dielectric materials such as 10,12-pentacosadiynoic acid, vinyl stearate, ω-tricosanoic acid will be used as insulating materials with the LB deposition

process for two important reasons [52–54]. The first criteria of material selection is to ensure that the molecules are amphiphilic in nature, and align themselves in an orderly manner on the surface of water in the LB trough. This allows for the formation of a compact and highly uniform film when the molecules are compressed between the two barriers in the trough. The second criterion, for such choice of materials, is the capability to polymerize insulating monomers with exposure to ultraviolet light. This UV initiated polymerization reduces the inter-molecular spacing between monomer chains on the surface of water. As a result, pinhole defects can be minimized to a huge extent using an appropriate selection of materials and process optimization.
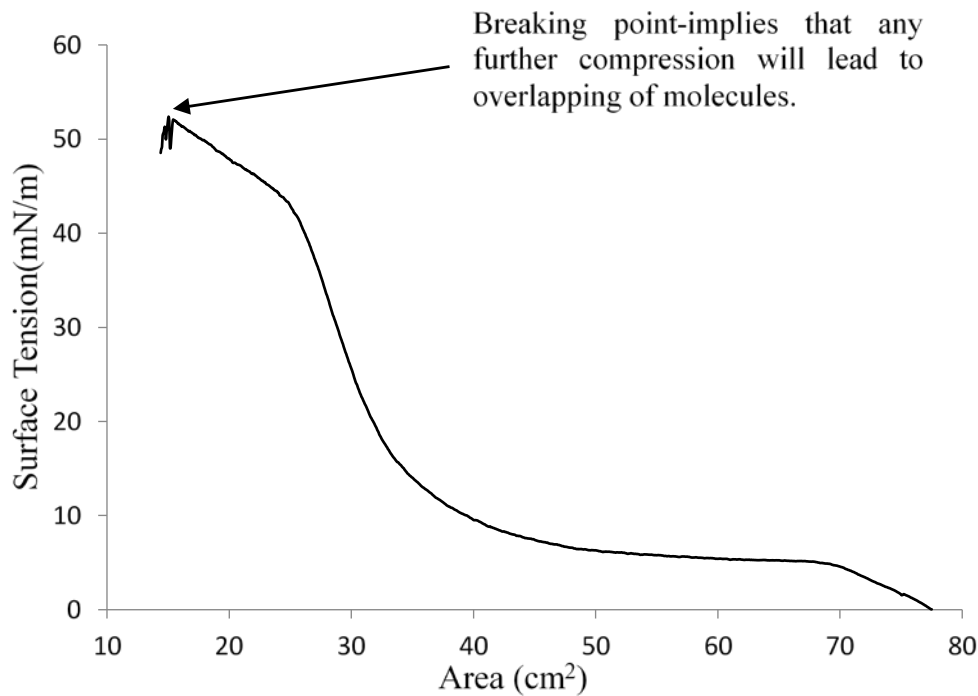
Figure 6 An example of surface tension-area isotherm to monitor film compression at the air-water interface.

One of the major challenges with LB films is that of the stabilization of a several monolayer assembly, which is related to different factors such as deposition conditions, nature of both substrate and constituent molecules and the composition of the subphase, including the presence of certain heavy-metal cations. Indeed, LB films are very easily damaged by ageing, by heating, by many chemical

22

solvents and by mechanical action. In order to understand the properties and the behavior of these systems it is necessary to characterize, down to the nanometer level, the organization as well as the chemical composition of the organic film, the solid substrate and the interface region [65].

(a) Self Assembled Monolayer

(b) Top metal contact deposition on Self Assembled Monolayer
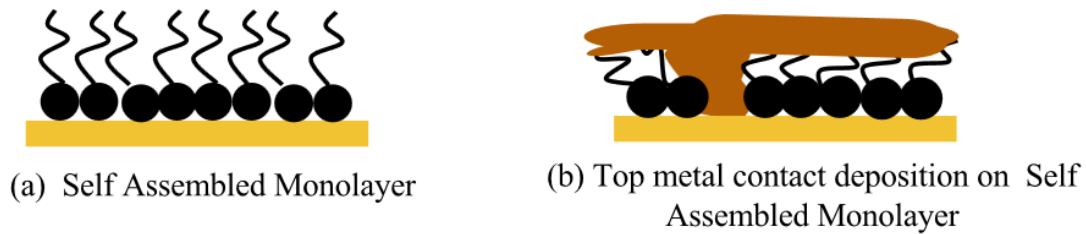
Figure 7 Top contact deposition challenge in self-assembled monolayer based MIM/MIIM diodes.

To fabricate a resonant tunnel diode (M I_1 I_2 M configuration), using the same process, an insulator will be deposited using the LB technique. This will be followed by UV exposure to polymerize the deposited monomolecular layer(s) to allow crosslinking between the individual monomers. The second insulator material will then be deposited by repeating the same process steps.

METHODOLOGY: DESIGN AND FABRICATION OF A NARROWBAND THERMAL EMITTER

Bulk thermal sources are known to suffer from lack of coherence and directionality. A multi-material structure with periodic features on the surface may be used to design a frequency selective emitter and overcome such limitations. Surface modification leads to excitation and coupling of surface plasmon modes, thereby altering optical properties of the crystal [15]. Thus, it is possible to tune the emission spectrum, according to the desired application, with the help of surface patterning of a periodic grating on a layered metal-dielectric structure. Microstructures of sub wavelength dimensions when etched onto a photonic crystal allow such application specific tailoring of the emission spectrum.

The presence of sub-wavelength features on the metal surface causes enhanced electromagnetic fields due to localized electron oscillations at the surface. This leads to a change in the optical properties of the patterned crystal.

During experimentation, the emittance of the thermal emitter can be found using the ratio of radiation emitted from the sample at a temperature T, to the radiation emitted from a blackbody at the same temperature T. For theoretical calculations, the concept was formulated on the basis of fundamental conservation of energy at the macroscopic level and Kirchhoff's law of thermal radiation.

$$\Phi_{incident} = \Phi_{reflected} + \Phi_{absorbed} + \Phi_{transmitted}$$

For opaque surfaces, the transmittance maybe ignored, and this was ensured by considering a metal ground plane at the back of the photonic crystal structure. Using Kirchhoff's law, in thermal

24

equilibrium, the emittance of the designed emitter must equal the absorptance, giving, ε =1- ρ. The reflectance in this relation can be obtained from the S_{11} values in a two port setup while modeling a photonic crystal. Computer Simulation Technology (CST) allows electromagnetic wave simulations using the Finite Integration Technique (FIT), rather than the classic Finite Element Method or Finite Difference Time Domain (FDTD) method. The simulations facilitate fast and easy analysis of the effect of material parameters as well as dimensional variation in the photonic crystal. The basic structure of a periodic hole array as modeled in CST is shown in Figure 8.
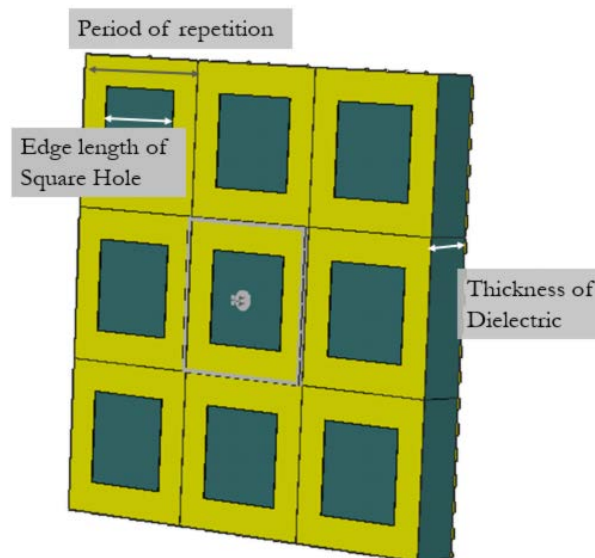
Figure 8 An emitter model showing a sub wavelength periodic square hole array.

4.1 Frequency Domain Solver Using The CST Microwave Studio

The frequency domain solver of the CST MICROWAVE STUDIO analyzes electromagnetic near and far fields as well as S-Parameters. The Frequency Domain Solver is considered preferable over time domain solvers, especially when dealing with electrically small structures, or devices with a high Q-value.

As a unique feature, the frequency domain solver in CST MWS can be switched from Cartesian to tetrahedral meshing. Besides segmented representation of curved surfaces, a true surface mesh as

25

shown below increases the accuracy and speed. Mesh optimization, ideal boundary conditions, geometry adaptation are some of the modeling considerations that must be accounted for.

Mesh refinement of traditional tetrahedral frequency domain solvers does not improve upon the initial facetted representation of the structure. CST's True Geometry Adaptation projects the refined mesh back onto the original model to achieve higher accuracy.

Broadband results are provided quickly with the built-in adaptive frequency sweep. For both mesh types automatic mesh adaptation schemes are implemented. The frequency domain solver in CST MWS offers a direct and an indirect linear equation system solver. The direct one is preferable if the number of tetrahedrons is not too large; it shows its main strength when the full S-matrix of a structure with multiple excitations is required.

A key application of the Frequency Domain Solver is periodic structures, such as photonic band-gap (PBG), frequency selective surfaces, or phased arrays. CST MWS features a special periodic boundary implementation, which automatically creates the boundaries for arbitrarily shaped unit cells.

Such an approximation with tetrahedrons was utilized to obtain the S parameters for metallo-dielectric periodic arrays. Later, the transmissivity, reflectivity and absorptivity were derived using the S Parameters. These values of α, ρ, τ were used for the ϵ calculations to determine the selectivity of emission that can be achieved with subwavelength periodic nanostructure arrays.

4.2 Process Flow For Thermal Emitter Fabrication

The patterning of the photonic crystal involves the use of conventional photolithography. To begin with, a silicon wafer was sputter coated with a thin film of Nickel. This was followed with basic photolithography steps such as coating photoresist spinning, baking, UV exposure and development. A deep reactive ion etching (DRIE) process was used to etch the underlying silicon substrate.

26
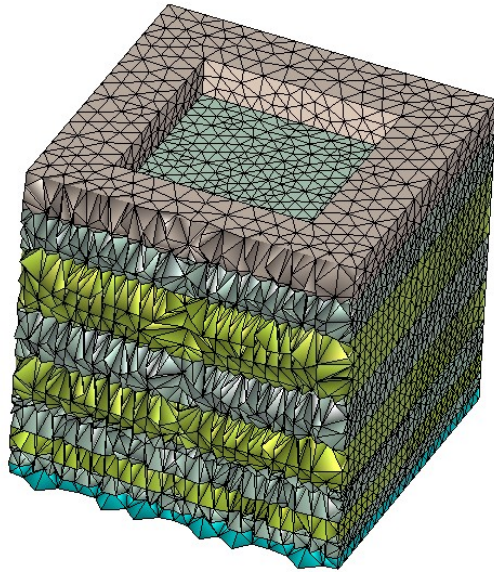
Figure 9 Model representation of a tetrahedron mesh generated in CST to simulate the emissivity spectrum of a square hole array structure.

(a) E-beam Evaporation of metal coating

(b) Spinning Photoresist followed by soft bake

(c) UV exposure and development of resist

(e) Lift off metal Patterning

(f) Deep Reactive Ion Etching

(g) Photoresist stripping

Figure 10 The process flow used for the fabrication of periodic grating structures for thermal emitter applications.

27

CHAPTER 5:

RESULTS: LAYER BY LAYER AND DEVICE CHARACTERIZATION FOR MIM DIODES

The proposed MIM structure involves a layer by layer deposition of the metal, and insulator layers followed by a confined top contact sputtering. While fabricating this assembly, a silicon wafer was used as a substrate, with a passivating oxide layer on the surface of the wafer for proper device isolation. This was followed by the sputter deposition of Nickel onto the silicon substrate.

In the sputtering process, atoms are ejected from a target material upon bombarding it with high-energy particles. The atoms ejected from the target uniformly coat the surface of the silicon substrate in the form of a thin film. Such deposition takes place in a vacuum environment (mTorr range) where an electric field between the cathode (target) and anode (substrate) creates a plasma in the form of Ar^+ ions that are used to bombard the target. The rate of Ni deposition is known to be dependent on the pressure inside the sputtering chamber, the ion energy (proporti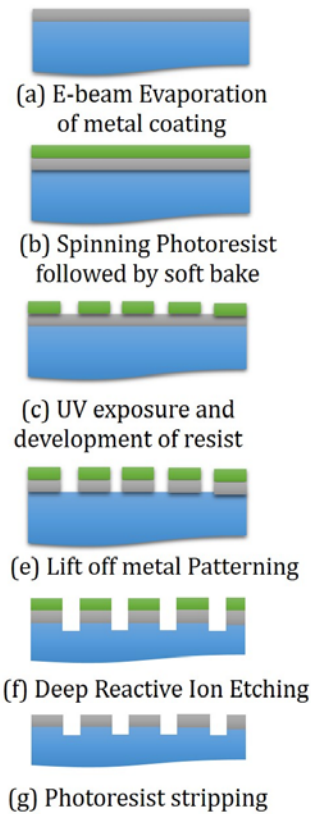onal to the RF or DC power), and the amount of Argon flow into the sputtering environment. These parameters were varied to get smooth Ni film depositions of 20nm ±1nm at a feasible rate.

The roughness of a 100nm x 100nm area of the deposited thin Nickel film was measured with the help of an atomic force microscope to give an rms value of 8.8Å. Bruker AFM probe tips (0.01-0.025 Ohm-cm Antimony (n) doped Si) were used for all AFM measurements in tapping mode. The Argon pressure was maintained close to 3 mTorr during this deposition process, and the RF power was set to 100 Watts.
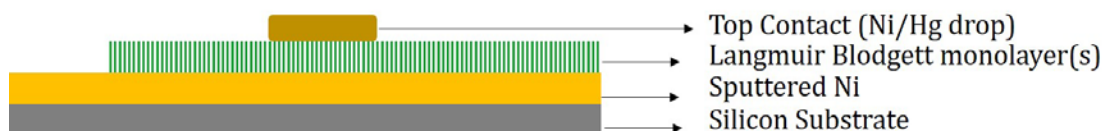
Figure 11 Schematic representation of the layer by layer MIM assembly.

Insulating monolayers can be deposited using the Langmuir Blodgett technique as described in the previous sections. Fatty acids were mostly selected for this research due to their amphiphilic nature which is a key requirement for the Langmuir Blodgett technique. MIM diodes were fabricated with Vinyl Stearate, 10,12-Pentacosadiynoic Acid (PDA), 5,10,15,20-Tetrakis(4-hydroxyphenyl)-21H,23H-porphine, ω-Tricosanoic acid, and Arachidic Acid monolayers as insulators.
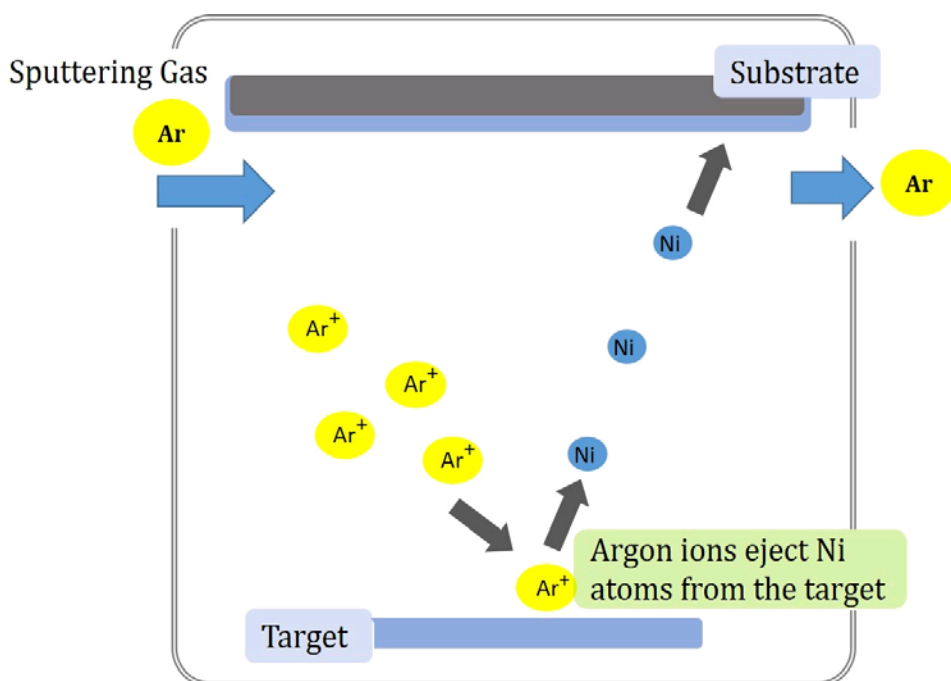
Figure 12 A schematic representation of Ni film deposition using the sputtering process.

The Langmuir monolayer behavior of these materials was first studied at the air-water interface to find the ideal surface tension of water for a close packed film. This was followed by the film deposition on silicon, ITO glass plate, quartz and nickel for optical spectroscopy, cyclic voltammetry and electrical measurements, respectively [54,56–58].

29

The optical and electrochemical properties of the films were investigated using FTIR and cyclic voltammetry studies, respectively. The electrochemical analysis of materials has proven useful to understand the chemical activity such as the oxidation-reduction reactions as well as their reversibility. Cyclic Voltammetry was performed on PDA films deposited on indium tin oxide (ITO) coated glass plates to study qualitative information about electrochemical processes, electron transfer rates and understanding of the kinetic and thermodynamic behavior of PDA, which helps with the identification of suitable applications for such materials [69]. The nickel (Ni) - PDA film(s)-Ni structure was studied in order to understand the tunneling behavior in MIM structures.
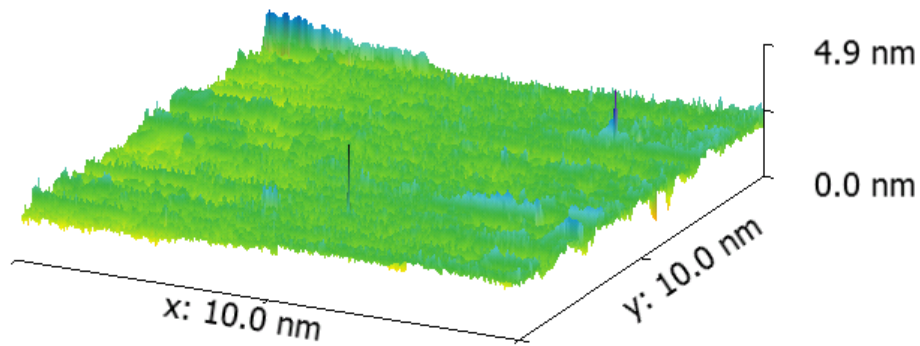
Figure 13 AFM micrograph showing the height profile of a vinyl stearate Langmuir Blodgett film.

5.1 Langmuir Blodgett Deposition Of PDA Monolayer

For these experiments, PDA was obtained from Sigma Aldrich in the form of 10-12-pentacosadiynoic acid ≥97.0% (HPLC grade). A 0.2mg/ml solution of the surfactant PDA was prepared in chloroform (>99.8% from Sigma Aldrich). The pH of water used as subphase was close to 6.8 throughout all experiments. Surface pressure-area isotherms were obtained using the KSV NIMA Langmuir Blodgett Trough system, while using water as a subphase for samples with varying volume and concentration of PDA. The surface pressure was measured using a paper wilhelmy plate suspended into water filled

30

in the trough. The deposition of the PDA monolayer was regulated using surface tension and compression feedback control in a closely packed layer by monitoring the change in surface tension with respect to the position of barriers in the trough. The pressure–area isotherm of the Langmuir monolayer changes with variation in the volume of the PDA solution dispersed on water. The Langmuir monolayer formation is dependent on the concentration of the solution and also the amount of material used. Varying volume samples (6, 7, 8 and 10 microliters) of PDA solution were experimented with, to obtain the best monolayer configuration. Figure 14 shows the molecular structure and UV-polymerized structure of the PDA molecule.

The quality of the monolayer can be determined by monitoring the surface tension and transfer ratio
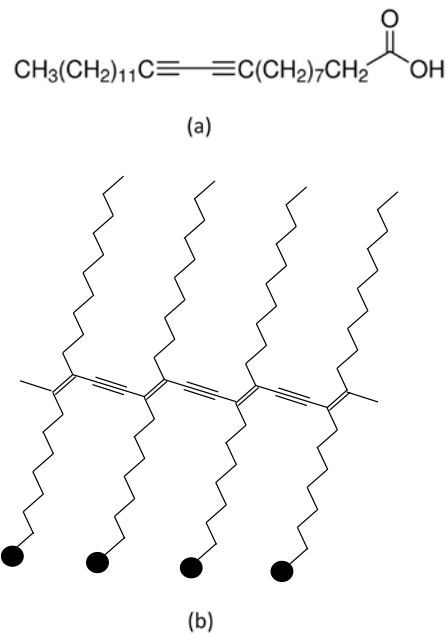
Figure 14 Chemical formula of 10,12-pentacosadiynoic acid is shown in (a) crosslinking among adjacent monomers is shown in figure (b).

calculation for each dipping experiment. Transfer ratio (t.r.) is defined as the ratio between the decrease in monolayer area from the water surface during the deposition stroke and the area of the substrate. A 25 mN/m pressure was selected for the best film configuration while transferring the Langmuir monolayer onto the substrate, after analyzing the isotherm shown in Figure 15. The surface

31

tension, and indirectly the film integrity were efficiently controlled using the KSV NIMA LB trough

controller. For polymerization purposes, the monolayers were exposed to 245nm UV radiation for 15

minutes of exposure time using a UV Bench lamp [70].

Figure 15 Surface tension-area isotherm for the PDA monolayer with and without in situ polarization in the trough. The inset shows that the in-situ polymerization of the PDA film reduces the film surface area by 2.5 cm^2 (15% more compact) close to the maximum confinement before the breaking point.
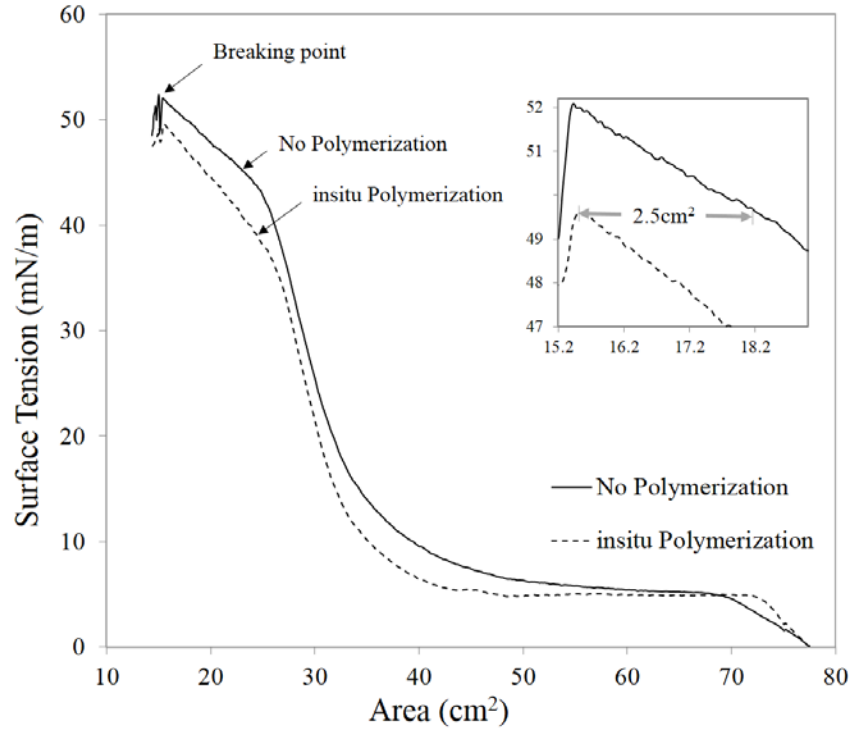
Figure 15 (curve 1) shows the pressure-area isotherm for the PDA Langmuir monolayer, curve 2

shows the in-situ polymerized PDA Langmuir monolayer at the air-water interface. The UV exposed

Langmuir monolayer shows a better compression area per PDA molecule. The compactness of the

film on the surface of the water was found to have been improved significantly with crosslinking of

molecules in the PDA layer using in-situ UV exposure of the film while on the surface of the water in

the trough. A Jasco FTIR 4600 was used to perform infrared (IR) spectroscopy on the PDA film in

the transmission mode. Silicon (Si) (IR transparent) was used as a substrate for the purpose of these

measurements. Figure 16 shows the infrared spectra of 20 PDA monolayers (a) with and without UV

32

exposure (b). The deposition was also performed on an infrared transparent silicon substrate to characterize the material with respect to its absorption peaks. The analysis was carried out on the basis of the difference between the infrared spectra of a UV irradiated sample compared to that of PDA without UV exposure. The peak observed at 1700cm^{-1} in Figure 2 (a) shows pronounced C=O vibration frequencies, the peak at 2300 cm^{-1} could be due to the presence of C≡C vibrations. Stronger peaks were noticed at 2200-2300cm^{-1} for UV irradiated samples [61, 62].

Electrochemical investigation was carried out in a cell containing three electrodes. An indium tin oxide (ITO) coated glass with LS/LB films of PDA was used as the working electrode, platinum as counter electrode and Ag/AgCl as the reference electrode in an HCl electrolyte concentration of 0.01M. The electrochemical measurements were made using a Voltalab PGZ301.

Figure 17 shows the cyclic voltammogram of 20 monolayers of the PDA LB film on ITO coated glass substrates at various scan rates (5, 10, 25, 50, 100, 150 mV/sec) in a 0.01M HCl electrolyte. The PDA shows half–redox characteristics in the CV studies suggesting it is a pseudo- redox material. The redox peak of the PDA LB film shows a distinct shift with an increase in the scan rate from 5 to 150 mV/sec. This peak can be attributed to the cross-linking of the vinyl group caused by the UV-polymerization during the formation of the Langmuir layer (shown in Fig. 1). The vinyl group of PDA polymerized molecules exhibits redox properties while interacting with the HCl molecules in the electrolyte. However, even though it is difficult to calculate the diffusion coefficient, the voltammogram is indicative of the presence of the polymerized vinyl group in the Langmuir monolayer. The PDA molecule (10,12-pentacosadiynoic acid) has pi–bonds which make it electrochemically active besides having carboxylic acid as well. The electrolyte interacts with the pi–bonding resulting in the pseudo redox behavior recorded around -150 to 50 mV as a function of scan rate. The redox properties are not intrinsic to the film and can be attributed to the reaction between the film and the electrolyte.

33

However, this data clearly indicates that polymerized PDA has electrochemical redox properties. In spite of the 'pi-bond' conjugation that provides high carrier mobility there is still a very low concentration of carriers, as can be seen by the insulating behavior of the material [22,23].
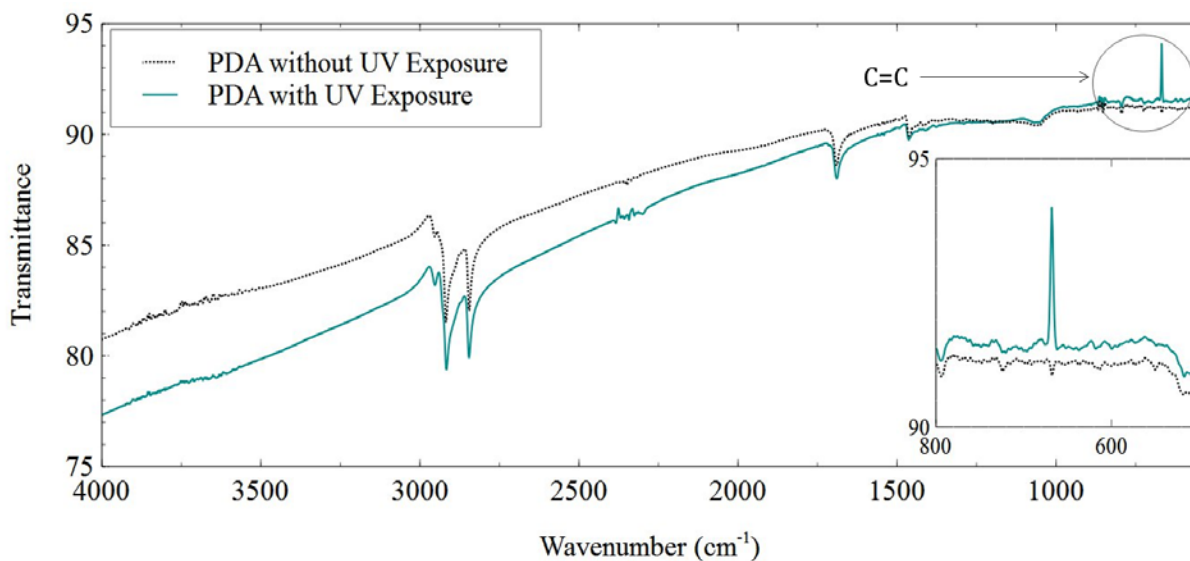

Figure 16 The infrared spectrum of 20 PDA monolayers with and without UV exposure.

The vinyl group of PDA polymerized molecules exhibits redox properties owing to its reaction with the HCl molecules in the electrolyte. However, even though it is difficult to calculate the diffusion coefficient, the voltammogram is indicative of the presence of the polymerized vinyl group in the Langmuir monolayer. Figure 18 shows the relation of the current density with respect to the (scan rate)$^{1/2}$ that is not a straight line, suggesting that these are not completely redox type characteristics. These experiments were conducted with 20 monolayers of PDA deposited using the Langmuir Blodgett technique. As seen in the figure, there is a nonlinear relationship between the current density and the square root of the scan rate for 20 monolayers of PDA on ITO substrates with 0.01M HCl as the electrolyte.
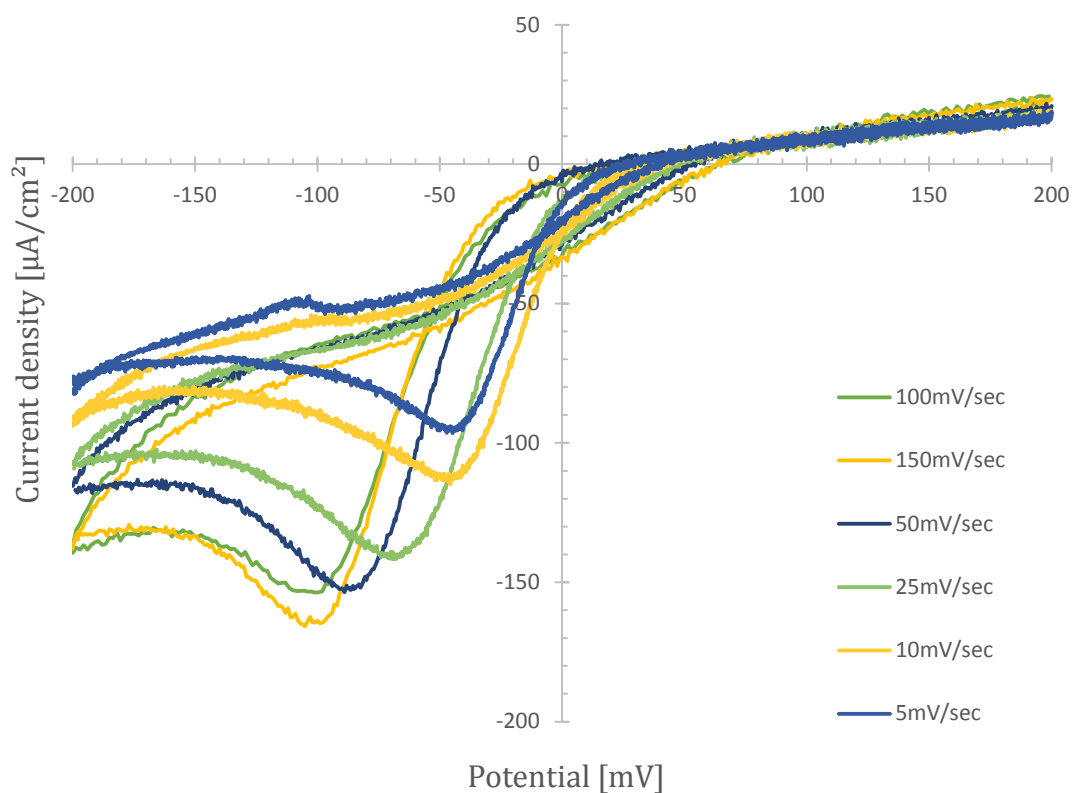
34

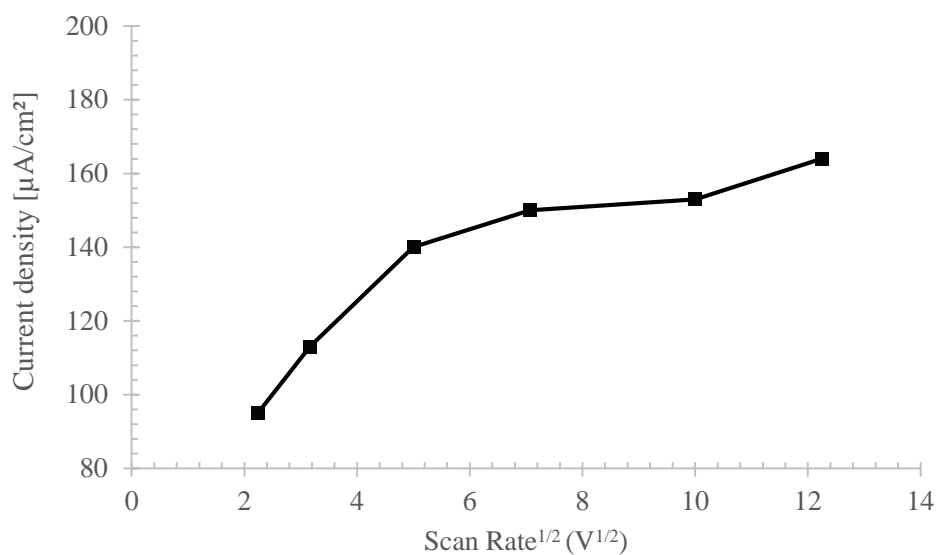Figure 17 Cyclic voltammetry results with varying scan rates for 20 monolayers of PDA.

Figure 18 Current density with respect to voltage scan rate for 20 monolayers of PDA on ITO substrate with 0.01M HCl as electrolyte.

35

The LB films of 10 PDA monolayers were deposited onto a Ni coated substrate using the LB deposition technique [63–65]. For this experiment, 50nm of Ni was sputtered on a silicon wafer with a passivating surface layer of silicon dioxide. The Langmuir monolayer was exposed to 254 nm UV radiation to allow crosslinking of the monomers. A confined Ni top contact was sputtered onto the PDA layers with the help of a shadow mask. To avoid physical damage to the PDA layers, the RF power during sputtering was kept at only 30Watts to sustain enough plasma to allow sputtering of Ni atoms. The current-voltage characteristics of the Ni-PDA-Ni assembly were measured using a micromanipulator setup with Dumet (Cu-Fe) probe tips. The 4145B Semiconductor Parameter Analyzer was used to record the IV measurements.
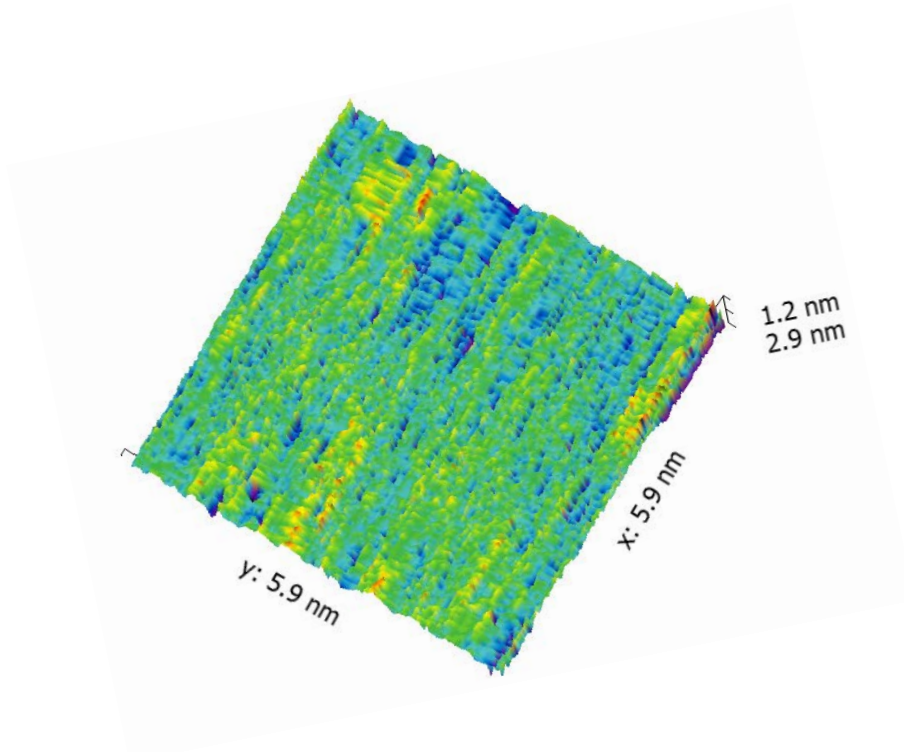

Figure 19 AFM image of 10-12, pentacosadiynoic acid Langmuir Blodgett monolayers (40 monolayers).

The roughness of the deposited monolayers was analyzed using Atomic Force Microscopy. Special Bruker AFM tips (0.01-0.025 Ohm-cm Antimony (n) doped Si) were utilized to scan the film

36

morphology. An average roughness, R_a of 23.7Å, was recorded for a single monolayer of PDA whereas a higher R_a value of 32.3Å was measured for 3 layers of PDA [76].
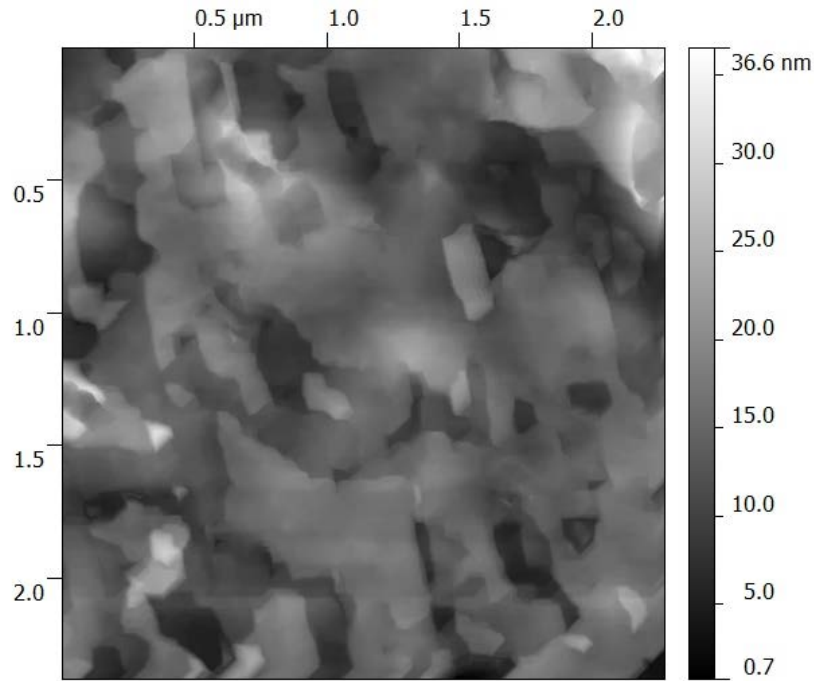

Figure 20 AFM image of 10-12, pentacosadiynoic acid Langmuir Blodgett monolayers (10 monolayers).

Initially, due to the extremely small thickness of the PDA monolayers it was difficult to avoid pinholes, and most MIM devices failed. After polymerization and 20-30 monolayers of insulating PDA, the top contact sputtering caused physical damage to the thin PDA assembly which was observed from the short circuit characteristics obtained with such devices. Reducing the RF power during the Ni top contact sputter runs greatly improved the device fabrication, causing less physical damage and avoiding any significant field effect on the PDA film. Probing on a delicate thin film device was another major challenge. Extended Ni pads were sputtered to allow the probe tip to be applied outside the active area of the device. After such optimization, the I-V characteristics of the Ni-PDA-Ni MIM configuration could be successfully measured.

37

Figure 21 shows a voltage versus diode resistance plot for a MIM diode with 3 insulating monolayers of Arachadic Acid with the diode resistance given by:

$$R(\Omega) = \frac{1}{\frac{dI}{dV}}$$

The breakdown field strength (E_b) of the insulating films deposited using Langmuir Blodgett technique was also computed based on the highest voltage that the device could withstand without being damaged
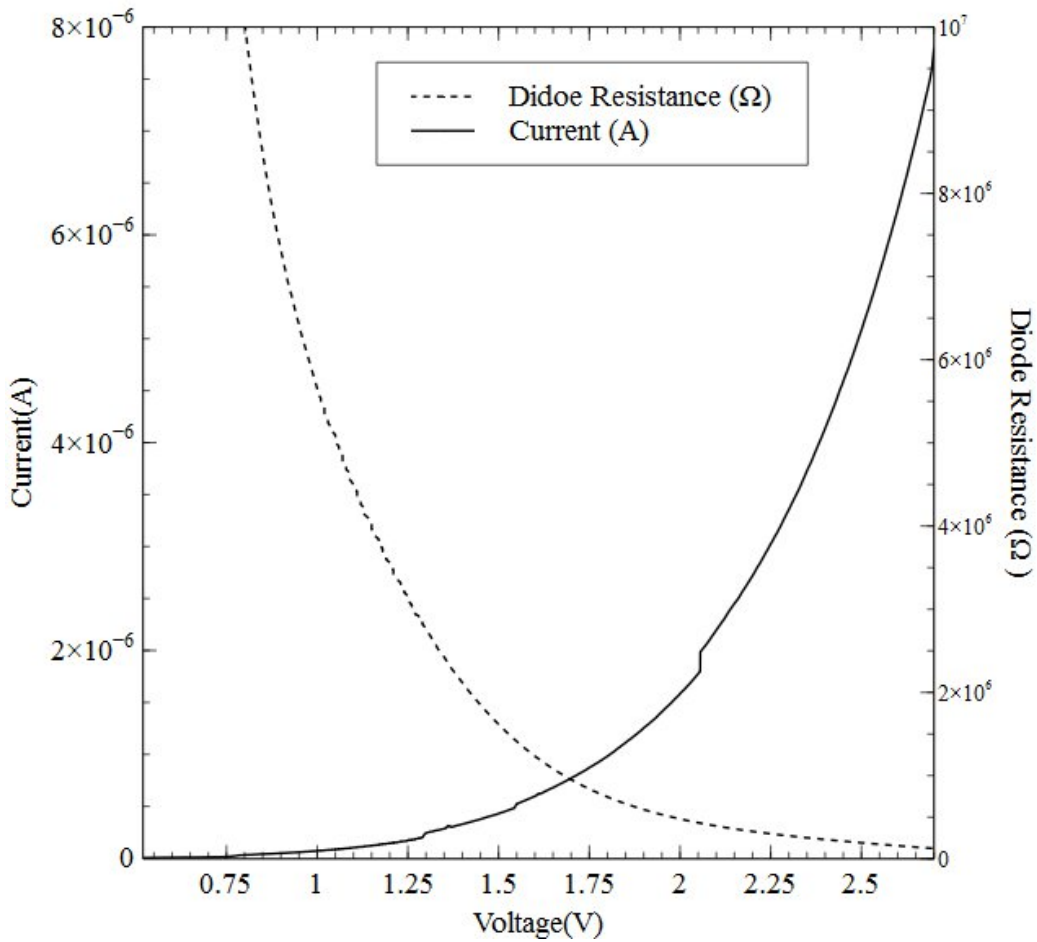
$$E_b = \frac{V}{d}$$

Figure 21 Voltage vs. diode resistance for a Ni-arachidic acid-Au/Pd based MIM diode.
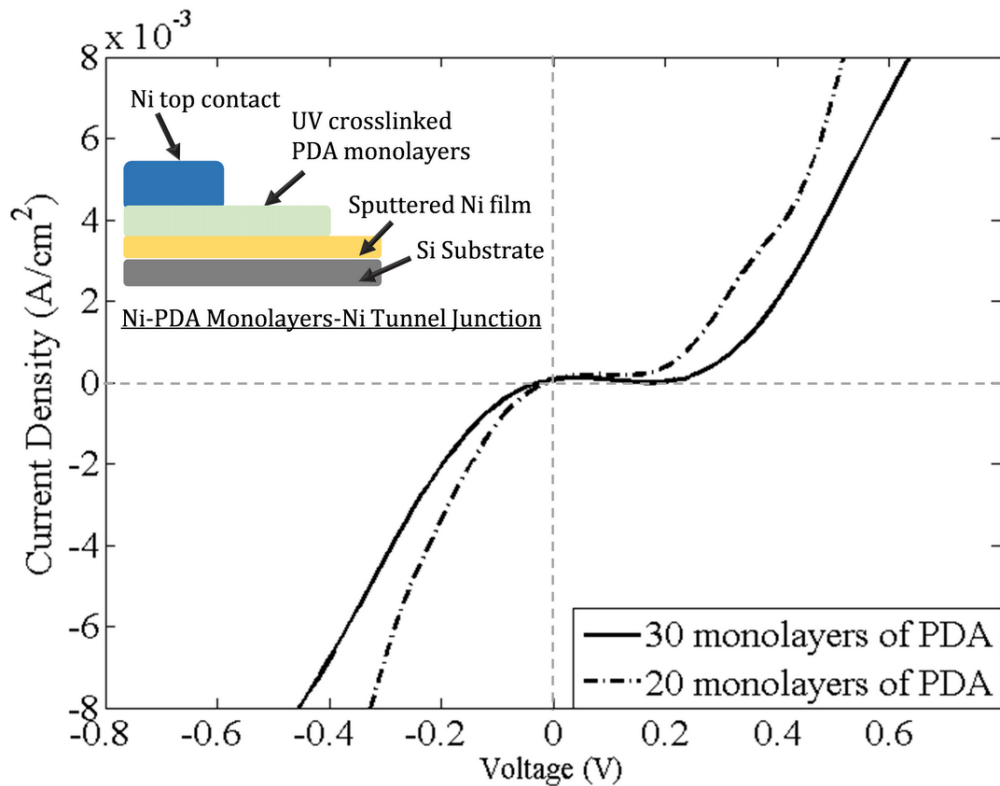
Figure 22 Current-voltage characteristics for a Ni-PDA monolayers-Ni diode with 20 and 30 monolayers of PDA assembly.

Table 1 shows the breakdown field strength observed during I-V measurements for the MIM diode assembly. These diodes were fabricated using multiple layers of tricosanoic acid, arachidic acid and poly-o-anisidine deposited on a metal substrate using the Langmuir Blodgett technique.

Table 1 Observed breakdown field strength during I-V measurements for the MIM diode assembly.

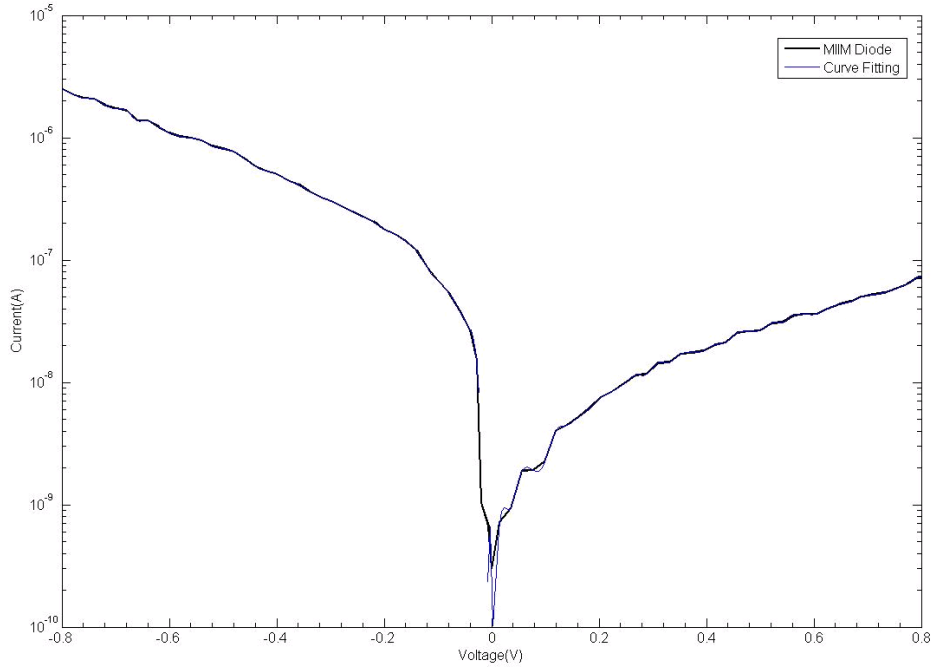| Insulating Material	Breakdown field strength, E_b (MV/cm)
Tricosanoic Acid	2.35 ± 0.03
Arachidic Acid	2.8 ± 0.05
Poly-o-anisidine	4.3 ± 0.05

Figure 23 Semilog plot of the current vs. voltage characteristics for a Ni-arachadic acid-tricosanoic acid-Au/Pd based MIIM diode.

Figure 23 shows a semilog representation of the current vs voltage characteristics of an MIIM diode

with Arachadic Acid and Tricosanoic Acid LB films sandwiched between Ni and Au/Pd metal layers.

This graph also shows a spline interpolation curve fitting with an R square value of 0.976.

Table 2 Summary of rectification ratios calculated for MIM and MIIM diodes fabricated using insulating LB films of arachidic acid (AA) and tricosenoic acid.

Diode Configuration	Rectification Ratio (η)	Voltage
MIM (Ni-AA-Au/Pd)	1:25	100mV
	1:450	200mV
MIIM (Ni-AA-TA-Au/Pd)	1:4	100mV
	1:6	200mV
	1:500	500mV

40

The orientation of the insulating monolayers is very critical since it decides the least attainable distance of separation between the two metal layers in the MIM diode. That is, the Langmuir Blodgett films that are vertically oriented and with a chain length of ~2-4nm as in the case of PDA and Arachidic Acid can only be used to fabricate tunnel diodes with a minimum tunneling distance of ~2-4nm[77], [78]. However, if the choice of materials was further scrutinized to ensure insulating amphiphiles that are always oriented horizontally in the form of a two dimensional lattice, it would mean that we can get Angstrom scale monolayer deposition or a tunneling distance lesser than 2nm [50], [51].

Poly o-anisidine and poly methyl methacrylate were selected as suitable amphiphilic molecules to investigate the feasibility of ultrathin insulating Langmuir films with horizontal orientation. The metal insulator metal diodes were fabricated using the procedure described in the previous sections. The electrical characteristics were measured and analyzed in terms of current density (A/cm^2) with respect to voltage, resistance (Ω) with respect to voltage, responsivity with respect to voltage andrectification with respect to voltage. The rectification ratio at a specific bias voltage, V_b, was calculated as a ratio of currents for an equal voltage deviation around the bias voltage (V_b) i.e.

$$RR = \frac{I_f(\text{at } V_b + V)}{I_r(\text{at } V_b - V)}$$

Figure 24 shows the rectification ratio calculations using the I-V characteristics of the MIM diode, by taking the ratio of the currents at an equal voltage deviation on either side of the bias voltage V_b. The responsivity was also calculated to find the ideal bias voltage for each diode and to compare the performances of different insulating layer combinations that were selected for each MIM assembly. In order to calculate the responsivity, the first derivative dI/dV was obtained from the I-V characteristics as a function of the voltage, as shown in Figure 32 and Figure 38. Then a second derivative of the I-V characteristics was obtained as a function of voltage, as shown in Figure 31 and 39. The responsivity

41

was calculated using the first and the second derivative, given by:

$$Responsivity = \frac{1}{2}\frac{\frac{d^2I}{dV^2}}{\frac{dI}{dV}}$$

Higher responsivity reflects improvement in the rectification ability of the diode[79], [80]. Eliasson et al have reported the use of responsivity as a measure of improvement in small signal rectification[81][82].
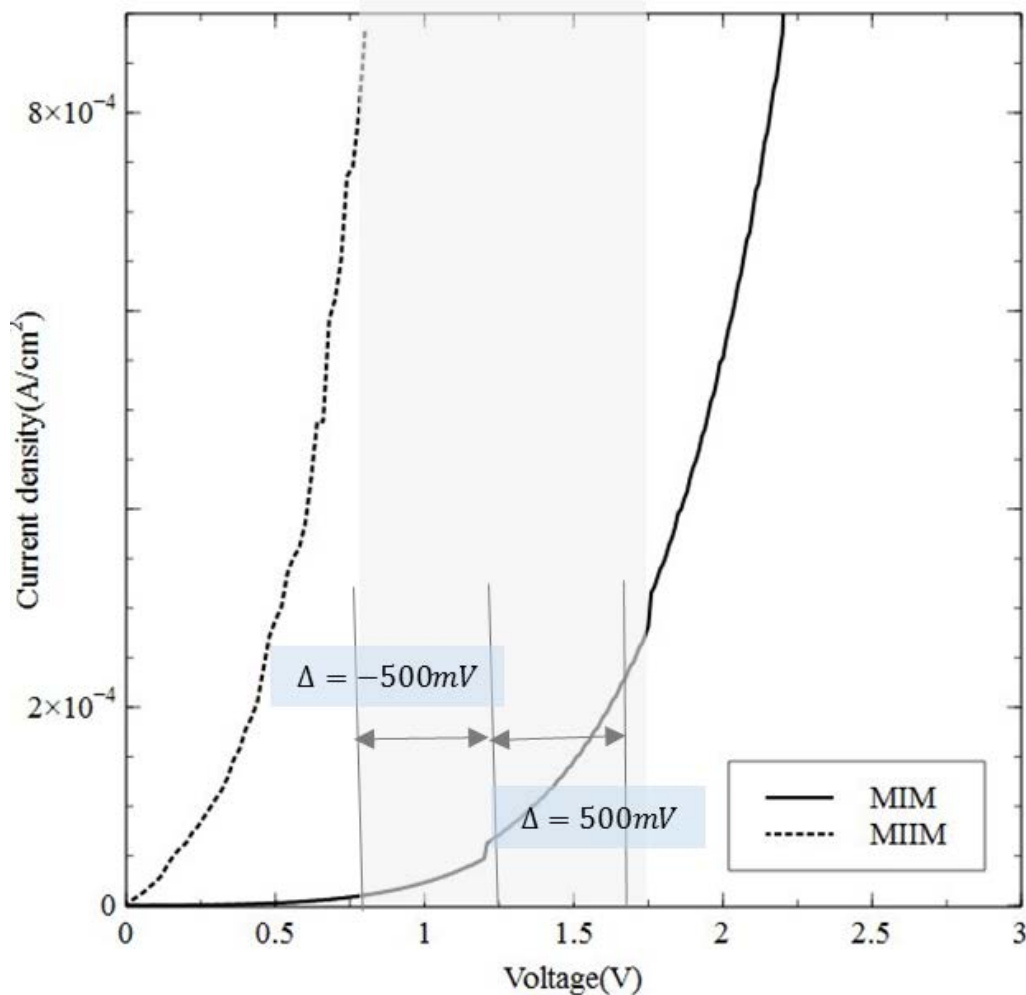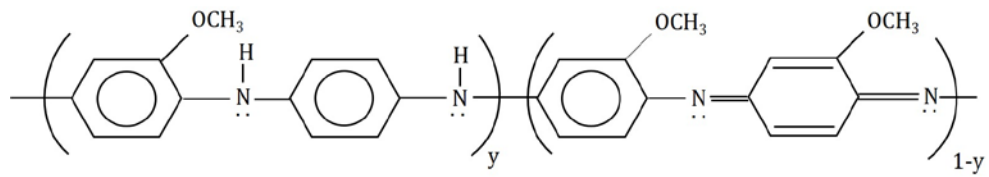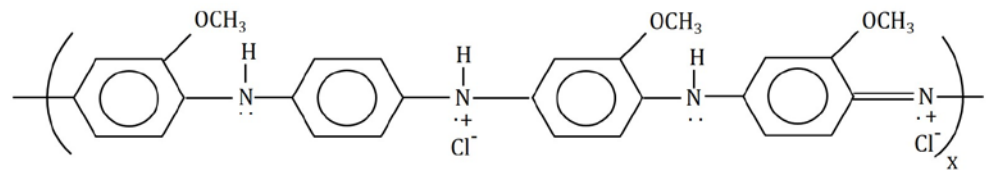

Figure 24 Rectification ratio calculations for MIM and MIIM diodes fabricated using Langmuir Blodgett thin films. The small signal rectification ratio for the MIM diode was calculated as 4:1 at ±100mV and that for the MIIM diode was calculated to be 25:1 at ±100mV for diodes fabricated using arachidic acid and PDA monolayers.

42

(a) Undoped poly-o-anisidine

(b) Doped poly-o-anisidine

Figure 25 Current density-voltage characteristics of Ni-POA monolayers-(Au/Pd) tunnel junction using Langmuir Blodgett technique.

Figure 26 SEM micrographs of synthesized poly o-anisidine at 2000X, 2500X, 3000X and 5000X magnifications.

43
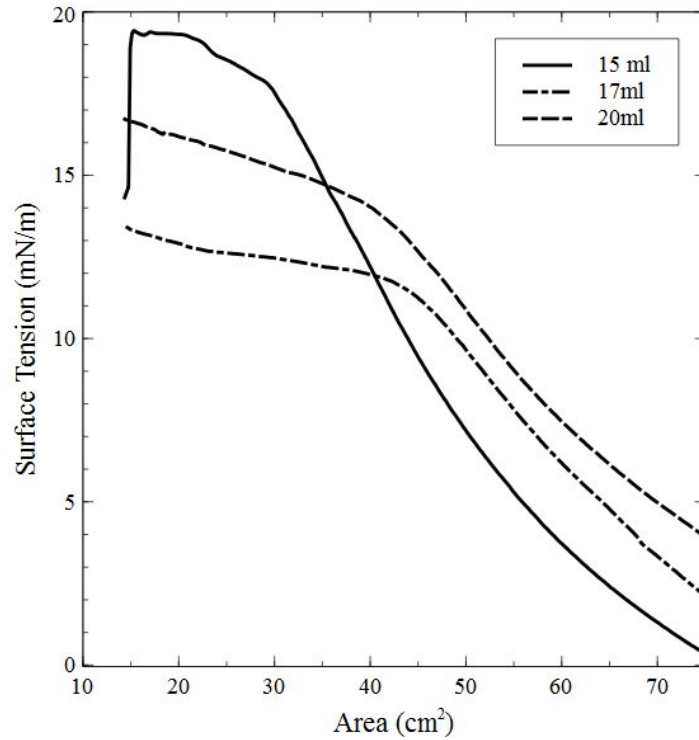
Figure 27 Surface tension vs area isotherms for 15, 17 and 20ml of 0.2mg/ml POA in chloroform obtained for Langmuir Blodgett thin film deposition.
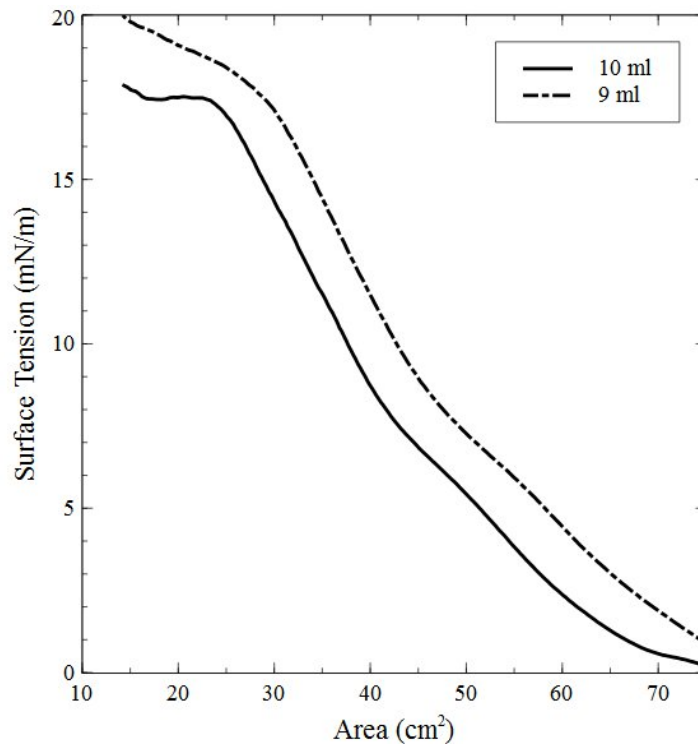
Figure 28 Surface tension vs area isotherms for 9 and 10ml of 0.5mg/ml PMMA in chloroform.
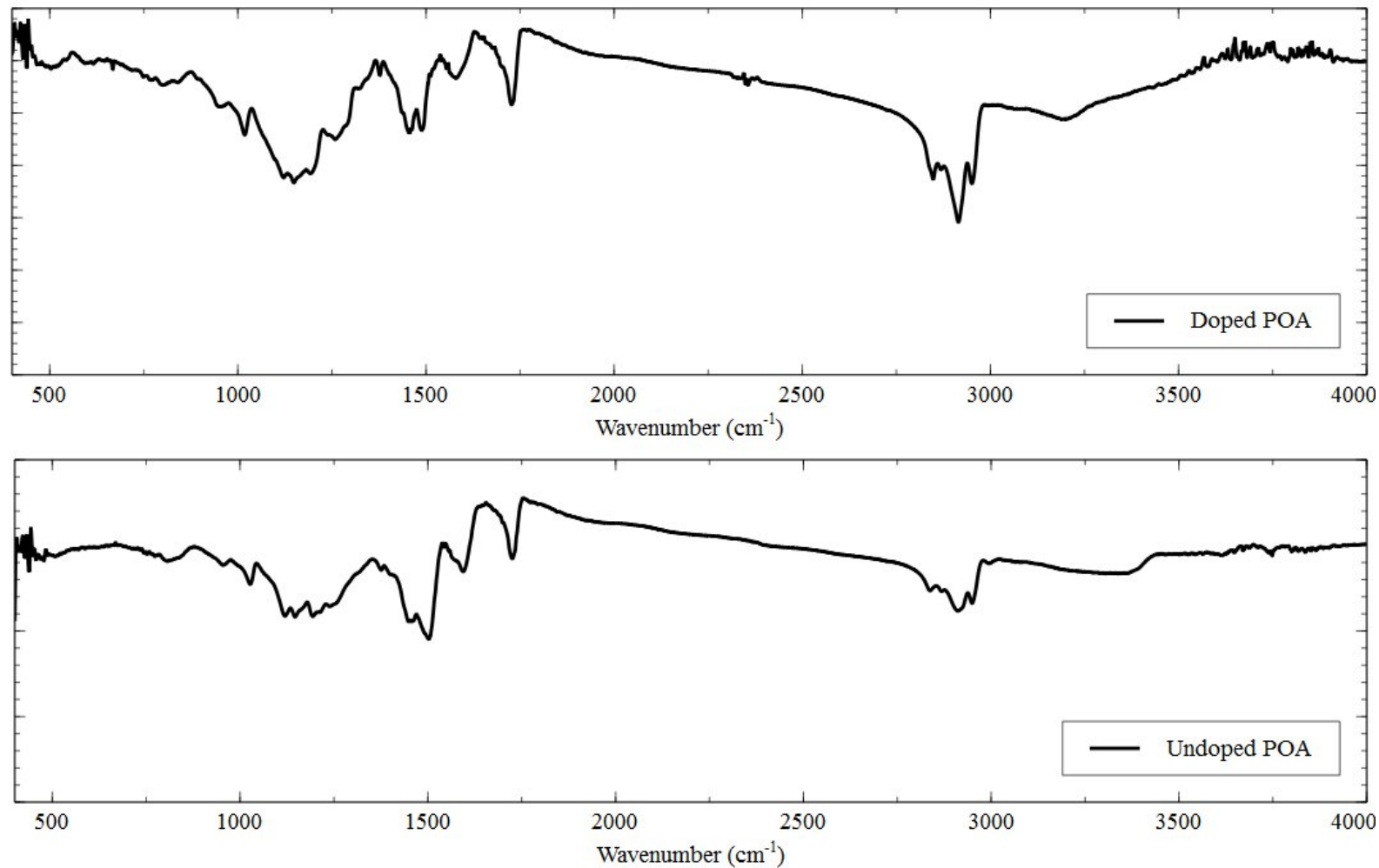
Figure 29 Reflection measurements using IR spectroscopy for undoped and doped forms of POA monolayers
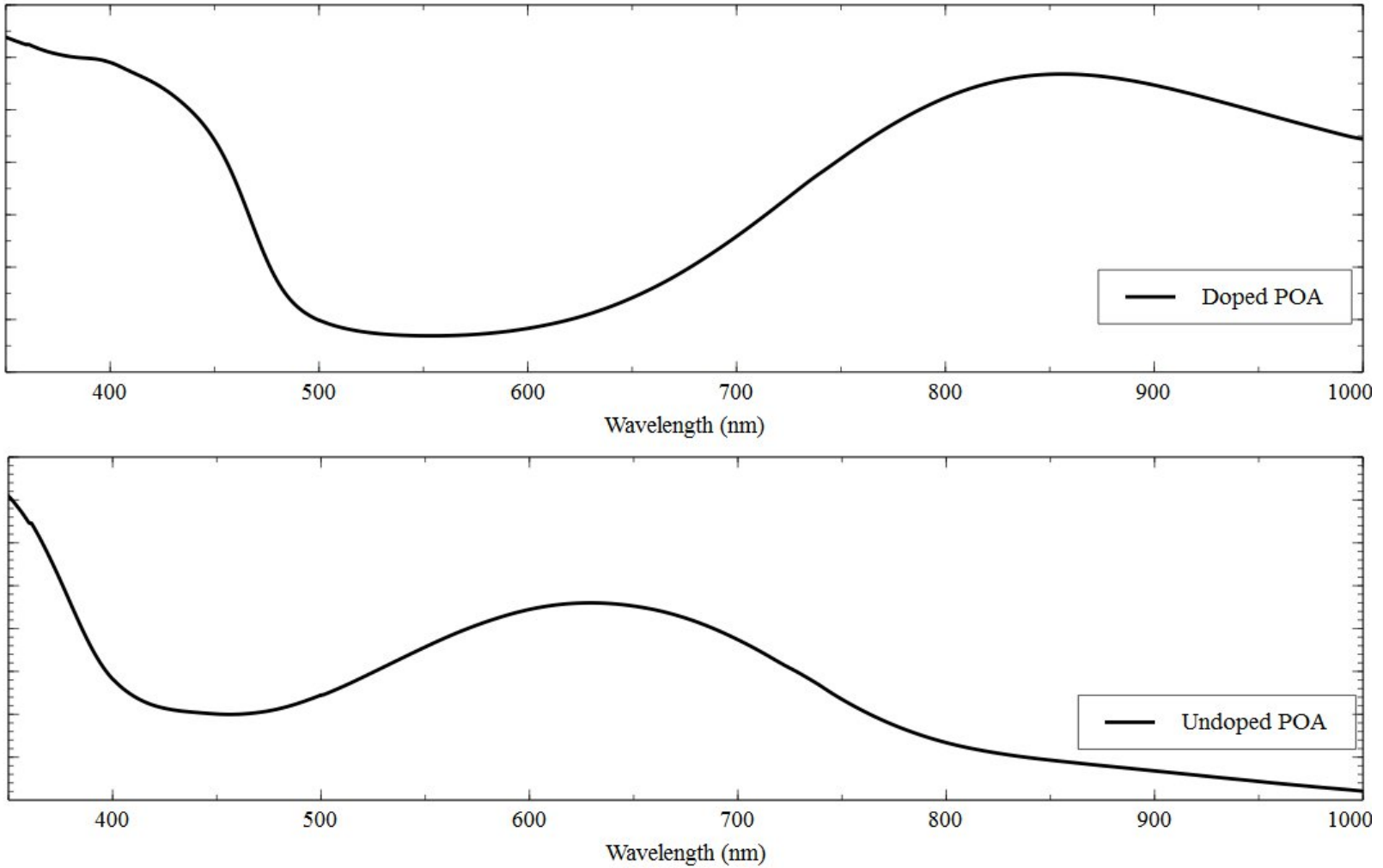
Figure 30 Transmission measurements using UV-VIS spectroscopy for undoped and doped forms of POA monolayers.
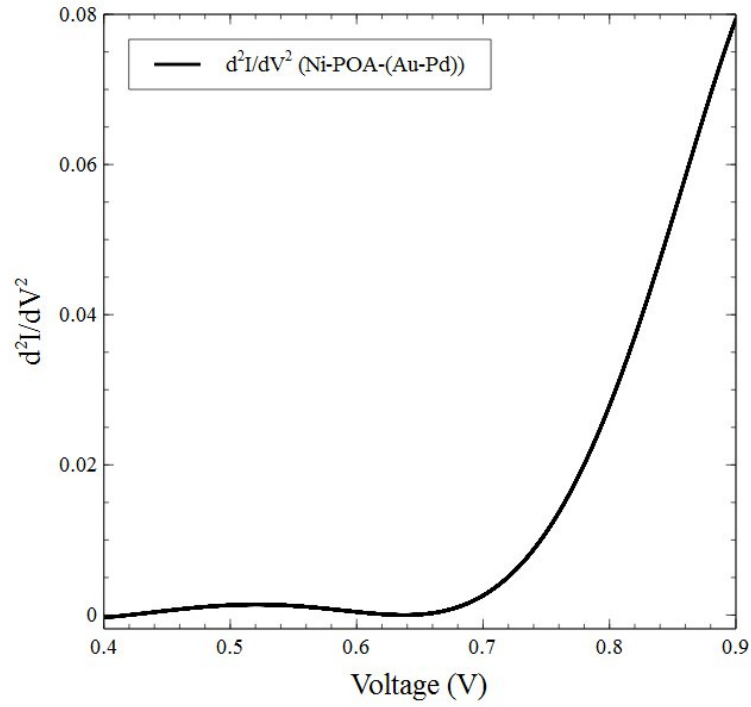
Figure 31 d^2I/dV^2-voltage characteristics of Ni-POA monolayers-(Au/Pd) tunnel junction using Langmuir Blodgett technique.

Figure 32 dI/dV - voltage characteristics of Ni-POA monolayers-(Au/Pd) tunnel junction using Langmuir Blodgett technique.
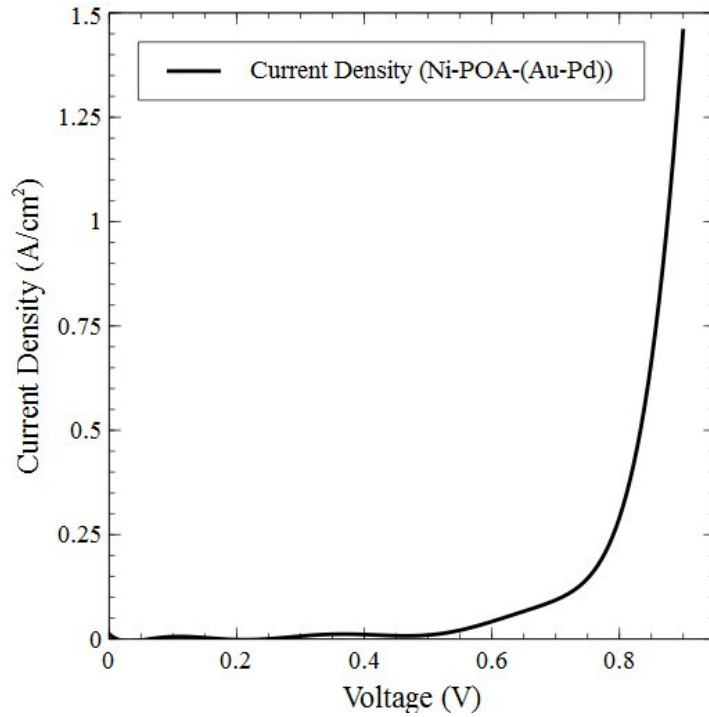
Figure 33 Current density-voltage characteristics of Ni-POA monolayers-(Au/Pd) tunnel junction grown by using the Langmuir Blodgett technique.
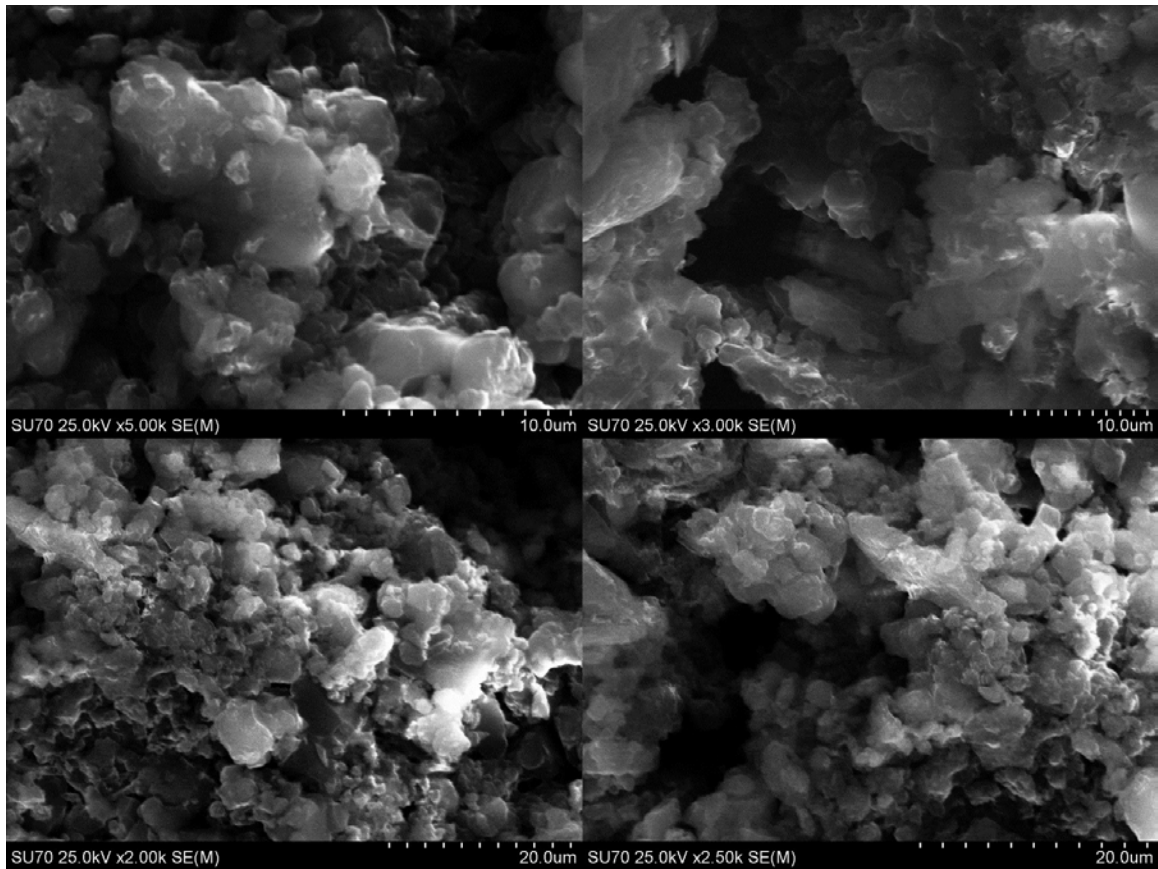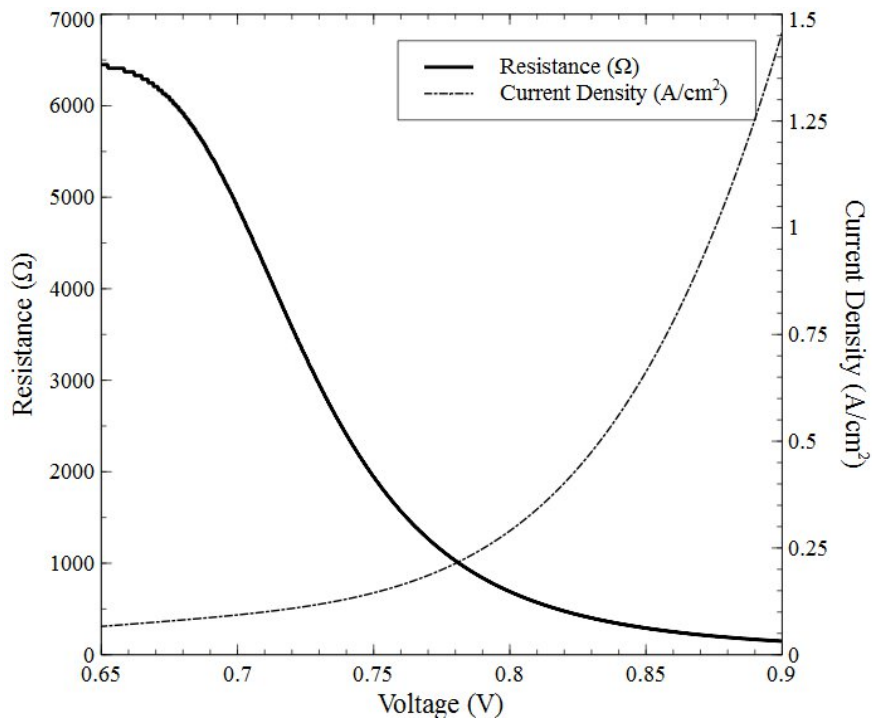

Figure 34 Resistance-voltage characteristics of a Ni-POA monolayers-(Au/Pd) tunnel junction grown by the Langmuir Blodgett technique.
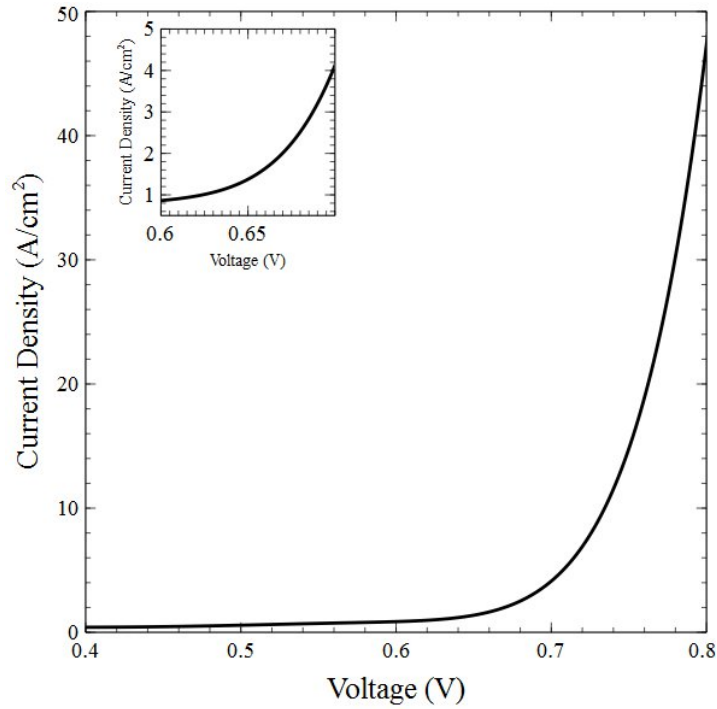
Figure 35 Current density-voltage characteristics of Ni-PMMA monolayers-(Au/Pd) tunnel junction developed by the Langmuir Blodgett technique.
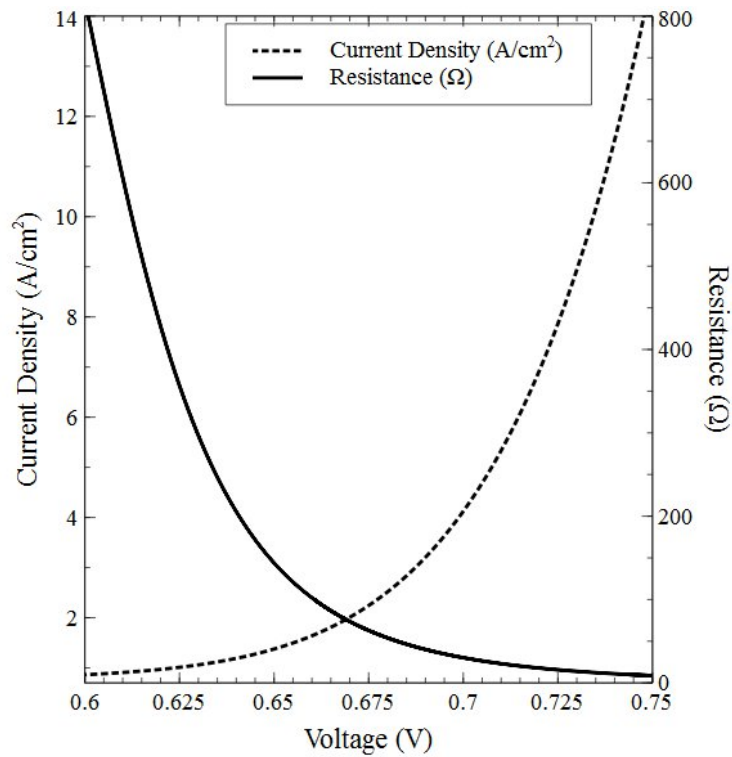
Figure 36 Resistance and current density vs. voltage characteristics of a Ni-PMMA monolayers-(Au/Pd) tunnel junction using Langmuir Blodgett technique.

49
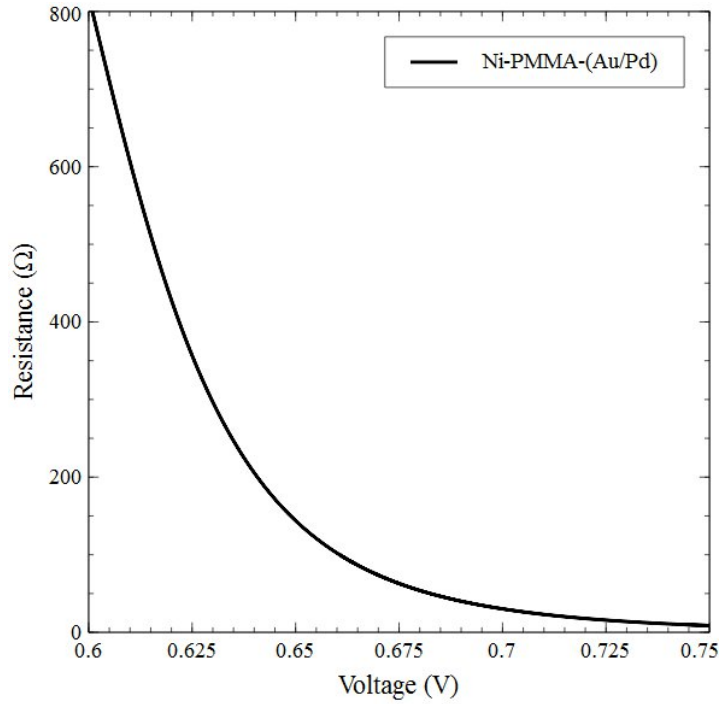
Figure 37 Resistance-voltage characteristics of Ni-PMMA monolayers-(Au/Pd) tunnel junction using Langmuir Blodgett technique.
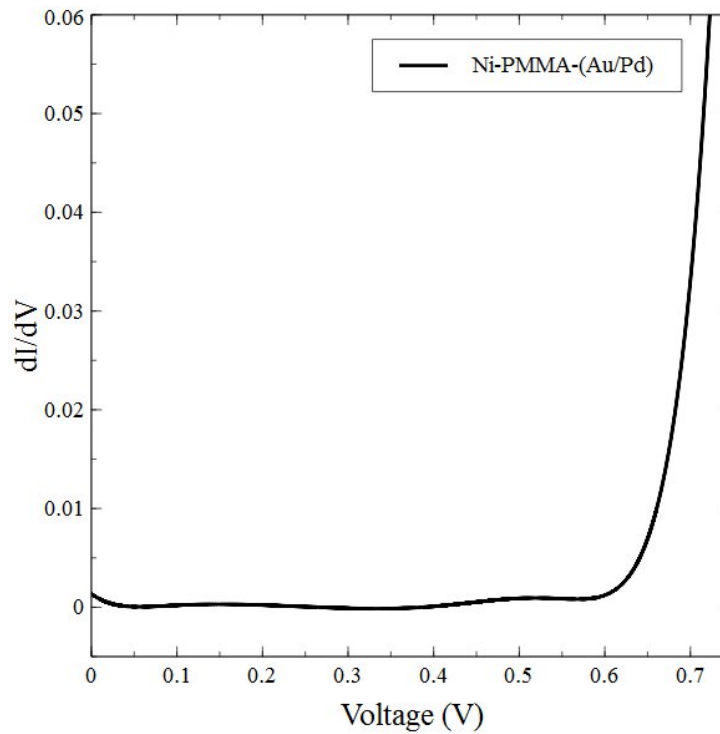
Figure 38 First derivative-voltage characteristics of Ni-PMMA monolayers-(Au/Pd) tunnel junction using Langmuir Blodgett technique.

50
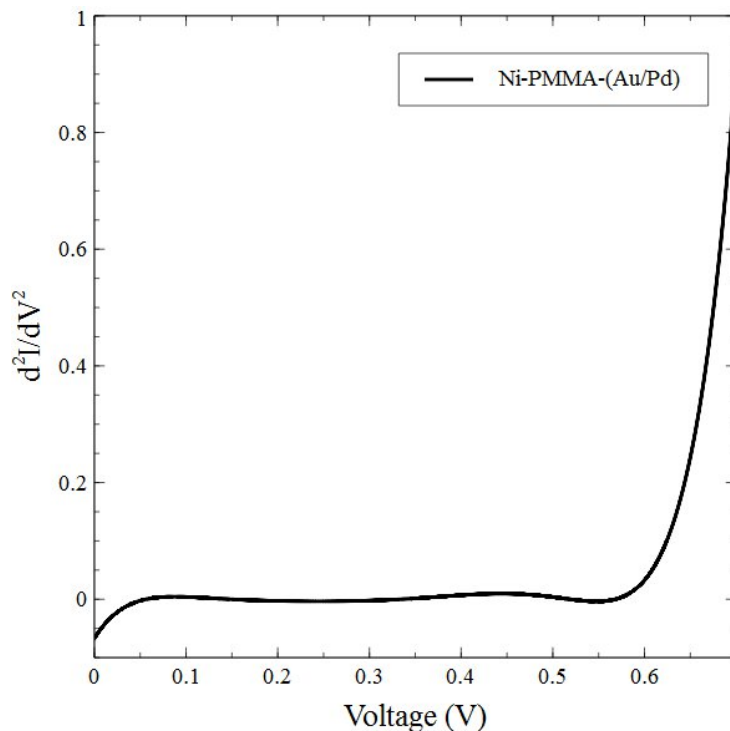
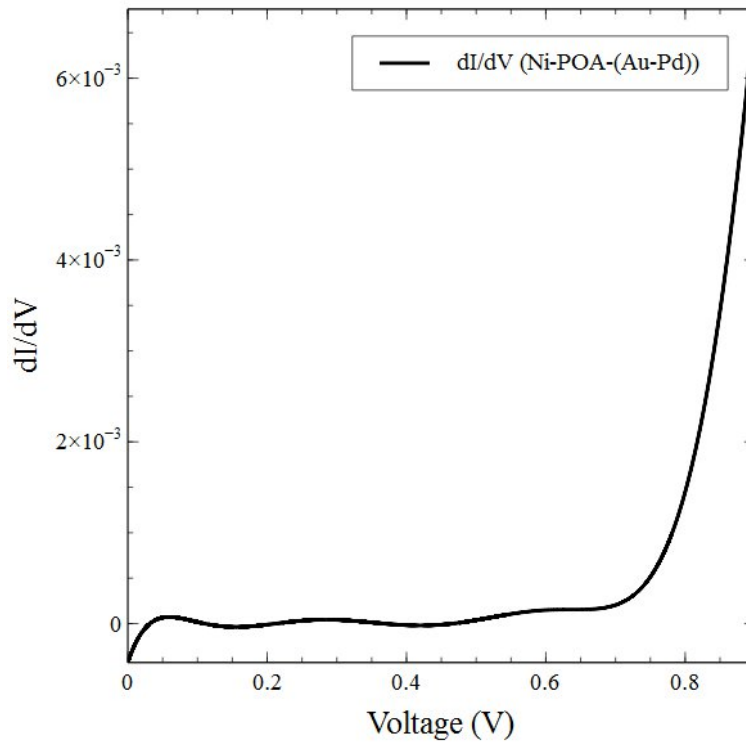Figure 39 Second derivative-voltage characteristics of Ni-PMMA monolayers-(Au/Pd) tunnel junction using Langmuir Blodgett technique.
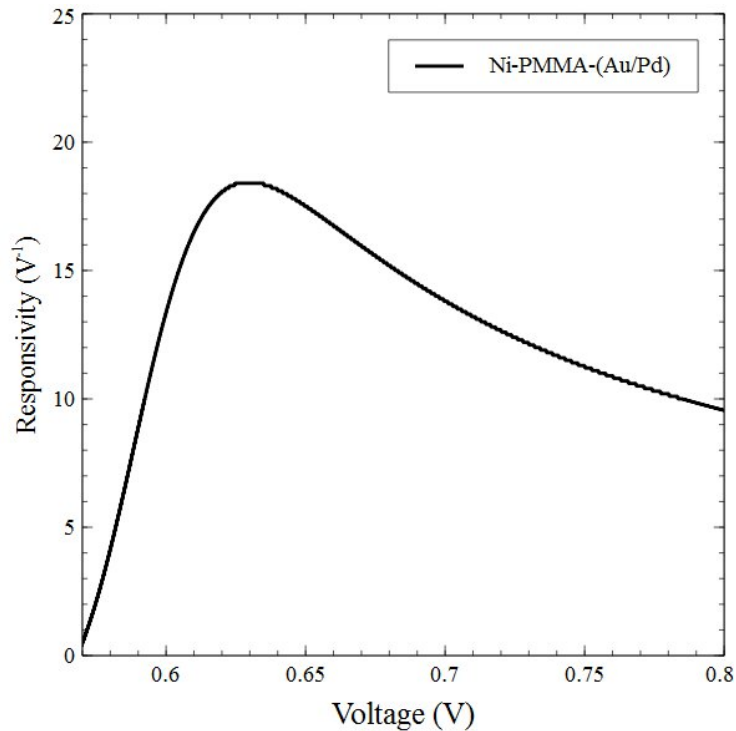
Figure 40 Responsivity-voltage characteristics of Ni-PMMA monolayers-(Au/Pd) tunnel junction using Langmuir Blodgett technique.

51

Table 3 State-of-the-art MIM diode Rectification Ratios (RR).

Assembly	η	Ref.
Au-**LB film** of 1-(10-acetylsulfanyldecyl)-4-{2-(4-dimethylaminonaphthalen-1-yl)-vinyl}-quinolinium iodide-Au	1:150 at ±1V	[83]
Ag–SAM of $SC_{14}CH_3Ga_2O_3$/GaIn Eutectic	1:100 at ±1V	[84]
Ag/Au-ferrocene(11-(ferrocenyl)-1-undecanethiol-Ag/Au	1:130 at ±1V	[44]
Au-Amino Thiol SAM-Au	1:55 at ±1 V	[85]
Au-SAM of Porphyrin/fullerene dyads/Au	1:12 at 2V	[86]
Au-SAM of $S-(CH_2)_3$ -Au	1:12 at ±1 V	[87]
Au-**LB film** of hexadecylquinolinium tricyanoquinodimethanide-Au	1:27 at 2.2 V	[88]
Au-**LB film** of 4-[2-(4-dimethylaminophenyl)-vinyl]-pyridinium salt (SAM)-Au/PtIr	1:70 at ±1 V	[89]

Table 4 State-of-the-art MIM diode responsivity.

Assembly	Maximum Responsivity (V^{-1})	Ref.
Ni-NiO-Au	5.5	Hoofring et. al[90]
Ni-NiO-Ni	1.6	I.Wilke et al[91]
Ni-NiO-Ni	2.75	M. Abdel Rahman et al[92]
Ni-NiO-Pt	-13	Esfandiari[93]
Ni-NiO-Cr/Au	5	Krishnan et al[94]

Table 4 (Continued).

Polysilicon-SiO$_2$-polisilicon	-31	Choi et al [95]
Polysilicon-SiO2-Au	-14.5	Dagenais et al [21]
Al-AlOx-Pt	-2.3	Bean et al [96]
Ni-NiO-Cu	7.3	Zhang et al[97]
Al-Al2O3-Pt	0.03	Kinzel et al[29]
Graphene-Air-Graphene	0.24	Zhu et al[57]

CHAPTER 6:

RESULTS: NARROW BAND EMISSION AND FREQUENCY SELECTIVITY OF NANOSTRUCTURE PERIODIC ARRAYS

As mentioned in previous chapters, a frequency selective thermal emitter has been patterned with periodic nanostructures of subwavelength dimensions. Optical lithography and reactive ion etching techniques were utilized to create Ni-Si based grating structures. With successive process optimization using different lithographic recipes, an optimum feature development was attained for the aimed period of repetition of 10 microns and an appropriate grating fill factor. Figure 41 shows an FIB micrograph of a Ni-Si based grating structure. An AZ 4620 photoresist recipe was optimized with
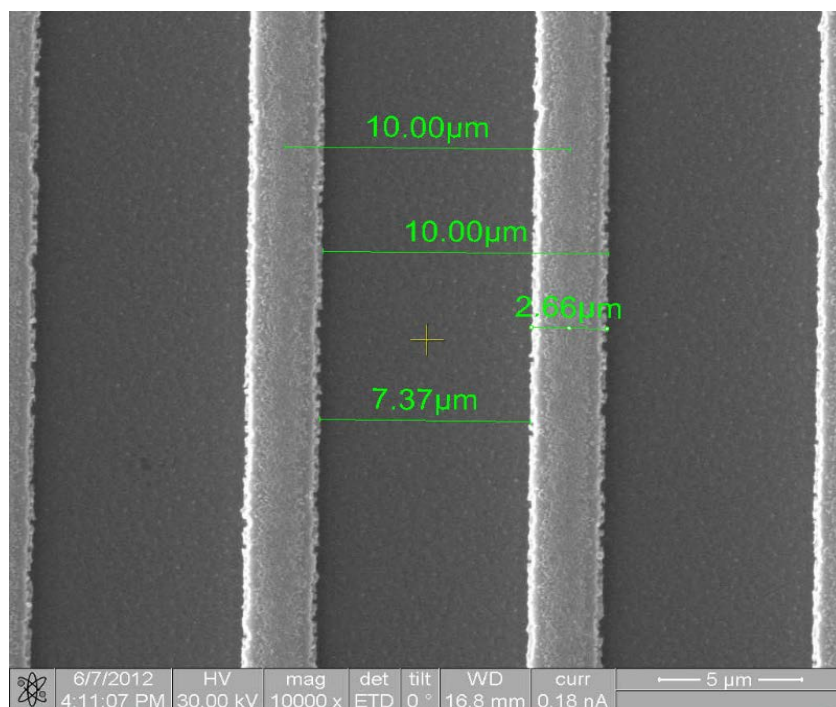
Figure 41 FIB micrograph of a nickel-silicon periodic grating structure for a thermal emitter application.

3000 rpm spin speed for a 7 micron thick layer of resist. It was followed by a 60 minute long soft bake and 3 hours of rehydration period. A Karl Suss Mask Aligner was used with an exposure energy of 350mJ/cm2 for 7 microns of AZ4620. The exposed photoresist was developed in an AZ400K-1:3 dilute mixture of developer and ionized water. 1 minute and 30 seconds of development time was found to be optimum for the desired feature size.

Figure 42 shows a schematic representation of the thermal emission measurements setup. The setup consists of a mounted heat source to heat the thermal emitter and a convex lens to focus the emitted radiation into a monochromator slit. A laser source and apertures were employed to ensure good alignment of the optics. A liquid nitrogen cooled HgCdTe detector was placed on the other end of the monochromator to proportionally detect thermal emission from the heated sample. The emissivity can be obtained by calculating the ratio of radiation emitted from the sample at a temperature T to the radiation emitted from a blackbody at the same temperature T.
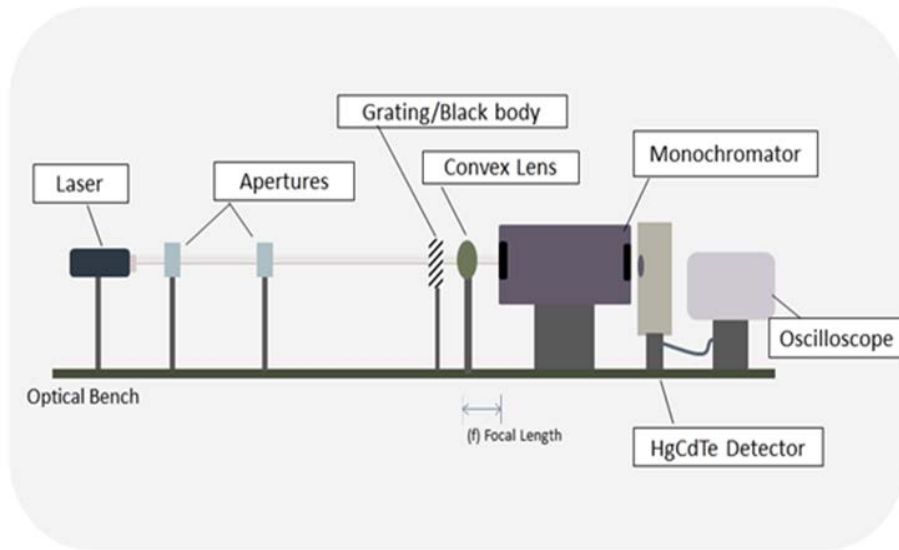
Figure 42 A schematic of the experimental setup for the measurement of the emission spectrum of the plasmonic emitter.

Even with careful fabrication optimization, the expected emission selectivity was not observed in the measurements. Using theoretical calculations it was later identified that the slightest variation in the

angle of inclination of the sample or the dimensions such as period of repetition, in the grating structure can lead to changes in thermal emission.

The thermal emission measurements for the grating were compared to simulated results to check the validity of the boundary conditions and solver parameters as shown in Figure 44.

A periodic disk structure was also modeled in the form of a 600nm diameter silver disk array on Quartz, as shown in Figure 43. These theoretical experiments have been used to investigate how the variation in the dimensional parameters of the periodic structures in a photonic crystal affects the tunability of emission.
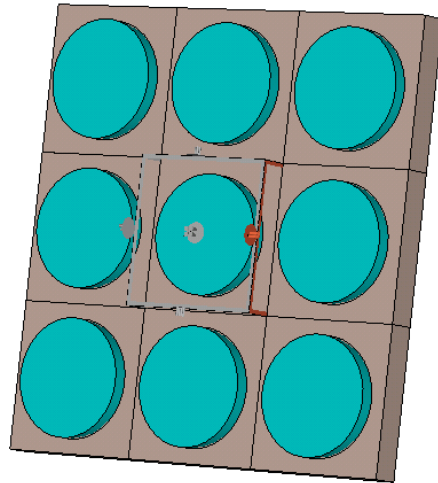
Figure 43 CST model with a sub wavelength periodic circular disk array.

Figure 43 also shows the CST model for a periodic disk array. As a base case, such a disk array was modeled for a period of repetition, p=3000nm, Ag nano disks with a diameter d=600nm, Au thickness m=40nm and underlying quartz thickness t=760nm. The emittance for this periodic disk array structure resulted in a narrow band peak with an emittance of 0.92 around ~185THz, as can be seen in Figure 45.

As shown in Figure 46, increasing the thickness of the underlying Quartz, shifts the peak to lower frequencies. Figure 47 shows how the frequency selectivity is greatly affected by the thickness of the

56

circular silver disk nanostructures. A sharp narrowband of emission was observed for a metal thickness of 760 nm. Varying this thickness by as little as ± 30nm, significantly reduces the frequency selectivity of emission from the photonic crystal. That is, for t_m corresponding to resonance there is perfect coupling between adjacent modes which can be seen with the enhanced emission peak. For changes in t_m or $t_m \pm \Delta$ there can be mixed modes due to the lack of perfect symmetry in coupling. Figure 48 shows the effect of change in the period of repetition of the silver disk array on the top of the quartz substrate. Increasing the period of repetition in such a nano disk array shifts the peak position to lower frequencies.

Thermal Emission from Ni-Si Grating
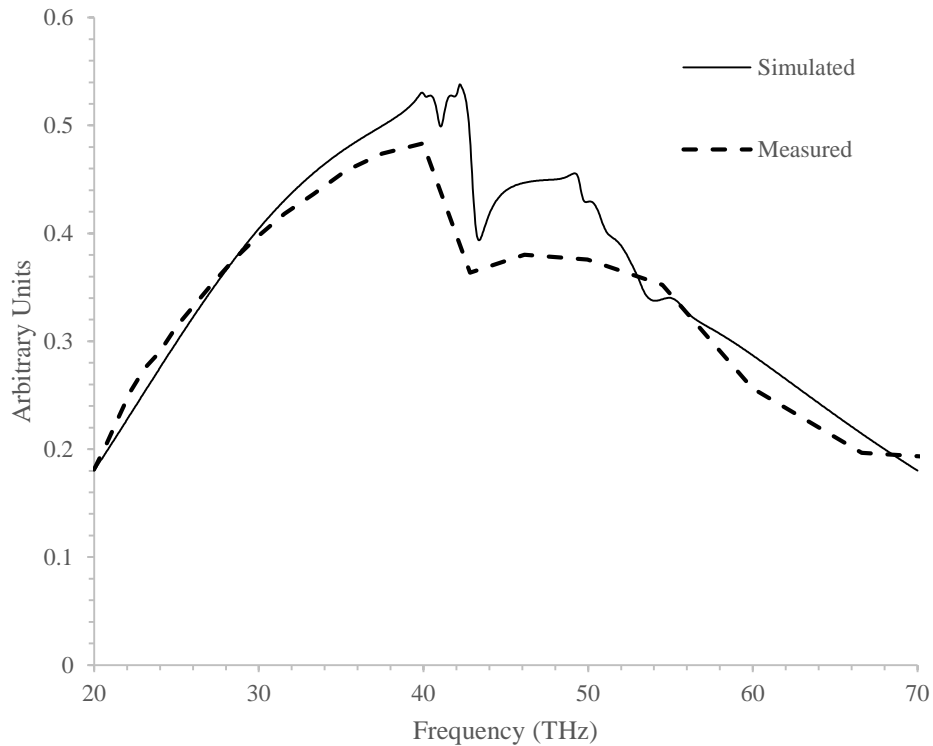
Figure 44 Comparison of simulated thermal emission results with measured data for a Si-Ni grating structure.
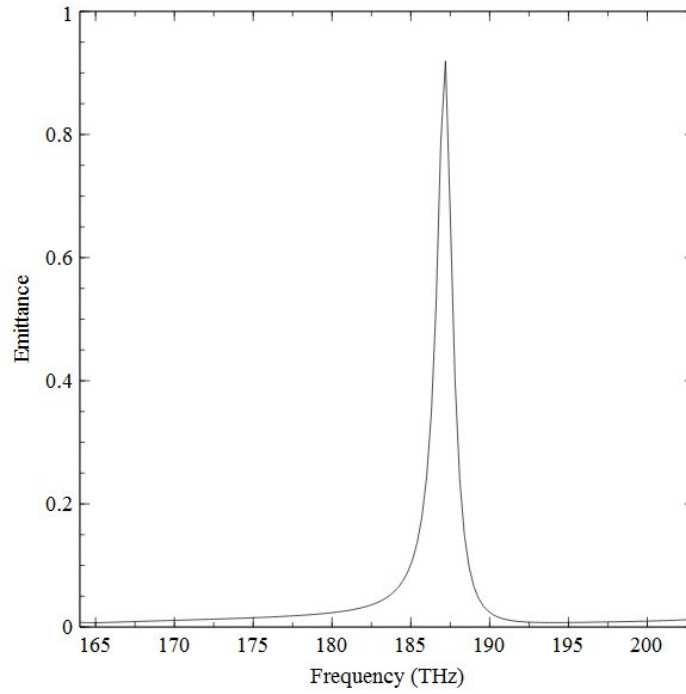
Figure 45 Frequency selective emission in a 600nm diameter circular disk structure in a quartz-silver photonic crystal.
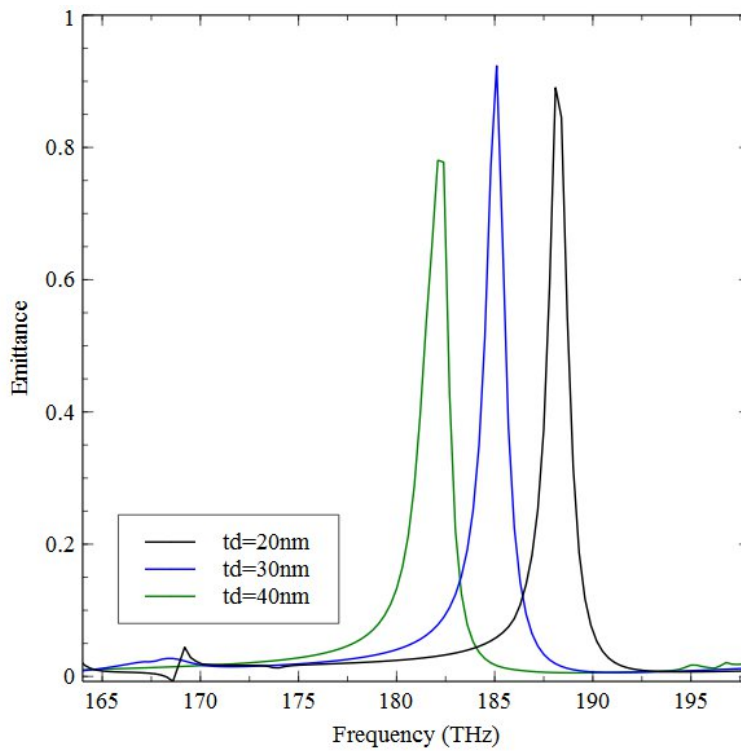
Figure 46 Effect of varying dielectric thickness in a quartz-silver based circular disk array.

58
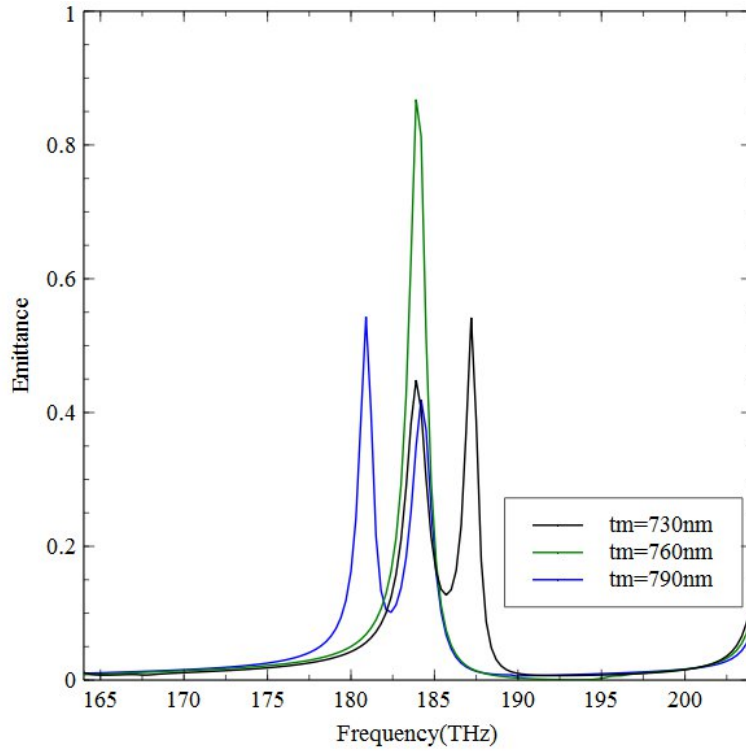
Figure 47 Effect of varying metal thickness in a quartz-silver based circular disk array.
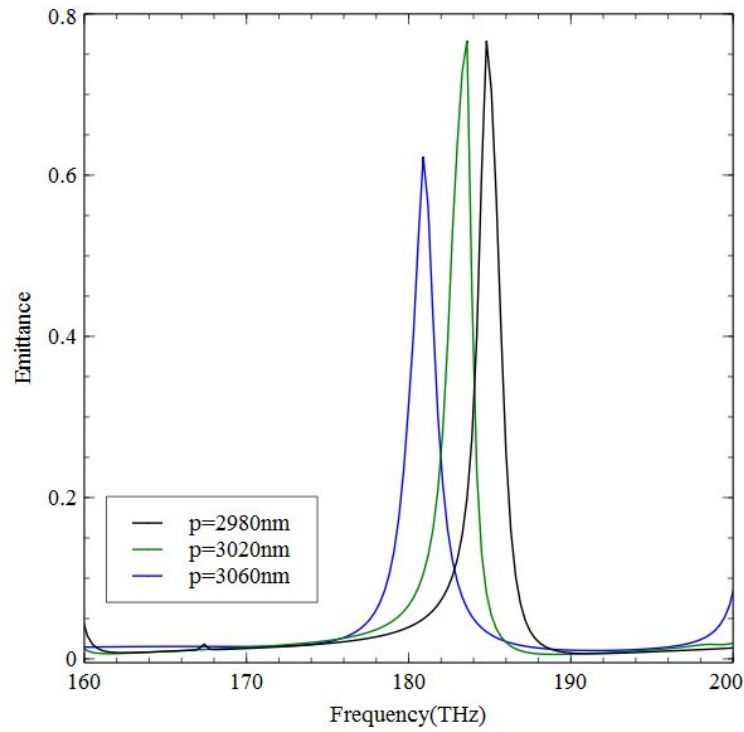
Figure 48 Effect of varying period of repetition in a quartz-silver based circular disk array.

6.1 Nanohole Arrays And Nanodisk Arrays For Frequency Selectivity

The use of diffraction gratings to observe the phenomenon of surface plasmon resonance was first described by Wood in 1902 [98]. Later, Lord Rayleigh, Otto and Kretschemann further developed the physical interpretation of the optical excitation of surface plasmons and the different techniques to achieve the same [99]–[101]. Surface plasmon resonance is an oscillation of charge-density at the interface between two media such as a metal and dielectric that possess dielectric constants of opposite signs. The surface wave resulting from an oscillating charge density can be associated with an electromagnetic wave. The field vectors of this electromagnetic wave decay reach their maxima at the interface while they show an evanescent decay deeper into the media. This surface plasma wave is of TM-polarization.

Fabry Perot resonators are often used to concentrate light within a subwavelength cavity. Such a cavity facilitates the enhancement of weak optical processes such as spontaneous emission. Accessing optical length scales well below the diffraction limit allows significant enhancement of weak physical processes [102]–[108]. Optical cavities allow efficient concentration and storage of electromagnetic energy and are consequently used throughout optics for numerous light emission and detection applications.

To analyze the emission enhancement of this system, dimensional and material variations were analyzed for a Ag-Quartz based disk array and hole array structures in the form of Fabry-Pérot cavities. Localized surface plasmon resonance is responsible for enhancement of emission peaks in the case of metal-dielectric periodic disk arrays. It is basically due to the collective motion of conduction electrons that are induced as a result of electromagnetic field interactions. When an electromagnetic wave in the suitable wavelength range is incident on a nanodisk array, it leads to the emergence of localized dipoles in each disk or nanoparticle. As the electrons, or said dipoles oscillate with a change in the

60

electromagnetic field, a strong surface plasmon peak is observed at a specific wavelength. In this way localized surface plasmon resonance can cause the enhancement of electric fields near the surface of the nanoparticles. Such resonance can also lead to extraordinary optical absorption, emission and scattering.

Localized surface plasmons are non-propagating excitations of the conduction electrons of metallic nanostructures coupled to the electromagnetic field [109]. Surface plasmon polaritons (SPPs) are propagating dispersive electromagnetic waves coupled to the electron plasma of a conductor at a dielectric interface. Surface plasmon polaritons are electromagnetic modes constituted by a light field coupled to a collective electron oscillation propagating along an interface between a metal and a dielectric. SPPs are electromagnetic modes constituted by a light field coupled to a collective electron oscillation propagating along an interface between a metal and a dielectric. As SPPs are surface waves, their field intensity is maximum in the interface and decays exponentially along a directions perpendicular to it.

Nanohole and nano-disk arrays were analyzed in terms of peak wavelength, bandwidth of the peak and the peak amplitude to understand their relationship with the frequency selectivity. Figure 49 provides a graphical presentation of the parameters that were analyzed to compare the selectivity of emission obtained using periodic arrays of nanostructures. The spectral bandwidth was obtained as the full width at half maximum (FWHM) or the full width taken where the amplitude is half of the peak value. Figure 50 and Figure 57 show the emission spectrum with and without a backside reflecting mirror for nano disk and nano hole array structures, respectively. The backside mirror is used to introduce a fabry-perot cavity type resonance for sharp and more selective emission spectra. Such a cavity structure is composed of a dielectric layer with a thin metal film (mirror) on one side and a periodic array structure of Au or Ag on the other side.

61
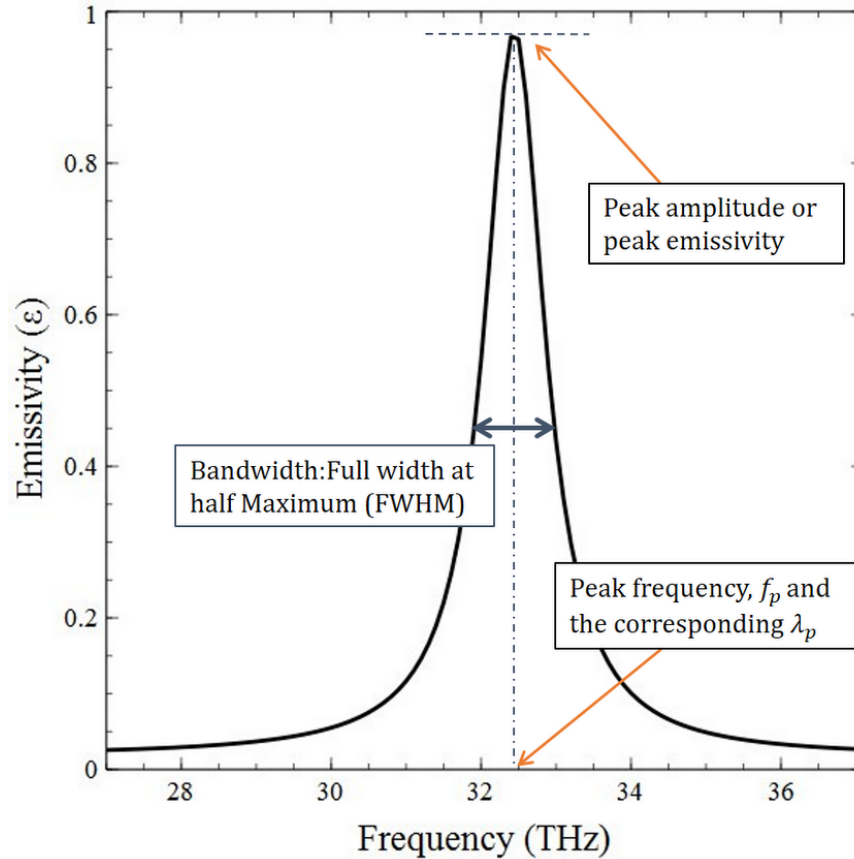
Figure 49 Analysis of selective emissivity for periodic disk and hole arrays, based on bandwidth of the peak, peak wavelength and peak amplitude.

6.2 Impact Of Dimensional Variations On The Frequency Selectivity Of IR Emission

Figure 51 shows the effect of disk thickness on the emission spectrum. On increasing the metal thickness, the emission peak shifts to lower frequencies. The peak amplitude also varies corresponding to any change in the metal thickness. Figure 52 shows the effect of the disk diameter on the emission spectrum. There is a reduction in the peak amplitude for smaller disk diameters. As the disk diameters become smaller, the peak shifts to higher frequencies. Quartz thickness modifications in this LSPR based disk array structure can allow the tuneability of the peak wavelength while maintaining the same spectral bandwidth and peak amplitude, as seen in Figure 54. Figure 56 shows the impact of the period of repetition on the frequency selective emission in the case of a periodic hole array structure. It is observed that with increasing the period of repetition, the peaks shift to higher frequencies without a

significant change in the amplitude of emissivity. Whereas in the case of a periodic disk array structure, increase in the period of repetition shifts the peak to higher frequencies while showing a reduction in the value of peak emissivity, as it can be seen in Figure 53.

Figure 60 shows the impact of variation of metal thickness on the emission spectrum in a Ag-Quartz periodic hole array structure. The metal thickness or the hole depth is seen to significantly impact the peak bandwidth. Figure 58 presents the impact of hole diameter on the selectivity of emission. Both, the peak amplitude and the bandwidth vary with a change in the hole diameter in a periodic hole array structure. Figure 59 shows the impact of Quartz thickness on the selectivity of emission. The Quartz thickness can be used to change the wavelength corresponding to the emission peak without affecting the peak amplitude or bandwidth.
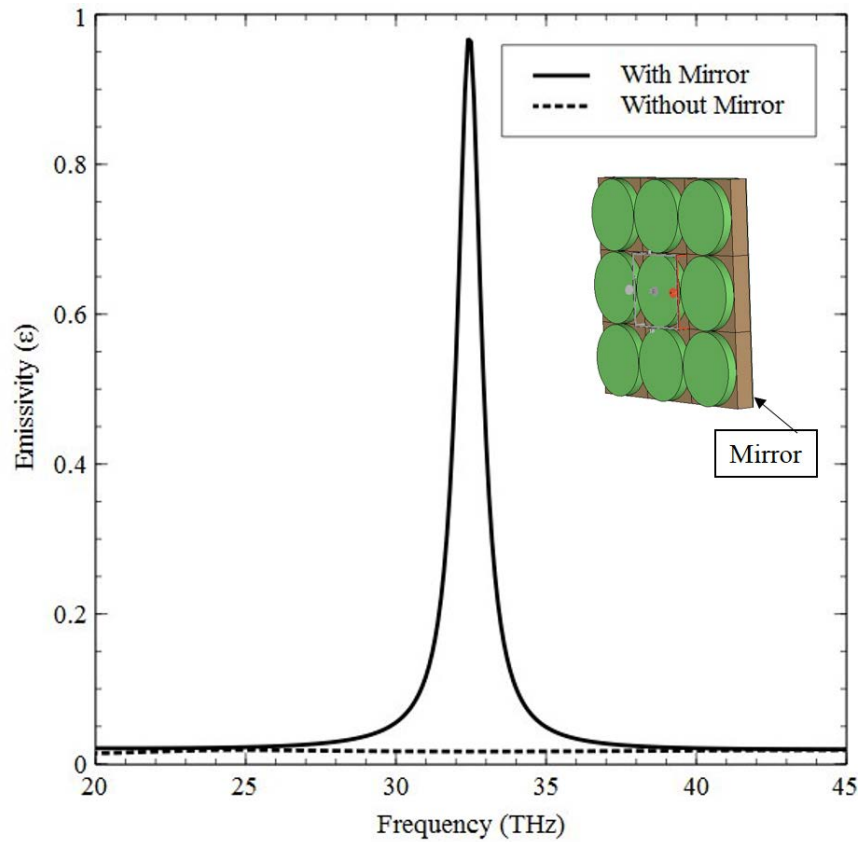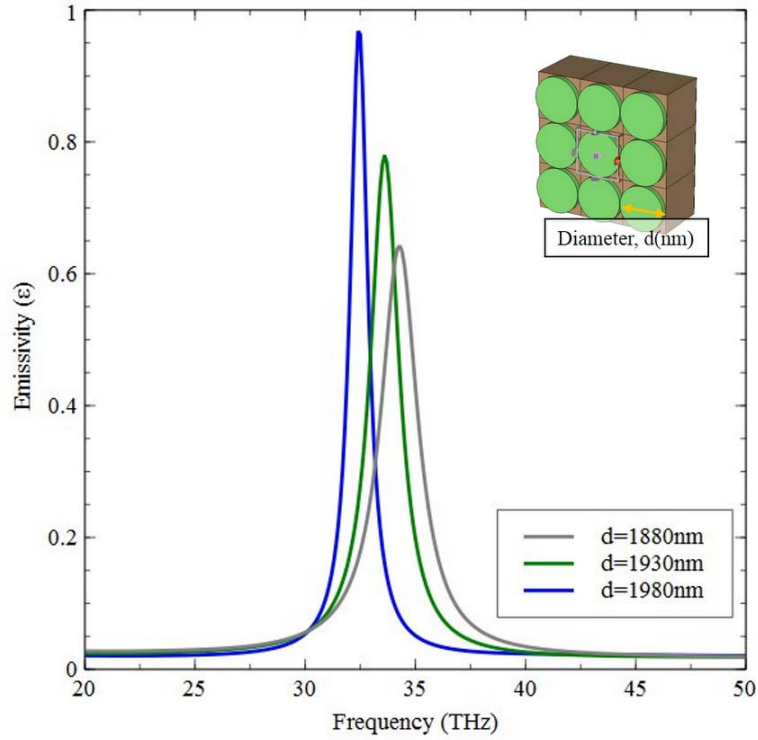

Figure 50 Disk array with and without a backside reflecting mirror to create a Fabry-Pérot cavity.

X

Figure 51 Effect of varying disk diameter on the frequency selectivity in a periodic disk array structure.

Figure 52 Effect of varying disk thickness on the frequency selectivity in a periodic disk array structure.

64

As reported in literature, the impact of period of repetition on the peak wavelength can be approximately given by[56], [110]:

$$\lambda_{max} = \frac{a}{\sqrt{i^2 + j^2}} \cdot \sqrt{\frac{\epsilon_1 \epsilon_2}{\epsilon_1 + \epsilon_2}}$$

where a is the period of repetition and i and j are the diffraction orders in the x and y directions of the periodic array. However this relationship only holds in the case of periodic hole arrays with diameter, $d \sim a/2$. In order to support this assumption, the change in the peak position was observed for two cases. Case 1: where $d \sim a/2$ as shown in Figure 55 and Case 2: where $d \sim a$ as shown in Figure 56. As it can be clearly seen, Case 1 shows a shift in the peak position to higher wavelengths on an increase in the period of repetition as expected whereas Case 2 shows a shift in the peak position to longer wavelengths on increase in the period of repetition.

Figure 53 Effect of varying period of repetition on the frequency selectivity in a periodic disk array structure.

65

Figure 54 Effect of varying quartz thickness on the frequency selectivity in a periodic disk array structure.

Figure 55 Effect of varying period of repetition on frequency selectivity in Au-quartz hole array structure for diameter d, where d~a/2.
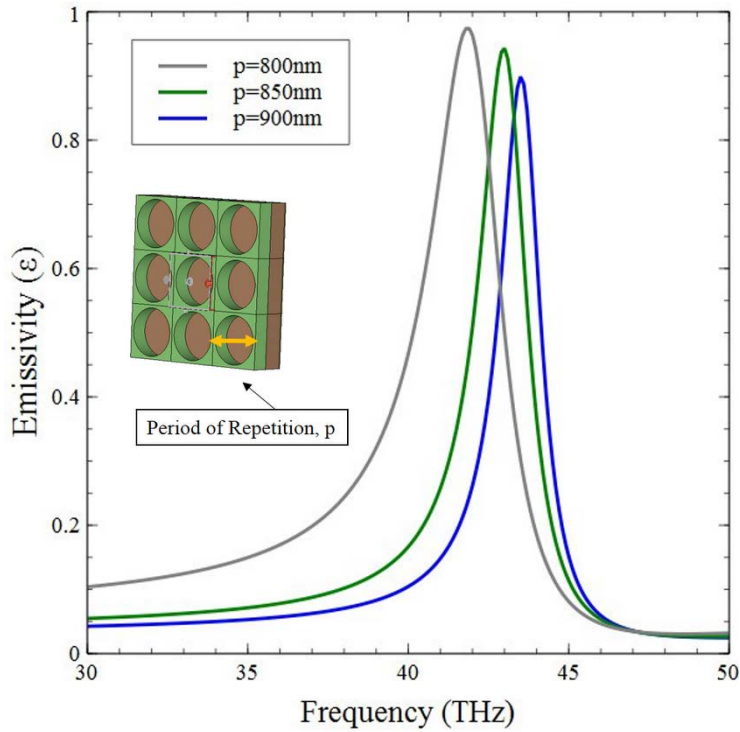
Figure 56 Effect of varying period of repetition on frequency selectivity in Au-quartz hole array structure where d~a.
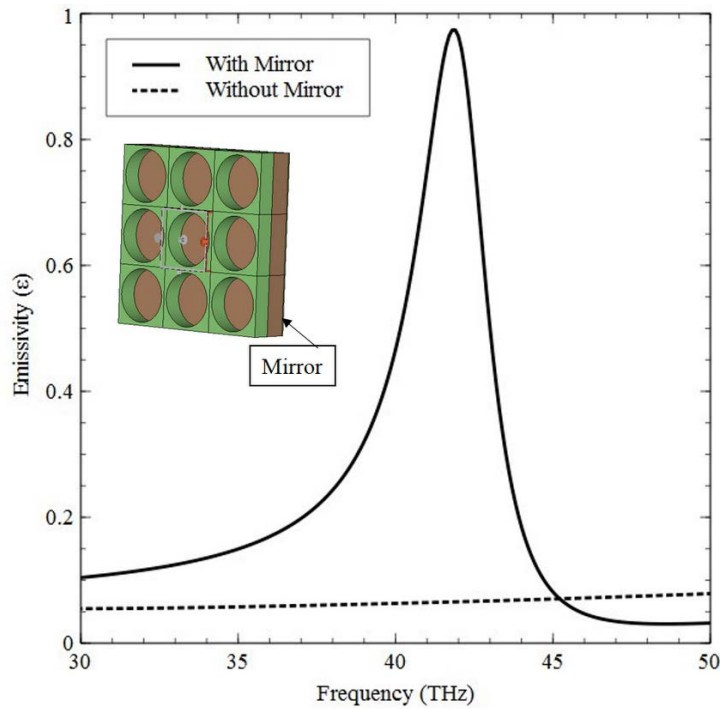
Figure 57 Hole array with and without a backside reflecting mirror to create a Fabry-Pérot cavity.

67
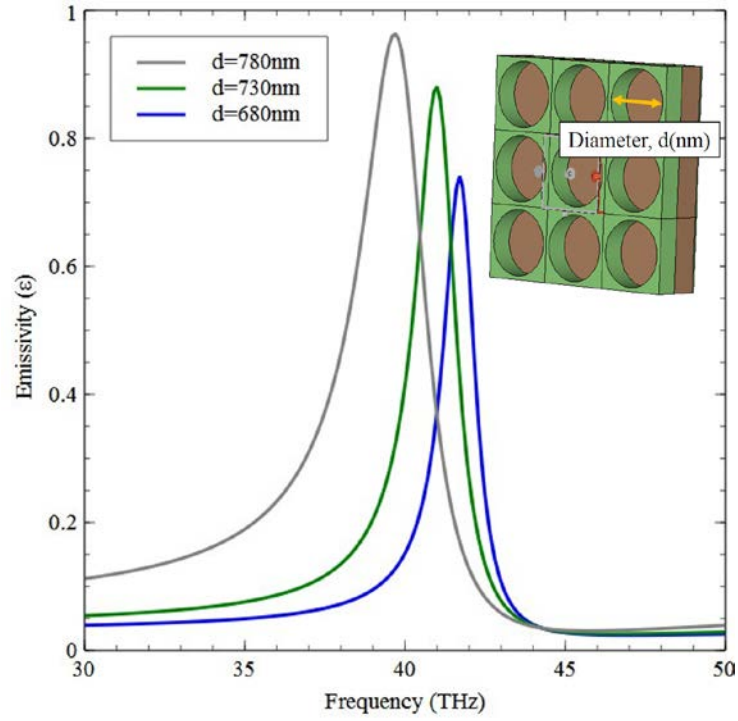
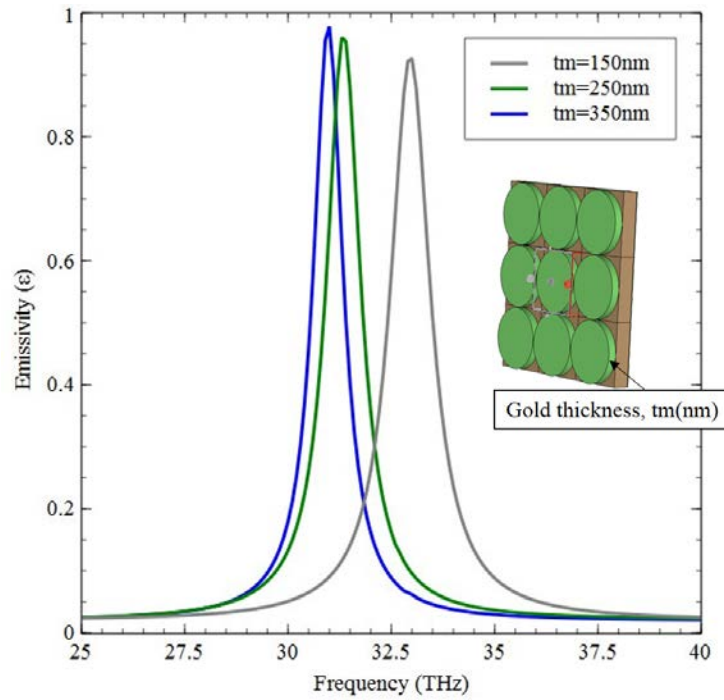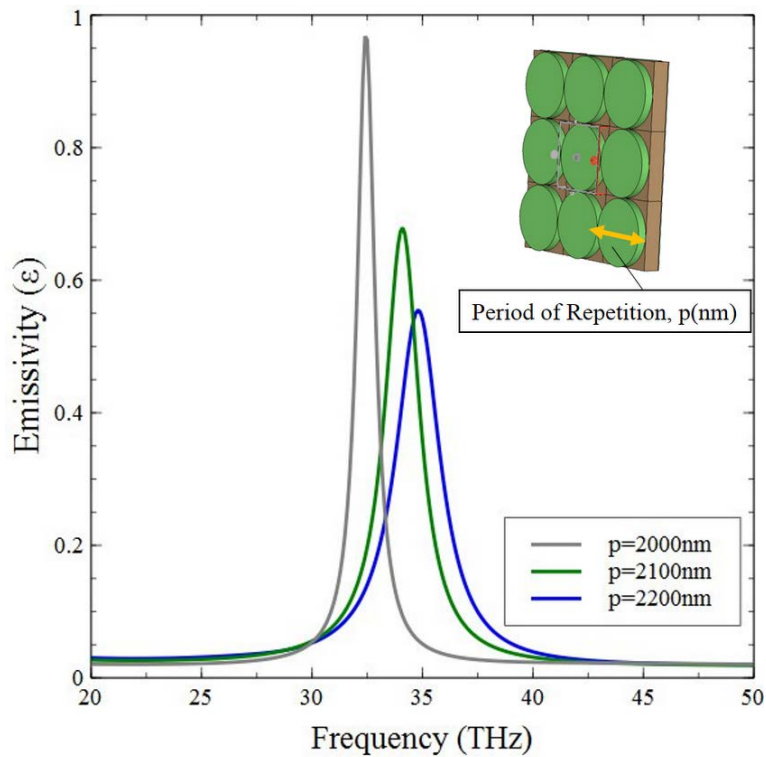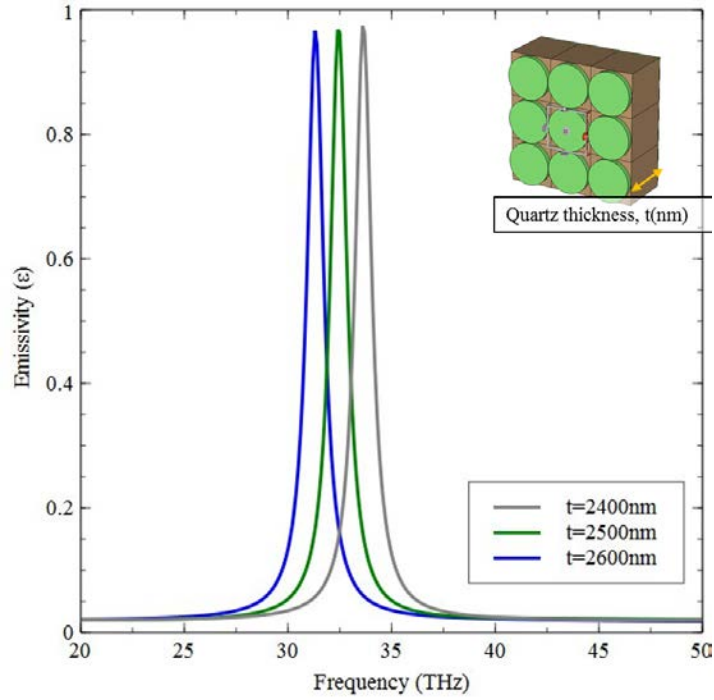Figure 58 Effect of varying hole diameter on frequency selectivity in a periodic hole array structure.
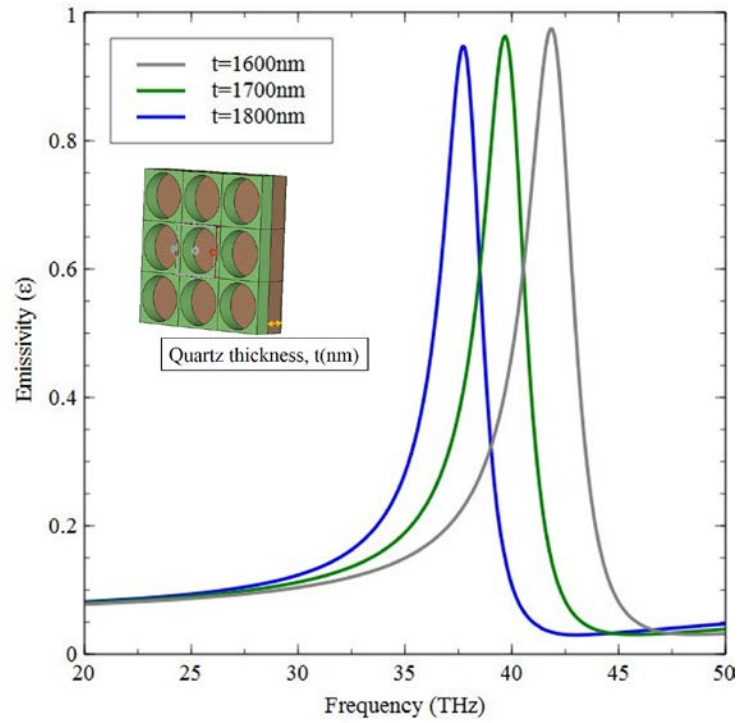
Figure 59 Effect of varying quartz thickness on the frequency selectivity in a periodic hole array structure.
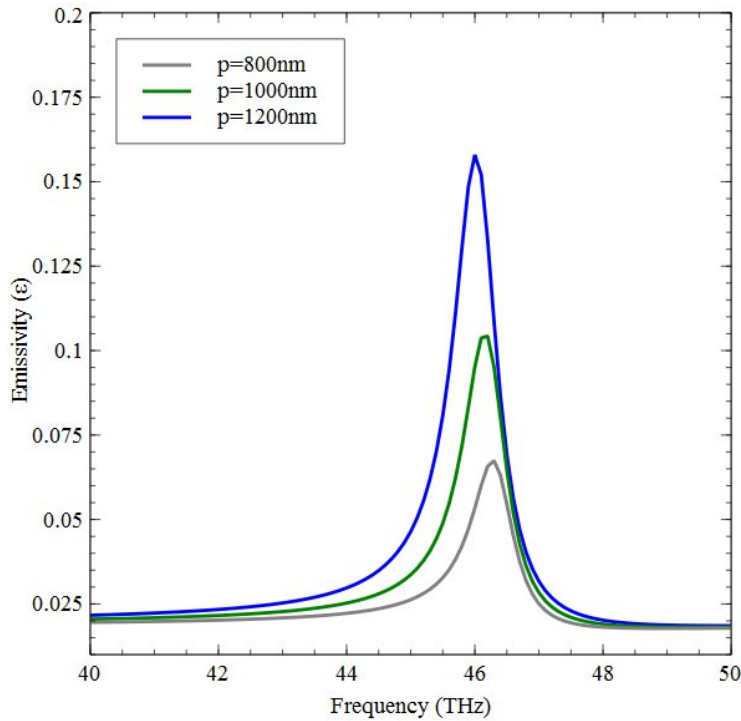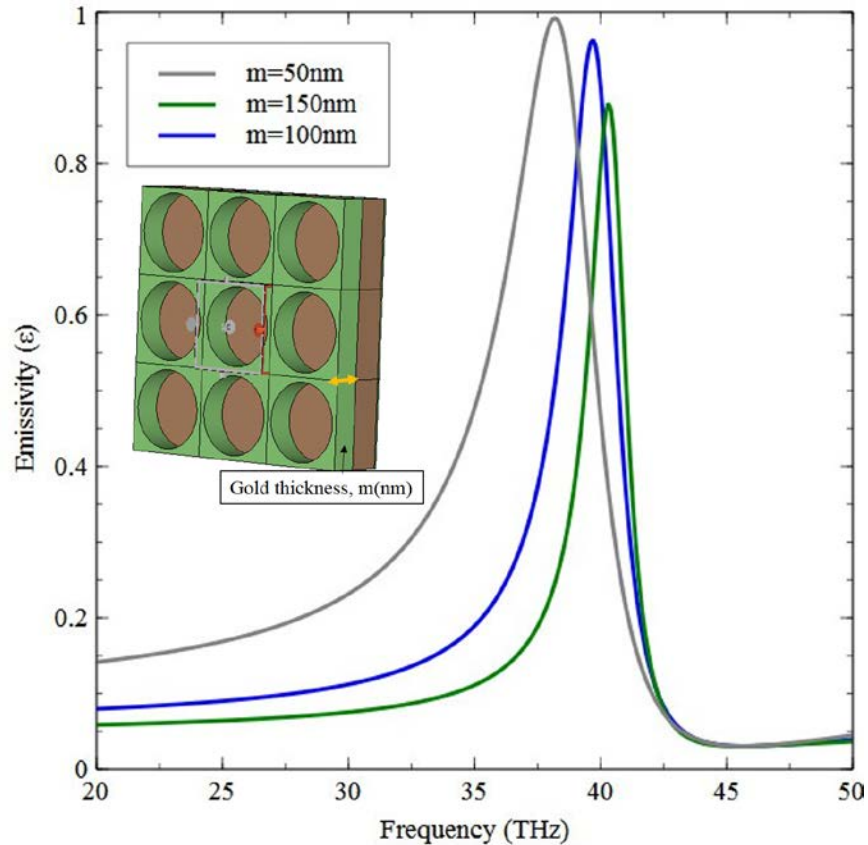
Figure 60 Effect of varying Au film thickness on the frequency selectivity in a periodic hole array structure.

6.3 Impact Of Dimensional Variations On The Bandwidth Of Narrow Band Emission

Figure 62 shows the impact of disk diameter on the bandwidth of narrowband emission. It is observed that an increase in the disk diameter causes the peak to become sharper. In other words the bandwidth of the emission peak is reduced by increasing the disk diameter. Unlike the disc diameter, variations in the Quartz thickness, in such a Au disk array, do not impact the bandwidth of narrowband emission, as shown in Figure 61. Figure 65 shows the impact of the metallic disk thickness on the peak bandwidth. For an increase in the Au film thickness, the bandwidth of the emission peak is reduced, however, beyond a certain saturation limit, any further increase in the Au film thickness does not affect the bandwidth of the emission peak. Figure 64 shows the impact of the hole diameter on the bandwidth of the narrow band emission. It is observed that the bandwidth increases with an increase

69

in the hole diameter. Figure 64 shows the effect of quartz thickness on the bandwidth of the narrowband emission. The bandwidth is found to decrease with increasing quartz thickness in periodic hole array structures. Figure 66 shows the effect of the Au film thickness on the bandwidth of the narrowband emission. The bandwidth is observed to decrease drastically with an increase in the gold film thickness. However, the bandwidth almost saturates with any further incremental increase in the Au film thickness after a certain limit. In this case, the bandwidth is observed to saturate around 200nm of Au film thickness, and any further increase in Au thickness does not affect the peak bandwidth of ~0.7 THz.
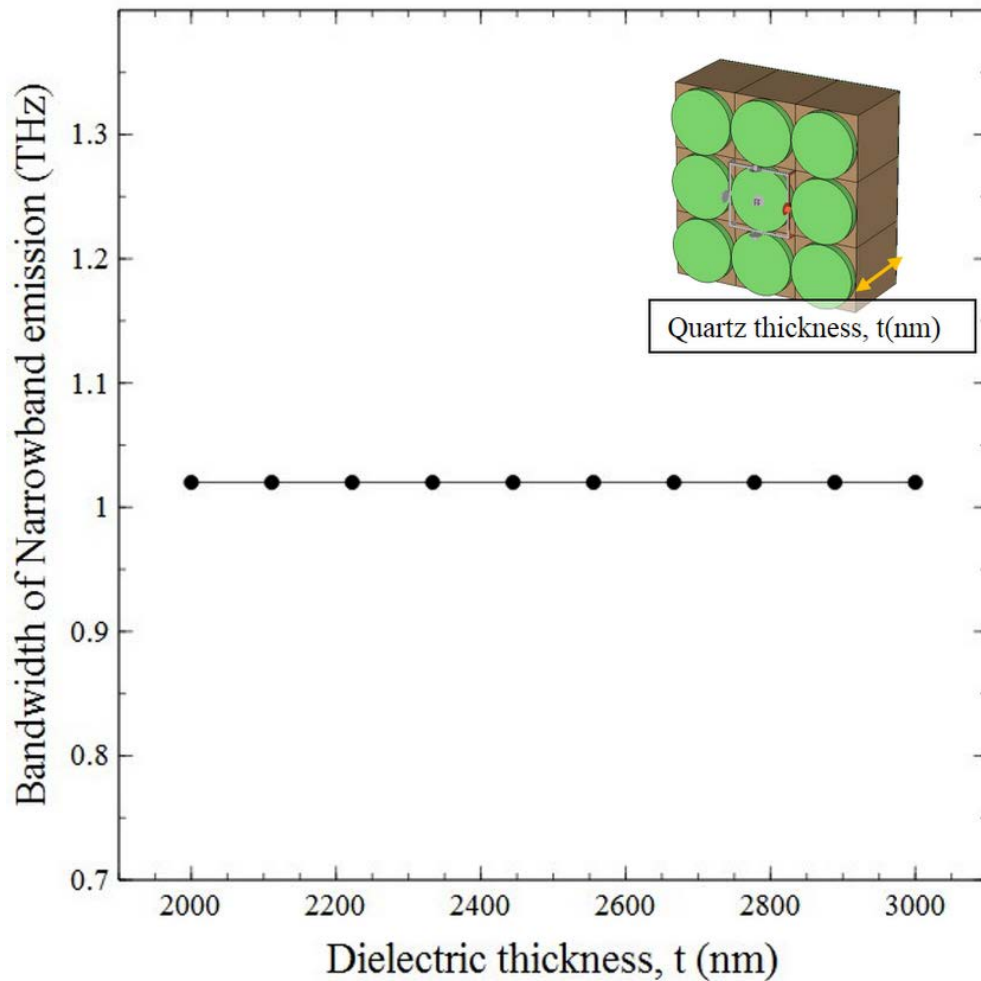
Figure 61 Effect of dielectric film thickness on the bandwidth of the narrowband emission for a periodic disk array structure.
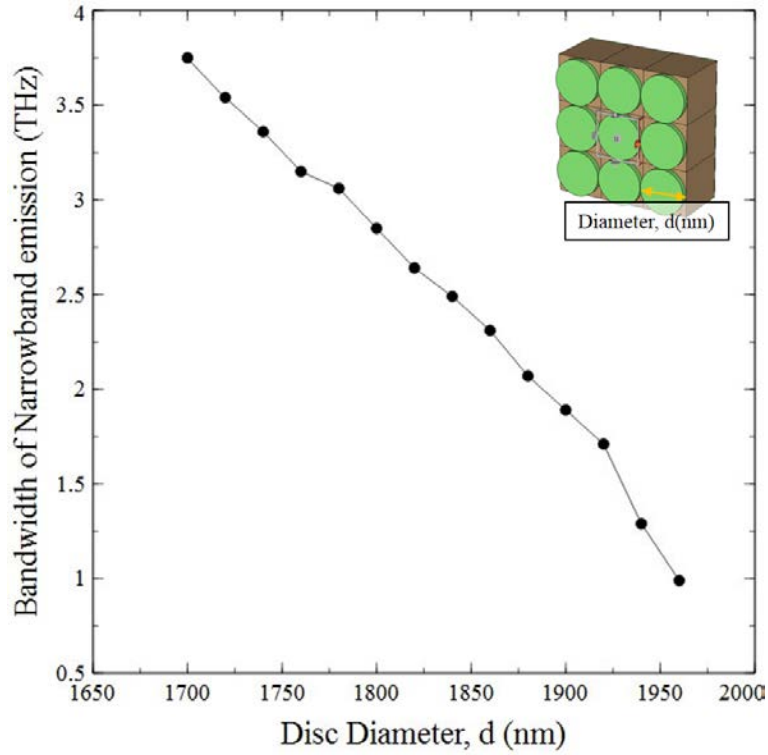
Figure 62 Effect of disk diameter on bandwidth of narrowband emission in a periodic disk array structure.
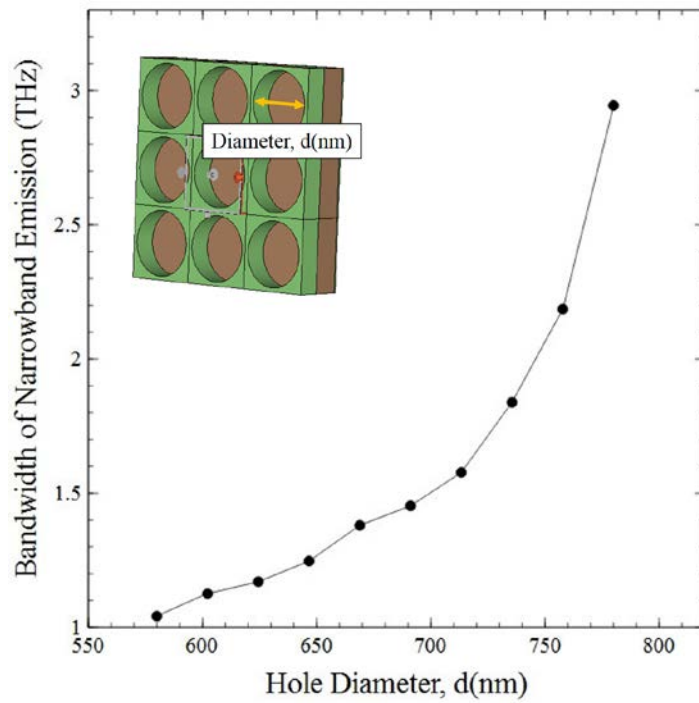
Figure 63. Effect of hole diameter on the bandwidth of the narrowband emission in a periodic hole array structure.

71
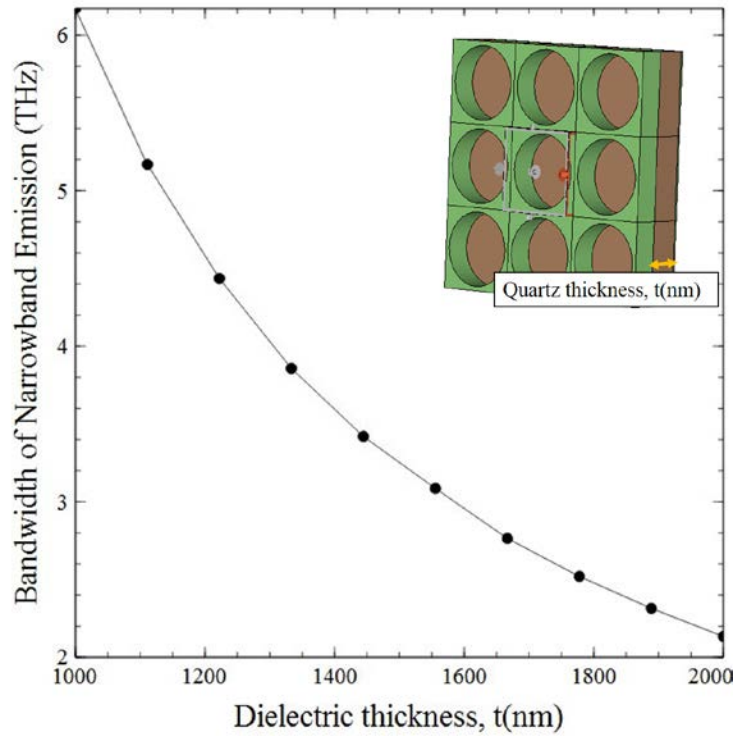
Figure 64 Effect of quartz thickness on the bandwidth of the narrowband emission in a periodic hole array structure.

Figure 65 Effect of metal/disk thickness on the bandwidth of the narrowband emission in a periodic disk array structure.

72
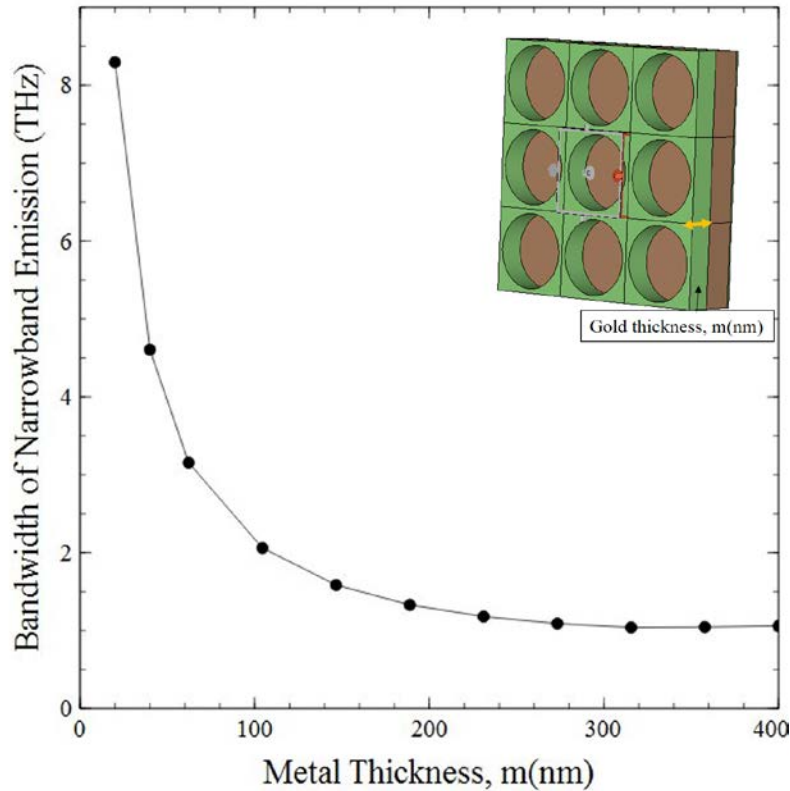
Figure 66 Effect of Au film thickness on the bandwidth of the narrowband emission in a hole array structure.

6.4 Impact Of Dimensional Variations On The Peak Emissivity Of The Narrow Band Emission

Figure 67 shows the impact of hole diameter on the amplitude of the emissivity peak. The peak amplitude is observed to increase with an increase in the hole diameter. For a hole diameter close to the period of repetition of this periodic array, the amplitude of the peak emissivity is ~1. Figure 69 shows the impact of metal film thickness in the case of periodic hole array nanostructures. It is observed that the peak emissivity is seen to decrease with an increase in metal film thickness, however, for thin, 20-30nm, metal films, i.e. Au, the peak emissivity is found to be as high as ~1. Figure 68 shows the impact of Quartz thickness on the peak emissivity in a the hole array structure. Increase in Quartz thickness is found to increase the peak emissivity up to a certain maximum, however, after this limit, any further increase in the Quartz thickness lowers the peak emissivity. Figure 71 shows the

73

impact of Au film thickness on the peak emissivity in the case of Au nano-disk arrays. The peak emissivity is found to increase to a maximum value as a result of thicker gold films, however, any further increase in the Au disk thickness lowers the peak emissivity. Figure 70 shows the impact of disk diameter on the peak emissivity of the narrowband emission. Increasing the disk diameter raises the amplitude of the peak emission attainable by the Au-Quartz disk array. Figure 72 represents the impact of dielectric thickness on the peak emissivity of a disk array structure. Just like in the case of hole array structures, Au-Quartz nano disk arrays with thicker dielectric films show an increase in the peak value of emissivity. However, after a certain value, the peak emissivity is lowered with any further increase in the dielectric thickness.
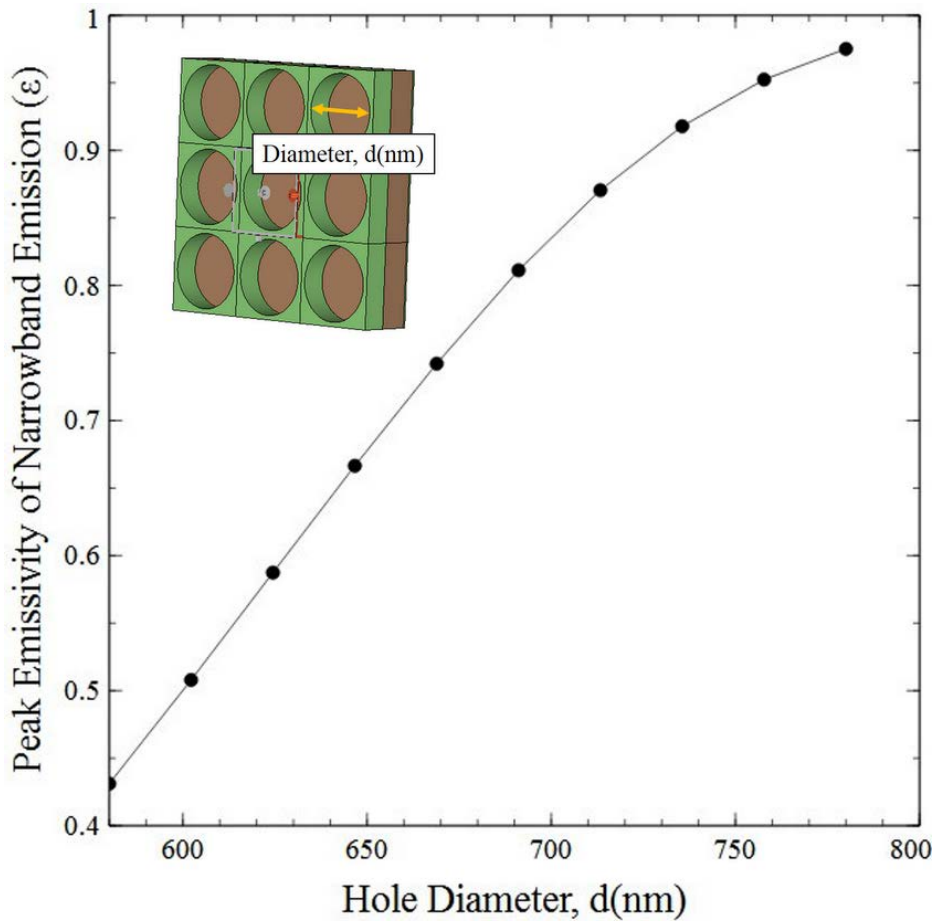
Figure 67 Effect of hole diameter thickness on peak emissivity for a periodic hole array structure.
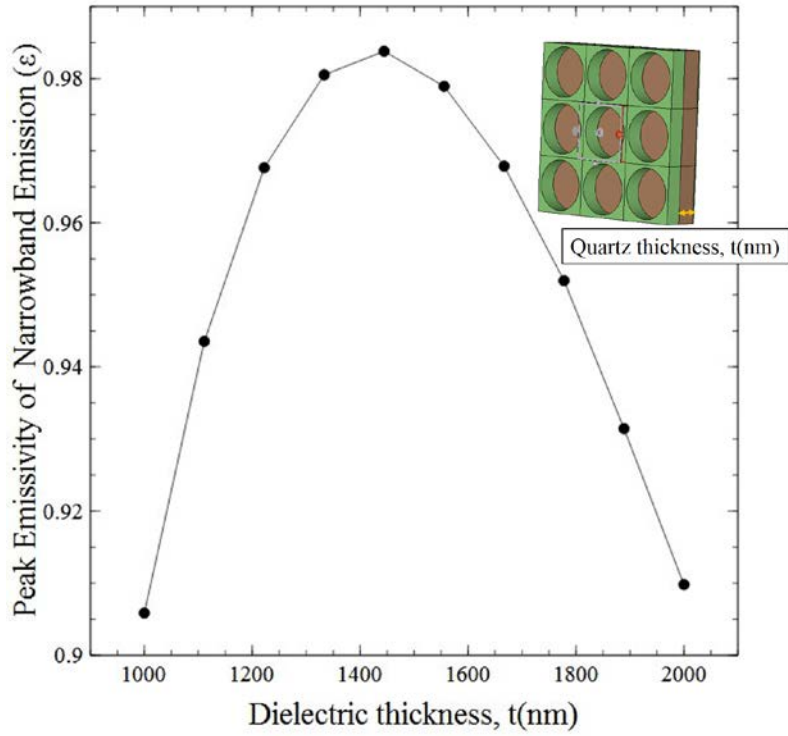
Figure 68 Effect of quartz thickness on peak emissivity in a periodic hole array structure.
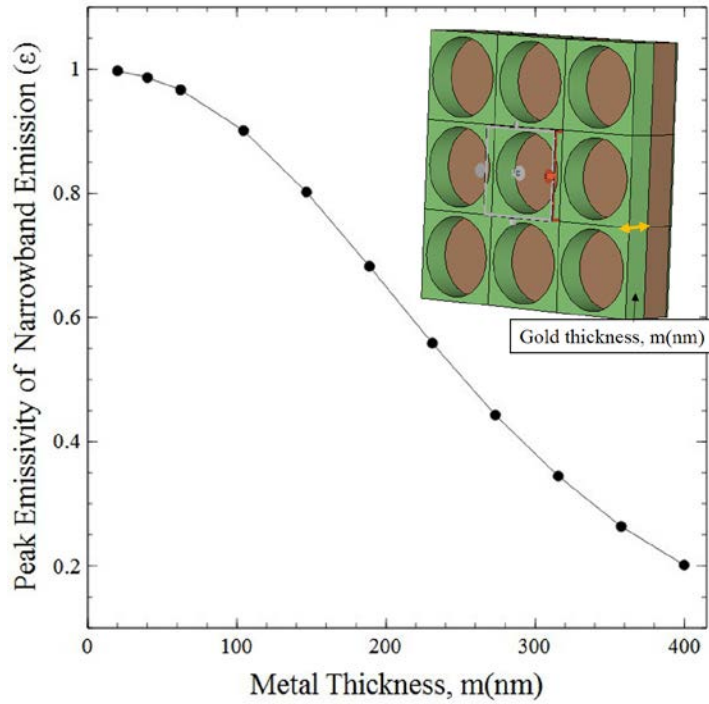
Figure 69 Effect of Au film thickness on peak emissivity for a Au-Quartz hole array structure.

75
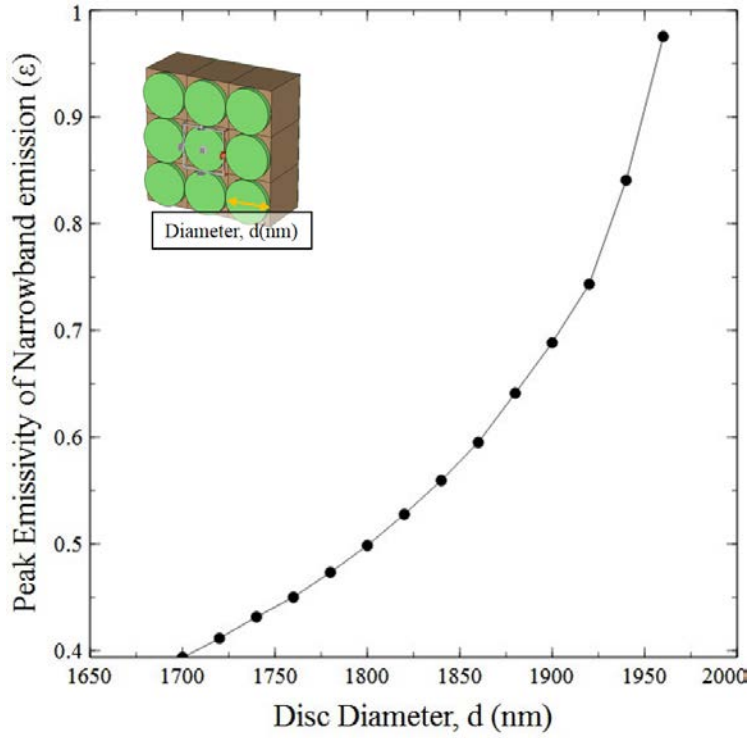
Figure 70 Effect of disk diameter on peak emissivity in narrowband emission in a periodic disk array structure.

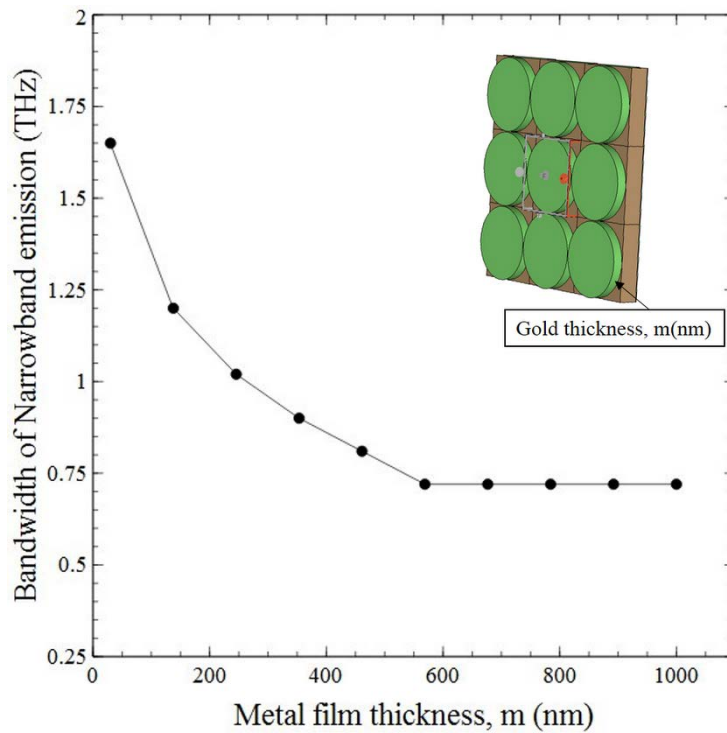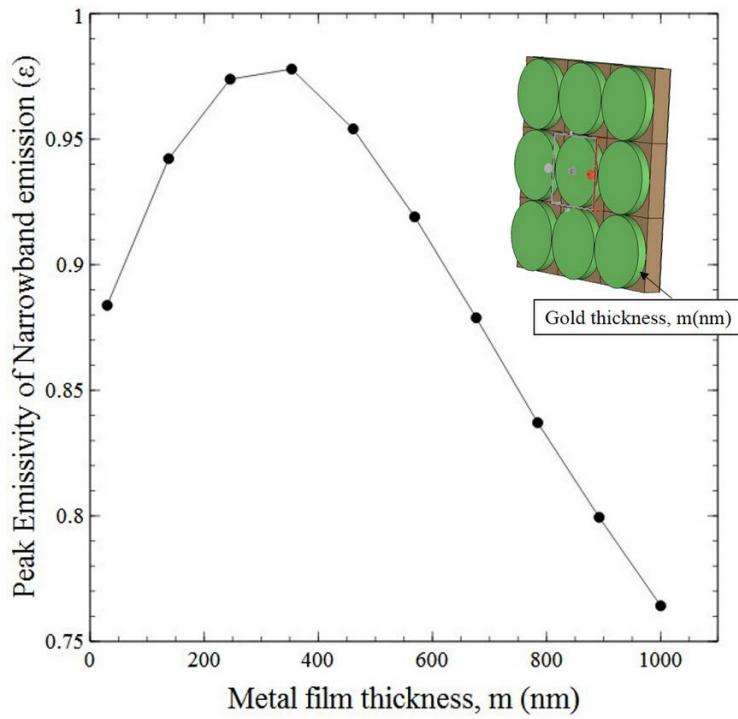Figure 71 Effect of Au film thickness on peak emissivity in narrowband emission in a periodic array structure.
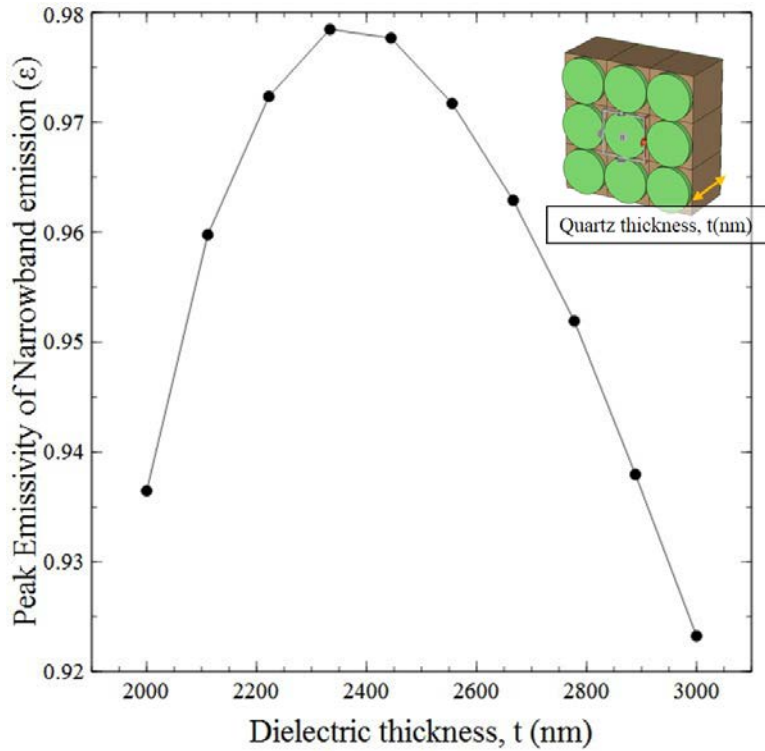
Figure 72 Effect of dielectric film thickness on peak emissivity in a periodic Au-quartz disk array structure.

6.5 Impact Of Temperature On The Frequency Selectivity Of Emission

The effect of temperature on the emissivity of the periodic structure was calculated as a function of of the input variables. The electron phonon frequency ω_c (sec^{-1}) and the refractive index of the dielectric material were used as temperature dependent values. In 1972, Ujihara reported a study on the impact of temperature on the electron-phonon collision frequency for Ag, as shown in Figure 73. Figure 75 shows the temperature dependence of the electron-phonon collision frequency in the temperature range of 300 to 1000K[106]. In 1980, Li reported the variations in the refractive index of Silicon and Germanium as a function of temperature[107]. Figure 74 and Figure 76 show the temperature dependent values of these refractive indices. These values were used as input parameters for the simulation model (to account for the dependence of temperature on the frequency selectivity) and to obtain a comparison of the current density at the surface of the periodic hole array structure at

two different temperatures. The maximum current density measured for a Au-Quartz periodic hole array at 400K was calculated as 13.072 x 10^{12} A/m^2 compared to that at 300K which was 11.422 x 10^{12} A/m^2.
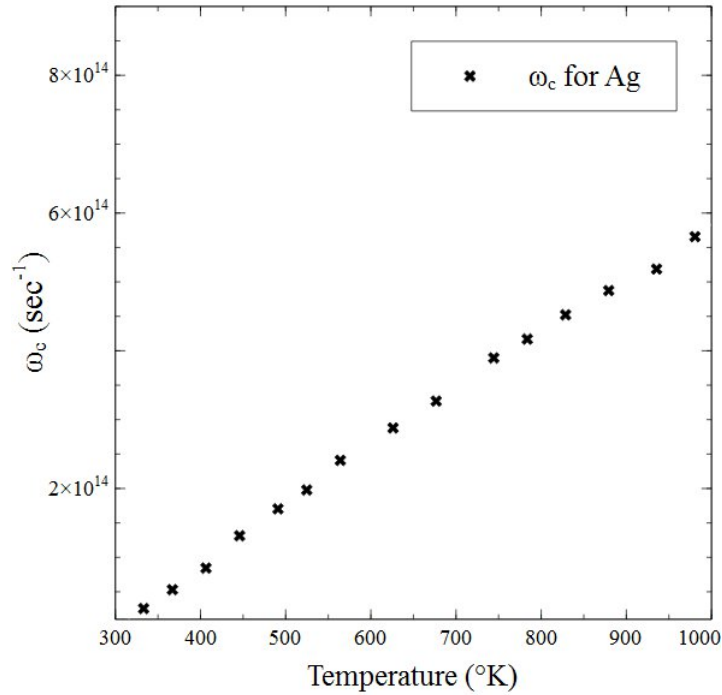
Figure 73 Electron-phonon collision frequency ω_c in sec^{-1}for Ag [106] as a function of temperature.
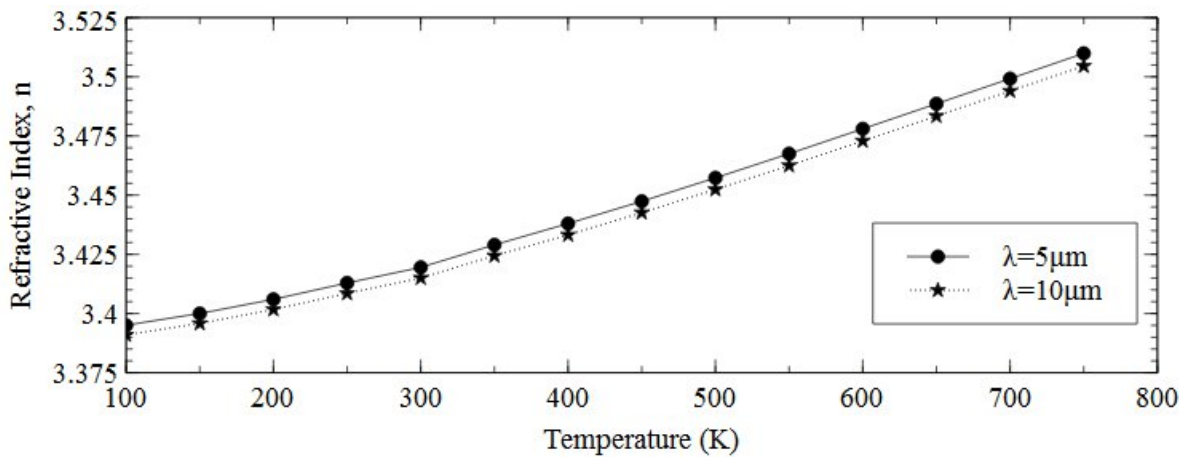
Figure 74 Refractive index of silicon with respect to temperature for λ=5μm, 10μm[107].

78
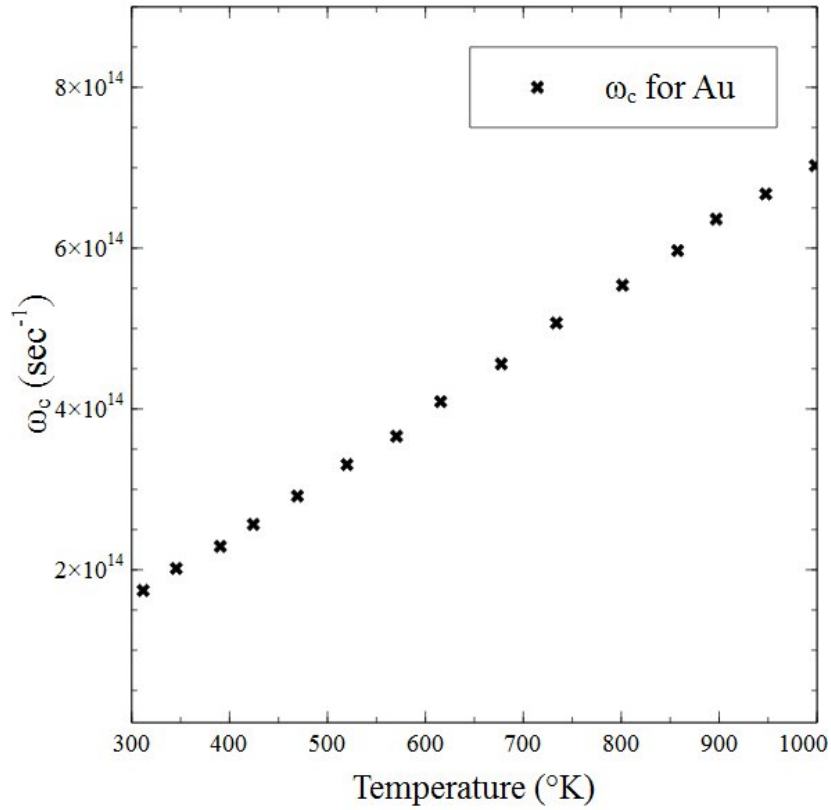
Figure 75 Electron-phonon collision frequency ω_c in sec^{-1} for Au [106] as a function of temperature.
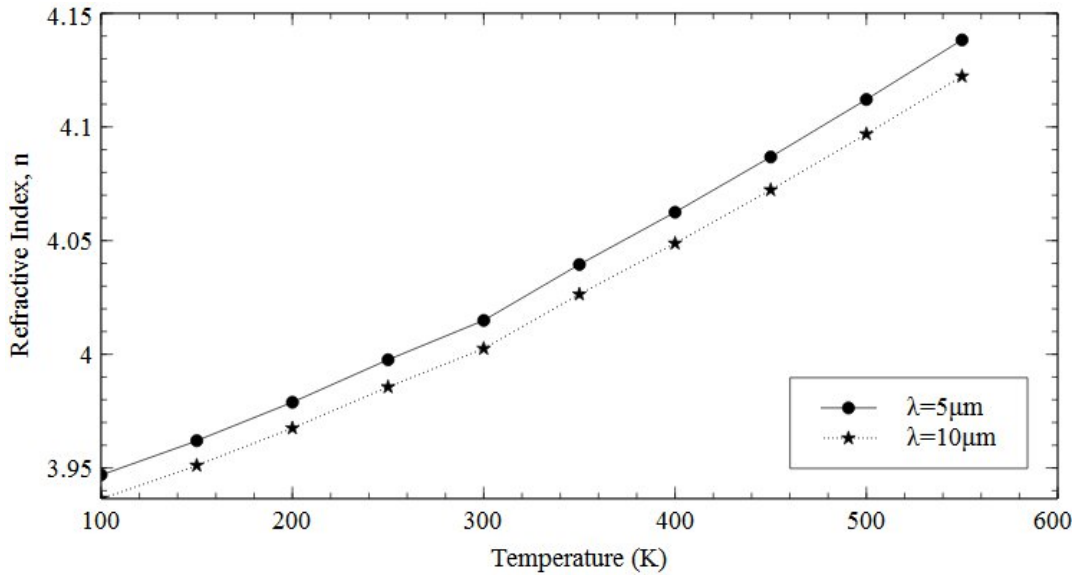
Figure 76 Refractive index of germanium with respect to temperature for λ=5µm, 10µm [107].

79
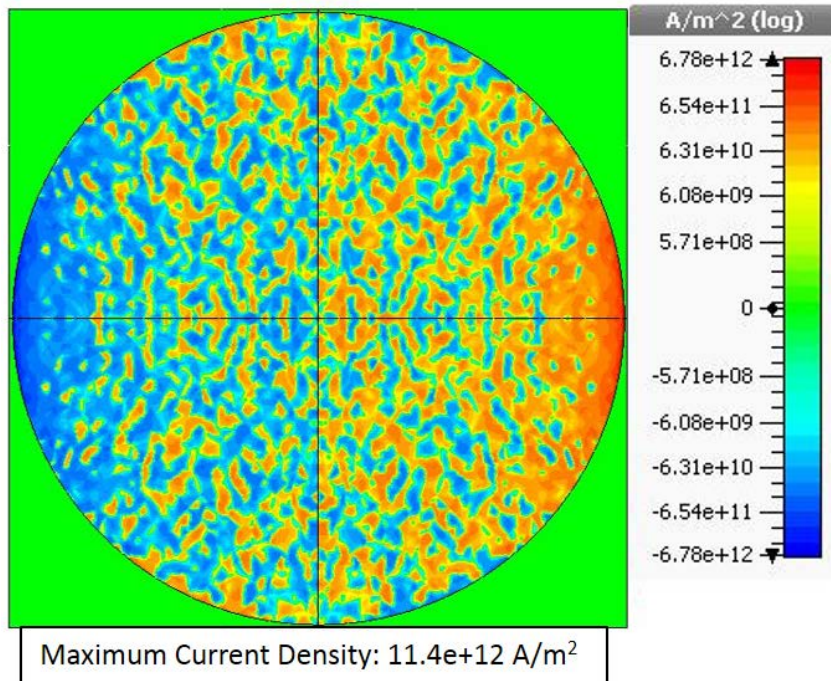
Figure 77 Current density profile (A/m^2) in an Au-quartz disk array at 300K.
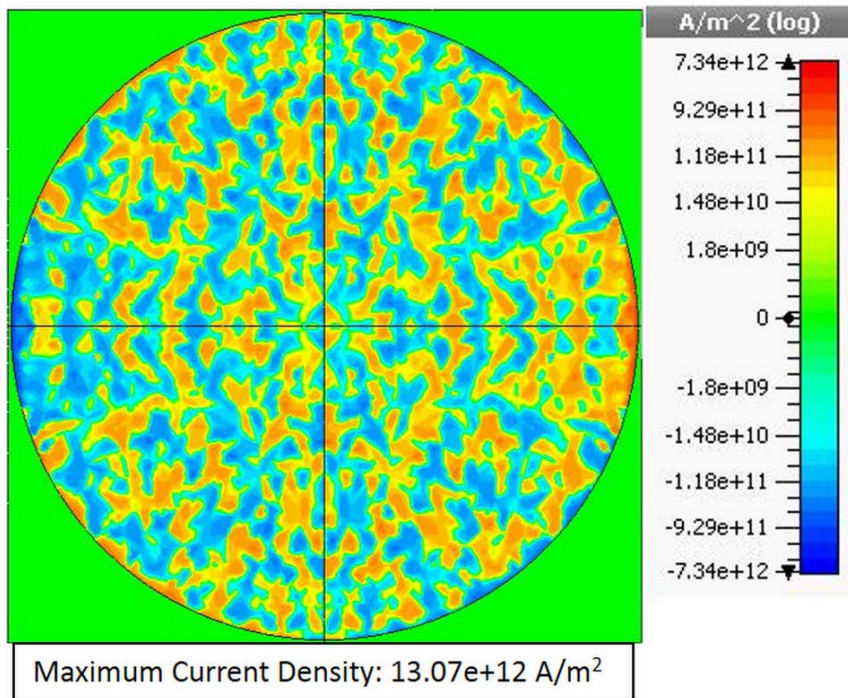
Figure 78 Current density profile (A/m^2) in an Au-quartz disk array at 400K.

80

More importantly, the emissivity spectra simulated for periodic disk array structures at different temperatures show that different peaks in the emissivity spectra respond differently to changes in temperature. Some peaks may show higher values of emissivity at higher temperatures, whereas other peaks may show an adverse lowering of emissivity at higher temperatures. Figure 80 shows the emissivity spectra for a Au-Quartz periodic disk array at varying temperatures, 300K and 700K. Figure 79 shows the emissivity spectra for a similar disk array structure at a 300K and 700K. As shown in Figure 80 and Figure 79 the first peak ~30THz shows a lower emissivity at 400K and even lower emissivity at 700K. However, the second peak ~60THz, shows a higher emissivity with an increase in temperatures, like 400K and 700K. This is a good indication that a selective emitter/absorber designed for frequency selectivity at a certain frequency, f_s might not be as selective over a broad range of temperatures. Thus, the design of such frequency selective surfaces must account for the change in material properties with respect to any variation in the temperature of operation.

From an efficient design perspective, it would be optimum to consider these temperature dependent material properties to produce a structure that is more tolerant to a change in the working temperature of such a frequency selective device. This can be performed by designing a selective emitter to be used in a temperature range of 300K-500K, as an optimum device with an average working temperature of T=400K. Such an optimization can also be undertaken by careful scrutiny of materials, that is, find materials that do not show a significant change in their refractive index or drude characteristics over a broad temperature window. The state of the art selective emitter/absorber designs do not account for any temperature variations in material properties. The effect of temperature on the frequency selectivity lacks uniformity. Some selective emission peaks increase in peak amplitude at higher temperatures whereas other peaks may be suppressed at higher temperatures. Being able to account for the effect of temperature can be a significant contribution in improving the performance of such a frequency selective device.

81
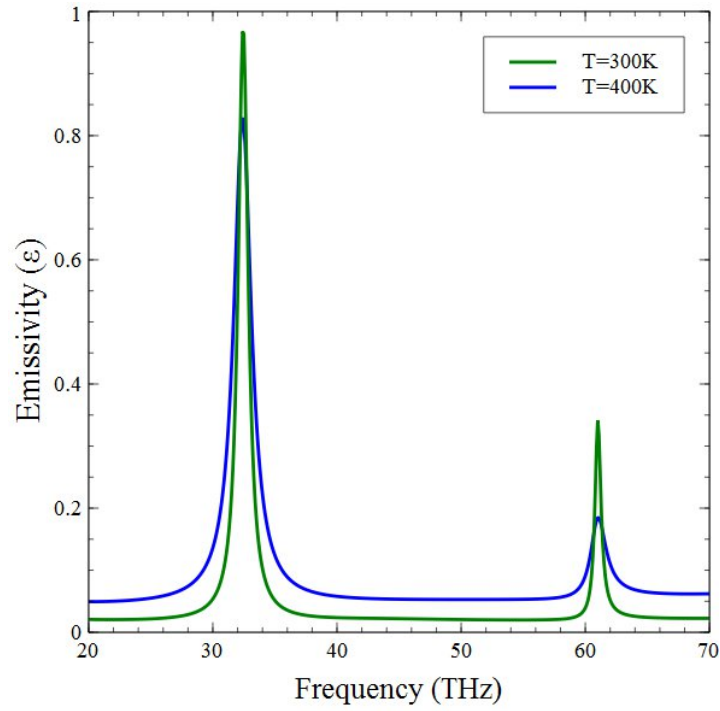
Figure 79 Variation in emissivity spectra for periodic Au-quartz disk array structures at different temperatures, i.e. 300K and 400K.
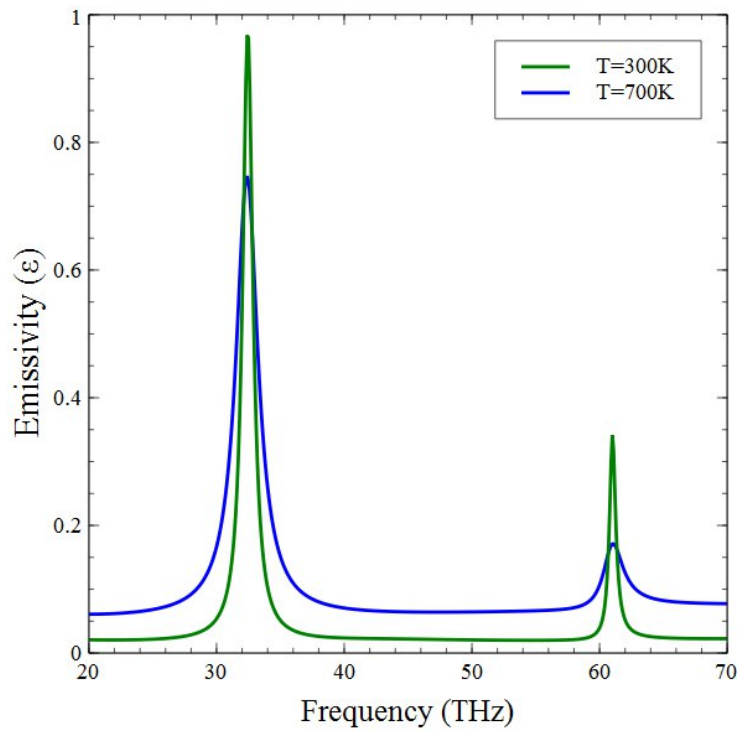
Figure 80 Variation in emissivity spectra for periodic Au-quartz disk array structures at different temperatures, i.e. 300K and 700K.

CHAPTER 7:

CONCLUSIONS AND FUTURE WORK

Metal-Insulator-Metal diodes for use in energy harvesting at 30 THz must show adequate nonlinearity for small signal rectification such as 30 mV. In a rectenna assembly, the output voltage signal received as an output from a single nanoantenna can be as small as ~30μV, as presented by Sarehraz [3]. Thus, only a hybrid nanoantenna array of as many as 1000 nanoantennas is required to provide a signal in the ~30mV range [113]. A metal-insulator-metal diode with highly nonlinear I-V characteristics is required in order for such small signal rectification to be possible. Such diode fabrication is faced with two major fabrication challenges. The first one being the lack of a precisely controlled deposition process to allow a pinhole free insulator deposition less than 3nm in thickness [4], [11], [25], [37], [95], [114]–[120]. Another major challenge is the deposition of a top metal contact on the underlying insulating thin film. As a part of this research study, most of the MIM diodes were fabricated using Langmuir Blodgett monolayers deposited on a thin Ni film that was sputter coated on a silicon wafer. The monolayer assembly was irradiated with ultraviolet radiation in order to perform intermolecular crosslinking using UV initiated polymerization. The polymerization of the LB monolayers helped in reducing the likelihood of pinholes and also allowed for a top contact sputtering on the underlying insulating layer, using a confined shadow mask. In addition to material characterization of all the individual films using IR, UV-VIS spectroscopy, electron microscopy and atomic force microscopy, cyclic voltammetry, the I-V characteristics, resistance, current density, rectification ratio and responsivity with respect to the bias voltage were also measured for the electrical characterization of these MIM diodes.

Further improvement in the diode rectification ratio and responsivity was obtained with Langmuir Blodgett films grown by the use of horizontally oriented molecules [50], [51]. These long chain polymeric molecules exhibit a two-dimensional molecular assembly thereby reducing the tunneling distance between the metal electrodes on either side of the insulating layer. Rectification ratios as high as 450:1 at ±200mV were obtained for an MIM diode configuration of Ni-LB films of Arachidic Acid films-(Au/Pd). Responsivity as high as ~18 was obtained for a MIM diode configuration with Ni-PMMA monolayers-(Au/Pd). Higher responsivity reflects improvement in the rectification ability of the diode[79], [80]. Eliasson et al have reported the use of responsivity as a measure of improvement in small signal rectification[81][82].

With a significant improvement in the rectification ratio, responsivity and asymmetry, the device fabrication still has certain drawbacks that need to be addressed. First, device packaging remains to be a challenge, since, in this work, the experiments used a micromanipulator setup for careful probing on the top metal contact. For a certain set of experiments, a liquid Ga drop was used as a secondary top contact on the Ni-LB film-Ni assembly. Second, the fabrication process involves Langmuir Blodgett monolayers of several fatty acids, these molecules at the molecular level are not resistant to most solvents or resist developers. Hence, the active area of such a device cannot be defined with photolithography due to material constraints.

In future work, one could possibly use atomic layer deposition of ZrO_2, HfO_2, Al_2O_3, or plasma nitriding processes to obtain insulating films in conjunction with photolithography. Such MIM diodes would need a significant amount of process optimization to improve the integrity of these films and reduce the likelihood of pinholes while maintaining an oxide or nitride thickness under 3nm [121]–[124]. As discussed in the introduction, the antenna element in rectennas has a limited bandwidth. In other words the diode can only utilize a portion of the incident radiation that is around the center

frequency of the antenna. The rest of the radiation does not reach the tunnel diode because of the bandwidth limitation of the antenna element preceding the diode.

Sarehraz et al have proposed a patch antenna for use ~30THz with a bandwidth of 9.5% of the center frequency [3]. This is to say that the allowable bandwidth of the incident radiation that can be used by this rectenna assembly must be within 9.5% of 30THz or ±1.5THz from the center frequency. This bandwidth constraint led to research in the field of frequency selective emitters capable of providing a narrowband emission around 30THz.

Several grating structures were fabricated in the form of Ni-Si periodic arrays, in a cleanroom environment using photolithography, sputtering and deep reactive ion etching. These frequency selective samples were characterized with the help of focusing optics, monochromators and HgCdTe detectors. The results obtained from the emission spectra were utilized to calibrate a simulation model with Computer Simulation Technology (CST) which uses numerous robust solving techniques, such as the finite element method, in order to obtain the optical parameters for the model. Thereafter, a thorough analysis of the different dimensional and material parameters was performed, to understand their dependence on the emissivity of the selective emitter.

Further research on the frequency selectivity of the periodic nano-disk or nano-hole array led to the temperature dependence of the simulated spectra, because the material parameters, such as refractive index or drude model collision frequency, vary with temperature. Thus, the design of frequency selective absorbers/emitters must account for the temperature range of operation of these structures. In conclusion, not all the emissivity peaks respond the same way to an increase in temperature. Some peaks show increased emissivity with an increase in temperature, whereas other peaks show lower emissivity as the temperature increases, thus making it even more critical to account for the temperature dependent material properties in the design of frequency selective structures.

REFERENCES

[1]Brown, W. C. Proc Sps Microw. Syst. Work. Jscnasa 1980, 271–280.

[2]Joshi, S.; Moddel, G. Appl. Phys. Lett. 2013, 102, 083901.

[3]Sarehraz, M. Novel Rectenna For Collection Of Infrared And Visible Radiation, University Of South Florida, 2005.

[4]Grover, S.; Member, S.; Moddel, G.; Member, S. 2011, 1, 78–83.

[5]Liu, X.; Tyler, T.; Starr, T.; Starr, A. F.; Jokerst, N. M.; Padilla, W. J. Phys. Rev. Lett. 2011, 107, 045901.

[6]Pralle, M. U.; Moelders, N.; Mcneal, M. P.; Puscasu, I.; Greenwald, A. C.; Daly, J. T.; Johnson, E. A.; George, T.; Choi, D. S.; El-Kady, I.; Biswas, R. Appl. Phys. Lett. 2002, 81, 4685.

[7]Hasman, E.; Dahan, N.; Kleiner, V.; Niv, A.; Biener, G.; Gorodetski, Y. In 2007 Quantum Electronics And Laser Science Conference; IEEE, 2007; Pp. 1–2.

[8]Alimardani, N.; Conley, J. F. Appl. Phys. Lett. 2013, 102, 143501.

[9]Alimardani, N.; Conley, J. F. In Proceedings Of SPIE - The International Society For Optical Engineering; Sulima, O. V.; Conibeer, G., Eds.; 2013; Vol. 8824, P. 88240s.

[10]Alimardani, N.; William Cowell, E.; Wager, J. F.; Conley, J. F.; Evans, D. R.; Chin, M.; Kilpatrick, S. J.; Dubey, M. J. Vac. Sci. Technol. A Vacuum, Surfaces, Film. 2012, 30, 01a113.

[11]Grover, S.; Moddel, G. IEEE J. Photovoltaics 2011, 1, 78–83.

[12]Raether, D. H. Surface Plasmons On Smooth And Rough Surfaces And On Gratings; Springer Tracts In Modern Physics; Springer Berlin Heidelberg, 1988; Vol. 111.

[13]Hibbins, A. P. 1999.

[14]Pendry, J. B.; Martín-Moreno, L.; Garcia-Vidal, F. J. Science 2004, 305, 847–848.

[15]Thio, T.; Ghaemi, H. F.; Lezec, H. J.; Wolff, P. A.; Ebbesen, T. W. J. Opt. Soc. Am. B Opt. Phys. 1999, 16, 1743–1748.

[16]Nguyen-Huu, N.; Chen, Y.-B.; Lo, Y.-L. Opt. Express 2012, 20, 5882–5890.

[17]Dahan, N.; Niv, A.; Gorodetski, Y.; Kleiner, V.; Hasman, E. In 2008 Proceedings Of The 9th Biennial Conference On Engineering Systems Design And Analysis; 2009; Vol. 4, Pp. 363–367.

[18]Bhansali, S.; Krishnan, S.; Stefanakos, E.; Goswami, D. Y.; Aswal, D. K.; Debnath, A. K. 2010; Vol. 79, Pp. 79–83.

[19]Celestin, M.; Krishnan, S.; Goswami, D. Y.; Stefanakos, E.; Bhansali, S. Procedia Eng. 2010, 5, 1055–1058.

[20]Chin, M.; Nichols, B.; Osgood, R.; Kilpatrick, S.; Dubey, M.; Dhar, N. Mrs Proc. 2011, 1303, Mrsf10–Mrsf1303 – Y06–Y09.

[21]Dagenais, M.; Choi, K.; Yesilkoy, F.; Chryssis, A. N.; Peckerar, M. C. In Proceedings Of SPIE - The International Society For Optical Engineering; Eldada, L. A.; Lee, E.-H., Eds.; 2010; Vol. 7605, P. 76050e – 76050e – 12.

[22]Grover, S.; Dmitriyeva, O.; Estes, M. J.; Moddel, G. IEEE Trans. Nanotechnol. 2010, 9, 716–722.

[23]Grover, S.; Joshi, S.; Moddel, G. J. Phys. D. Appl. Phys. 2013, 46, 135106.

87

[24]Hashem, I. E.; Rafat, N. H.; Soliman, E. A. IEEE J. Quantum Electron. 2013, 49, 72–79.

[25]Hashem, I. E.; Rafat, N. H.; Soliman, E. A. In 2013 IEEE 5th International Nanoelectronics Conference (Inec); IEEE, 2013; Pp. 61–64.

[26]Imafidon, O.; Georgakopoulos, S.; Vabbina, P. K.; Pala, N. In Proceedings Of SPIE - The International Society For Optical Engineering; George, T.; Islam, M. S.; Dutta, A. K., Eds.; 2010; Vol. 7679, P. 76792l – 76792l – 9.

[27]Joshi, S.; Moddel, G. Appl. Phys. Lett. 2013, 102, 083901.

[28]Joshi, S.; Zhu, Z.; Grover, S.; Moddel, G. In 2012 38th IEEE Photovoltaic Specialists Conference; IEEE, 2012; Pp. 002976–002978.

[29]Kinzel, E. C.; Brown, R. L.; Ginn, J. C.; Lail, B. A.; Slovick, B. A.; Boreman, G. D. Microw. Opt. Technol. Lett. 2013, 55, 489–493.

[30]Kinzel, E. C.; Brown, R. L.; Ginn, J. C.; Lail, B. A.; Slovick, B. A.; Boreman, G. D. In Proceedings Of SPIE - The International Society For Optical Engineering; Andresen, B. F.; Fulop, G. F.; Hanson, C. M.; Norton, P. R.; Robert, P., Eds.; 2013; Vol. 8704, P. 87041c.

[31]Krishnan, S.; La Rosa, H.; Stefanakos, E.; Bhansali, S.; Buckle, K. Sensors Actuators A Phys. 2008, 142, 40–47.

[32]Krishnan, S.; Bhansali, S.; Buckle, K.; Stefanakos, E. In Materials Research Society Symposium Proceedings; 2006; Vol. 935, Pp. 26–33.

[33]Periasamy, P.; Bergeson, J. D.; Parilla, P. A.; Ginley, D. S.; O'hayre, R. P. In 2010 35th IEEE Photovoltaic Specialists Conference; IEEE, 2010; Pp. 002943–002945.

[34]Periasamy, P.; Berry, J. J.; Dameron, A. A.; Bergeson, J. D.; Ginley, D. S.; O'hayre, R. P.; Parilla, P. A. Adv. Mater. 2011, 23, 3080–3085.

[35]Periasamy, P.; Guthrey, H. L.; Abdulagatov, A. I.; Ndione, P. F.; Berry, J. J.; Ginley, D. S.; George, S. M.; Parilla, P. A; O'hayre, R. P. Adv. Mater. 2013, 25, 1301–1308.

[36]Ratnadurai, R.; Krishnan, S.; Stefanakos, E.; Goswami, D. Y.; Bhansali, S.; Aswal, D. K.; Debnath, A. K. In Aip Conference Proceedings; 2010; Vol. 1313, Pp. 403–405.

[37]Ratnadurai, R.; Krishnan, S.; Stefanakos, E.; Goswami, D. Y.; Bhansali, S. Procedia Eng. 2010, 5, 1059–1062.

[38]Araghi, H. Y.; Paige, M. F. Can. J. Chem. 2013, 91, 1130–1138.

[39]Bardosova, M.; Hodge, P.; Matsuda, H.; Nakanishi, F.; Tredgold, R. H. Langmuir 1999, 15, 631–633.

[40]Choi, Y.; Kwon, Y.; Lee, K. 2006 IEEE Nanotechnol. Mater. Devices Conf. 2006, 564–565.

[41]Hino, K.; Abe, S.; Kushida, M. Ieej Trans. Fundam. Mater. 2008, 128, 6–85.

[42]Iwamoto, M.; Suzuki, M.; Hino, T. In Proceedings Of The Symposium On Electrical Insulating Materials; Inst Of Electrical Engineers Of Japan, 1984; Pp. 173–176.

[43]Iwamoto, M.; Kubota, T.; Sekine, M. J. Phys. D Appl. … 2000, 575.

[44]Nijhuis, C. A.; Reus, W. F.; Barber, J. R.; Dickey, M. D.; Whitesides, G. M. Nano Lett. 2010, 10, 3611–3619.

[45]Hing, T. Japanese J. Appl. Physics, Part 1 Regul. Pap. Short Notes Rev. Pap. 1996, 35, 5400–5404.

[46]Kaneko, F.; Shibata, M.; Inaba, Y.; Kobayashi, S. Thin Solid Films 1989, 179, 121–127.

[47]Roberts, G. Langmuir-Blodgett Films; Springer, 1990; P. 444.

[48]Galletti, G. S.; Guiseppi-Elie, A. Thin Solid Films 1985, 132, 163–172.

[49]Ogawa, K. Polym. Int. 1992, 28, 25–33.

[50]Kumaki, J.; Kajitani, T.; Nagai, K.; Okoshi, K.; Yashima, E. J. Am. Chem. Soc. 2010, 132, 5604–5606.

[51]Aoki, H.; Takahashi, T.; Ito, S. Polym. J. 2010, 43, 218–221.

[52]Marquier, F.; Joulain, K.; Mulet, J.-P.; Carminati, R.; Greffet, J.-J.; Chen, Y. Phys. Rev. B 2004, 69, 155412.

[53]Hasman, E.; Kleiner, V.; Dahan, N.; Gorodetski, Y.; Frischwasser, K.; Balin, I. J. Heat Transfer 2012, 134, 031023.

[54]Hesketh, P.; Zemel, J.; Gebhart, B. Phys. Rev. B 1988, 37, 10795–10802.

[55]Sai, H.; Yugami, H.; Akiyama, Y.; Kanamori, Y.; Hane, K. J. Opt. Soc. Am. A. Opt. Image Sci. Vis. 2001, 18, 1471–1476.

[56]Sai, H.; Kanamori, Y.; Yugami, H. J. Micromechanics Microengineering 2005, 15, S243–S249.

[57]Zhu, Z.; Joshi, S.; Pelz, B.; Moddel, G. In Proceedings Of SPIE - The International Society For Optical Engineering; Sulima, O. V.; Conibeer, G., Eds.; 2013; Vol. 8824, P. 88240o.

[58]Maraghechi, P.; Foroughi-Abari, A.; Cadien, K.; Elezzabi, A. Y. Appl. Phys. Lett. 2012, 100, 113503.

[59]Maraghechi, P.; Foroughi-Abari, A.; Cadien, K.; Elezzabi, A. Y. Appl. Phys. Lett. 2011, 99, 253503.

[60]Simmons, J. G. J. Appl. Phys. 1963, 34, 2581.

[61]Simmons, J. G. J. Appl. Phys. 1963, 34, 1793.

[62]Girard-Egrot, A.; Blum, L. In Nanobiotechnology Of Biomimetic Membranes Se - 2; Martin, D., Ed.; Fundamental Biomedical Technologies; Springer Us, 2007; Vol. 1, Pp. 23–74.

[63]Search, H.; Journals, C.; Contact, A.; Iopscience, M.; Address, I. P. 1990, 95.

[64]Cemel, A.; Fort, T.; Lando, J. B. J. Polym. Sci. Part A-1 Polym. Chem. 1972, 10, 2061–2083.

[65]Pignataro, B.; Panebianco, S.; Consalvo, C.; Licciardello, A. Surf. Interface Anal. 1999, 27, 396–400.

[66]Ogawa, K. J. Phys. Chem. 1989, 5305–5310.

[67]Fukuda, K.; Shibasaki, Y.; Nakahara, H. Thin Solid Films 1988, 160, 43–52.

[68]Blumstein, A.; Billmeyer, F. W. J. Polym. Sci. Part A-2 Polym. Phys. 1966, 4, 465–474.

[69]Diao, P.; Jiang, D.; Cui, X.; Gu, D.; Tong, R.; Zhong, B. J. Electroanal. Chem. 1999, 464, 61–67.

[70]Ogawa, K. Polym. Int. 1992, 28, 25–33.

[71]Mino, N.; Tamura, H.; Ogawa, K. Langmuir 1992, 8, 594–598.

[72]Saito, A.; Urai, Y.; Itoh, K. Langmuir 1996, 12, 3938–3944.

[73]Kaneko, F. 1988, 220–226.

[74]Leger, A.; Klein, J.; Belin, M.; Defourneau, D. Thin Solid Films 1971, 8, R51–R54.

[75]Yoo, S.-Y.; Jung, S.-B.; Park, J.-C.; Kwon, Y.-S. In Proceedings Of The IEEE International Conference On Properties And Applications Of Dielectric Materials; IEEE, 1997; Vol. 2, Pp. 685–688.

91

[76]Meyer, E.; Howald, L.; Overney, R. M.; Heinzelmann, H.; Frommer, J.; Güntherodt, H.-J.; Wagner, T.; Schier, H.; Roth, S. Nature 1991, 349, 398–400.

[77]Kurnaz, M. L.; Schwartz, D. K. J. Phys. Chem. 1996, 100, 11113–11119.

[78]Kuhn, H.; Försterling, H.-D.; Waldeck, D. H. Principles Of Physical Chemistry; John Wiley & Sons, 2009; P. 1032.

[79]Ashwell, G. J.; Mohib, A. J. Am. Chem. Soc. 2005, 127, 16238–16244.

[80]Nijhuis, C. A.; Reus, W. F.; Whitesides, G. M. J. Am. Chem. Soc. 2010, 132, 18386–18401.

[81]Ashwell, G. J.; Williams, A. T.; Barnes, S. A.; Chappell, S. L.; Phillips, L. J.; Robinson, B. J.; Urasinska-Wojcik, B.; Wierzchowiec, P.; Gentle, I. R.; Wood, B. J. J. Phys. Chem. C 2011, 115, 4200–4208.

[82]Matino, F.; Arima, V.; Maruccio, G.; Phaneuf, R. J.; Sole, R. Del; Mele, G.; Vasapollo, G.; Cingolani, R.; Rinaldi, R. J. Phys. Conf. Ser. 2007, 61, 795–799.

[83]Ashwell, G. J.; Tyrrell, W. D.; Whittam, A. J. J. Mater. Chem. 2003, 13, 2855.

[84]Metzger, R. M. Mrs Proc. 2011, 636, D7.8.1/Jj9.8.1.

[85]Ashwell, G. J.; Urasinska, B.; Tyrrell, W. D. Phys. Chem. Chem. Phys. 2006, 8, 3314–3319.

[86]Hoofring, A. B.; Kapoor, V. J.; Krawczonek, W. J. Appl. Phys. 1989, 66, 430.

[87]Wilke, I.; Oppliger, Y.; Herrmann, W.; Kneubuehl, F. K. Appl. Phys. A Solids Surfaces 1994, 58, 329–341.

[88]Abdel-Rahman, M. R.; González, F. J.; Boreman, G. D. Electron. Lett. 2004, 40, 116.

[89]Esfandiari, P.; Bernstein, G.; Fay, P.; Porod, W.; Rakos, B.; Zarandy, A.; Berland, B.; Boloni, L.; Boreman, G.; Lail, B.; Monacelli, B.; Weeks, A. In Defense And Security; Andresen, B. F.; Fulop, G. F., Eds.; International Society For Optics And Photonics, 2005; Pp. 470–482.

[90]Krishnan, S.; La Rosa, H.; Stefanakos, E.; Bhansali, S.; Buckle, K. Sensors Actuators A Phys. 2008, 142, 40–47.

[91]Kwangsik, C.; Yesilkoy, F.; Chryssis, A.; Dagenais, M.; Peckerar, M. IEEE Electron Device Lett. 2010, 31, 809–811.

[92]Bean, J. A.; Weeks, A.; Boreman, G. D. IEEE J. Quantum Electron. 2011, 47, 126–135.

[93]Zhang, F.; Meng, F.-Y.; Lee, J.-C.; Wu, Q. In 2013 IEEE International Wireless Symposium (Iws); IEEE, 2013; Pp. 1–4.

[94]Wood, R. W. Proc. Phys. Soc. London 1902, 18, 269–275.

[95]Rayleigh, Lord. Proc. R. Soc. London. Ser. A, Contain. Pap. A Math. Phys. Character 1907, 79, 399–416 Cr – Copyright © 1907 The Royal Soci.

[96]Otto, A. Zeitschrift FuR Phys. 1968, 216, 398–410.

[97]Kretschmann, E.; Raether, H. Z. Naturforsch. A 1968, 23, 2135.

[98]Akimov, A. V; Mukherjee, A.; Yu, C. L.; Chang, D. E.; Zibrov, A. S.; Hemmer, P. R.; Park, H.; Lukin, M. D. Nature 2007, 450, 402–406.

[99]Purcell, E.; Torrey, H.; Pound, R. Phys. Rev. 1946, 69, 37–38.

[100]Bergman, D.; Stockman, M. Phys. Rev. Lett. 2003, 90, 027402.

[101]Yu, N.; Cubukcu, E.; Diehl, L.; Belkin, M. A.; Crozier, K. B.; Capasso, F.; Bour, D.; Corzine, S.; HoFler, G. Appl. Phys. Lett. 2007, 91, 173113.

[102]Lal, S.; Link, S.; Halas, N. J. Nat. Photonics 2007, 1, 641–648.

[103]Liu, Y.; Bartal, G.; Genov, D.; Zhang, X. Phys. Rev. Lett. 2007, 99, 153901.

[104]Sorger, V. J.; Oulton, R. F.; Yao, J.; Bartal, G.; Zhang, X. Nano Lett. 2009, 9, 3489–3493.

[105]Plasmonics: Fundamentals And Applications; Springer Us: Boston, Ma, 2007.

[106]Ujihara, K. J. Appl. Phys. 1972, 43, 2376.

[107]Li, H. H. J. Phys. Chem. Ref. Data 1980, 9, 561.

[108]Pagnia, H.; Sotnik, N.; Stauss, H. Phys. Status Solidi 1985, 90, 771–778.

[109]Ratnadurai, R.; Krishnan, S.; Stefanakos, E.; Goswami, D. Y.; Bhansali, S. Procedia Eng. 2010, 5, 1059–1062.

[110]Ratnadurai, R.; Krishnan, S.; Stefanakos, E.; Goswami, D. Y.; Bhansali, S.; Aswal, D. K.; Debnath, A. K. 2010, 403, 403–405.

[111]Hegyi, B.; Csurgay, Á.; Porod, W. J. Comput. Electron. 2007, 6, 159–162.

[112]Properties, E.; Langmuir-Blodget, U. P. 1990, 25.

[113]Krishnan, S.; Stefanakos, E.; Bhansali, S. Thin Solid Films 2008, 516, 2244–2250.

[114]Rockwell, S.; Lim, D.; Bosco, B. A.; Baker, J. H.; Eliasson, B.; Forsyth, K.; Cromar, M. In 2007 IEEE Radio Frequency Integrated Circuits (RFIC) Symposium; IEEE, 2007; Pp. 171–174.

[115]In-Situ Nitride Initiation Layer For RRAM Metal Oxide Switching Material, 2014.

[116]Oxides—Advances In Research And Application: 2013 Edition: Scholarlybrief; Scholarlyeditions, 2013; P. 442.

[117]Chambers, B. A.; Macdonald, B. I.; Ionescu, M.; Deslandes, A.; Quinton, J. S.; Jasieniak, J. J.; Andersson, G. G. Sol. Energy Mater. Sol. Cells 2014, 125, 164–169.

[118]Kim, H.; Lee, J. T.; Lee, D.-C.; Magasinski, A.; Cho, W.; Yushin, G. Adv. Energy Mater. 2013, 3, 1308–1315.